# Elaboration, structure and functional properties of BiFeO3-based ferroelectric ceramics

Zhuo Yu

# THESE DE DOCTORAT EN COTUTELLE

LE MANS UNIVERSITE

COMUE UNIVERSITE BRETAGNE LOIRE

ECOLE DOCTORALE N° 596
*Matière, Molécules, Matériaux*
Spécialité : **PHYSIQUE**

**Zhuo YU**

**Titre: Elaboration, structure and functional properties of $BiFeO_3$-based ferroelectric ceramics**

**Thèse présentée et soutenue à Shanghai le 26 Mai 2021**
**Unité de recherche : IMMM-UMR CNRS et SHANGHAI INSTITUTE OF CERAMICS**
**Thèse N: 2021LEMA1018**

**Rapporteurs avant soutenance** :

| | |
|---|---|
| Isabelle MONOT-LAFFEZ | Professeur, Université de Tours |
| Soonil LEE | Professeur, Université Nationale de Changwon |

**Composition du Jury:**

| | | |
|---|---|---|
| Président : | Jingrong CHENG | Professeur, Université de Shanghai |
| Examinateurs : | | |
| | Kin Wing KWOK | Professeur, Université Polytechnique de Hong Kong |
| | Jean-Marc GRENECHE | DR-CNRS, IMMM-CNRS Le Mans Université |
| | Jiangtao ZENG | Professeur, Institut de Céramiques de Shanghai |
| Dir. de thèse : | Guorong LI, | Professeur, Institut de céramique de Shanghai |
| Dir. de thèse : | Abdel Hadi KASSIBA, | Professeur, IMMM-CNRS Le Mans Université |

# Acknowledgement

I would like to express my deep and sincere gratitude to my thesis of **Prof. Guorong Li** and **Prof. Abdelhadi Kassiba**, who imparted me the opportunity to study in their group and led me into the piezoelectric field and related interdisciplinary field. They taught me to be hopeful, patient and persistent towards my research. It was really fortunate for me to study in France as a joint PhD student.

I would like to acknowledge Prof. Jiangtao Zeng, Prof. Liaoying Zheng, Prof. Ronghua Zeng, Associate Prof. Zhenyong Man, Associate Prof. Kunyu Zhao, Associate Prof. Tian Tian, Mr. Xuezheng Ruan, Mr. Caiming Zhong, Ms. Xue Shi, Mr. Wenbin Liu, for kindly assistance during my scientific study.

I am very grateful to Prof. Jean-Marc Greneche for his help in the Mössbauer measurement. My thanks would go also to Prof. Alain Bulou, Prof. Francois, Mr. Anthony Rousseau, Ms. Sandy, Mr. Frederic for kindly assistance during my study at Le Mans.

I sincerely appreciate Xiang Huang, Qiwei Lou, Qianying Sun, Jian Zou, Jiangguli, Pneng, Xiao Luo, Jing Shang, Weiwei Li, Wei Li, Xiang Xia, Yusi Huang, Bingjie Teng, Chunbo Li, Xi Chen, Haoxian Chen, Aihua Liang, Dingwei Liu, Yin Shi, Namei Ke, et al.

My warm thanks to the administrative officers in the department of graduate student, I acknowledge Zhiwei Zhou, Caifei Lu, Xinhong Lu, Xueying Zhao, et al.

Lastly, I sincerely appreciate my **parents** for their selfless love and great confidence in me through all these year.

# List of publications

[1]. Zhuo Yu, Jiangtao Zeng, Liaoying Zheng, Jiangguli Peng, Guorong Li*. "Effects of $Ba(Zr_{0.25}Ti_{0.75})O_3$ substituent on ferroelectric properties in the $BiFeO_3$-$PbTiO_3$ high temperature ceramics". **Ceramics International.** (2018) 44:S65-S68.

[2]. Zhuo Yu, Jiangtao Zeng, Abdelhadi Kassiba, Liaoying Zheng, Jiangguli Peng, Guorong Li*. "Enhanced electrical properties of $BiFeO_3$-$PbTiO_3$ based ceramics with suitable raw material". **Journal of Materials Science: Materials in Electronics.** (2019) 30:14500–14507.

[3]. Zhuo Yu, Jiangtao Zeng, Liaoying Zheng, Wenbing Liu, Guorong Li*, Abdelhadi Kassiba*. "Large piezoelectricity and high Curie temperature in novel bismuth ferrite-based ferroelectric ceramics". **Journal of the American Ceramic Society.** (2020)103:6435–6444.

[4]. Zhuo Yu, Jiangtao Zeng, Liaoying Zheng, Anthony Rousseau, Guorong Li*, Abdelhadi Kassiba*. "Microstructure effects on the energy storage density in $BiFeO_3$-based ferroelectric ceramics". **Ceramics International.** (2021) 47:12735-12741.

# Conferences

[1] Nature Conferences of Ferroic Materials: Challenges and Opportunities. Xi'an, China (11/2017)

[2] 9th China-Japan Symposium on Ferroelectric Materials and Applications. Chengdu, China (09/2017)

[3] 2018 International Symposium on Solid-State Cooling Materials and Devices. Guangzhou, China (11/2018) **(Poster)**

[4] 21th Graduate English Academic Exchange Conference. Shanghai, China (11/2020) **(Oral)** (Title: A novel $BiFeO_3$-based ferroelectric ceramics with high temperature and high piezoelectric properties)

[5] 22th Graduate English Academic Exchange Conference. Shanghai, China (04/2021) **(Oral)** (Title: Microstructure effects on the energy storage density in $BiFeO_3$-based ferroelectric ceramics)

# Abstract

Bismuth ferrite ($BiFeO_3$, abbreviated as BFO) is an attractive lead-free ferroelectric material owing to its high Curie temperature ($T_c$=825 ℃) and large spontaneous polarization (~100 μC/cm$^2$). In addition, BFO ceramics with the addition of other perovskites $BaTiO_3$ (BT) and $PbTiO_3$ (PT) can form the morphotropic phase boundaries (MPB), similar to the PZT solutions. $BiFeO_3$-$PbTiO_3$ (BF-PT) based ceramics with a high Curie temperature are considered to be a very promising high-temperature piezoelectric material. However, two main factors restrict their applications in the field of high-temperature piezoelectric devices. This behavior can be related to BF-PT system in the vicinity of the MPB where a large tetragonality (*c/a*) occurs, enhancing the internal compatibility stresses which suppress the domain switching. The other reason is that high leakage current and dielectric loss make it difficult to be proper electrical poled of ceramics. In recent years, many reports were devoted to the enhancement of the piezoelectric properties by suitable or processing technology, mainly due to the dense microstructure, the formation of phase boundaries, and the reduction of the leakage current. It is critical to understand the interplay between the atomic features (ionic radius, electronegativity), the structure and interfaces (phase boundary, lattice distortion), the defects (oxygen vacancy, $Fe^{3+}/Fe^{2+}$) and the electrical performances (ferroelectricity, piezoelectricity, conductivity) for the BF-PT-based high-temperature piezoelectric ceramics. On the other hand, considering the large spontaneous polarization and the adjustable pseudo-cubic phase structure of BFO ceramics, BF-BT-based ferroelectric ceramics have great application prospects in the field of dielectric energy storage. Thus, exploring and developing the energy storage applications of BFO-based ferroelectric ceramics are relevant to research approaches for promising emerging technologies.

Based on the research background above, our investigations are closely associated with $BiFeO_3$-based ferroelectric ceramics. Doping modification was used to improve the ferroelectric and piezoelectric properties of $BiFeO_3$-$PbTiO_3$ based piezoelectric ceramics. At the same time, the defect pinning and the leakage current mechanisms of $BiFeO_3$ based ceramics were also studied, as well as the energy storage property of lead-free $BiFeO_3$-$BaTiO_3$ based ferroelectric ceramics. The main

results are as follows:

(1). Different lead raw materials have a significant influence on the electrical properties of BF-PT-based piezoelectric ceramics while a small amount of Bi-rich second phase precipitates at the grain boundaries of BF-PT-based ceramics prepared from $Pb_3O_4$. In addition, a high concentration of oxygen vacancies and $Fe^{2+}$ ions are induced in the samples prepared from $Pb_3O_4$. This leads to significantly higher leakage currents compared to the behavior in the samples prepared from PbO. This study not only confirms that the high leakage current of BF-PT-based piezoelectric ceramics is due to the fluctuation of $Fe^{3+}$ oxidation degree and the formation of oxygen vacancy, but also contributes identify the suitable lead raw material for the preparation of BF-PT-based piezoelectric ceramics with a high resistivity.

(2). A novel ferroelectric ternary system as $(0.76\text{-}x)BiFeO_3\text{-}0.24PbTiO_3\text{-}xBa(Sn_{0.2}Ti_{0.8})O_3$ was prepared by the solid-state reaction method. It is shown that the incorporation of large ionic radius $Ba^{2+}$ at A-site and nonferroelectric-active $Sn^{4+}$ at B-site generates a decrease in the tetragonality (*c/a*), which enhances the domain switching. Moreover, a wide multiphase coexistence region is formed with the content of BST ranging from x=0.13 to 0.28. The enhanced piezoelectric coefficient ($d_{33}$~200 pC/N) is achieved while maintaining a high Curie temperature ($T_c$~500 °C) and a high depolarization temperature ($T_d$~450 °C) for the composition of 0.6BF-24PT-0.16BST, which is superior to other BF-PT-based high-temperature piezoelectric ceramics.

(3). The comparison of the dielectric and ferroelectric properties for the poled and unpoled BF-PT-BST ceramics was studied. It is found that the pinning of domain wall is induced by defects such as $Fe^{2+}/Fe^{4+}$ and oxygen vacancies and causes the *P-E* loops being non-saturated for the unpoled BF-PT-BST ceramics. After poling, the *P-E* and *S-E* loops are displaced along the *E* axis with the internal bias field, which is related to the formation of the defect dipole which didn't align easily in the direction of the electric field. By increasing the temperature or decreasing the frequency of the electric field, the oxygen vacancies can be moved along the direction of the electric field leading to a decrease of the internal bias field. In addition, with the decrease of $BiFeO_3$ content, the difference in ferroelectric properties gradually disappeared and the internal bias field decreases for the unpoled and poled BF-PT-BST ceramics. This may be related to the decrease of the concentration of charged defects for the

ceramics.

(4). The influence of Mn doping on the conductivity, dielectric and ferroelectric properties of $0.7BiFeO_3$-$0.3PbTiO_3$ ceramics was systematically studied. It was found that the high leakage current in the pure 0.7BF-0.3PT ceramics limits drastically its use in piezoelectric devices. In addition, the thermal variation of dielectric loss curve in pure 0.7BF-0.3PT ceramics shows a relaxation peak in the temperature range of 30-250 ℃ and the frequency range of 100 Hz-1 MHz. The calculated activation energy shows that the relaxation peak is related to the doubly-ionized oxygen vacancies. A small amount (0.15 wt.%) of Mn doping can significantly reduce the leakage current of BF-PT ceramics, which is related to the decrease of the oxygen vacancy concentration in the ceramics. However, when the content of Mn increases (0.45 wt.%), the leakage current of ceramics increases also as a consequence of the increasing charge carriers–caused by the fluctuation in the valence of the B-site (Mn, Fe).

(5). Lead-free BF-BT-based ceramics with fine- and coarse-grains were fabricated by the conventional solid-state reaction process. The high-energy ball milling technique was utilized to obtain the fine-grained ceramics. The grain size effects on the dielectric, ferroelectric and energy storage properties of $BiFeO_3$-$BaTiO_3$-based ceramics were investigated. The fined-grained BFBT-BMN ceramics exhibit the broadening of $\varepsilon$-$T$ curve and the slim $P$-$E$ loops, corresponding to a low remnant polarization $P_r$. The recoverable energy storage density ($W_{re}$) of the fine-grained BFBT-BMN ceramics greatly increased by 8 times from 0.16 J/cm$^3$ to 1.27 J/cm$^3$, compared to the coarse-grained BFBT-BMN ceramics. This study shows that the reduction of grain size is an effective method to improve the energy storage properties of $BiFeO_3$-based ferroelectric ceramics.

# Résumé

La ferrite de bismuth ($BiFeO_3$, abrégée en BFO) est un matériau ferroélectrique sans plomb possédant une température de Curie élevée ($T_c$=825 °C) et une grande polarisation spontanée (~100 μC/cm$^2$). En outre, avec l'ajout d'autres pérovskites $BaTiO_3$ (BT) et $PbTiO_3$ (PT), la céramique BFO peut former les limites de phase morphotropique (MPB), similaires aux solutions solides $(Pb,Zr)TiO_3$. Les céramiques à base de $BiFeO_3$-$PbTiO_3$ (BF-PT) avec une haute température Curie sont potentiellement très prometteurs comme matériaux piézoélectriques hautes températures. Cependant, deux facteurs principaux limitent de telles applications. Il s'agit notamment du comportement du système BF-PT à proximité du MPB où une grande tétragonalité (*c/a*) se produit, favorisant les contraintes de compatibilité interne qui suppriment la commutation des domaines. L'autre raison est lié au courant de fuite élevé et aux perte diélectriques importantes qui compromettent le poling électrique optimal de ces céramiques. Dans la période récente, de nombreux travaux ont été consacrés à l'amélioration des propriétés piézoélectriques en modifiant le dopage et la méthode d'élaboration pour densifier la céramique, former des limites de phase et réduire les courants de fuite. Dans ce contexte, il est essentiel de comprendre l'interaction entre les caractéristiques des éléments chimiques (rayon ionique, électronégativité), la microstructure (limite de phase, distorsion du réseau), les défauts (lacunes d'oxygène, valence mixte $Fe^{3+}/Fe^{2+}$) et les performances électriques (ferroélectricité, piezoélectricité, conductivité) pour les céramiques piézoélectriques à hautes température à base de BF-PT. D'autre part, compte tenu de la grande polarisation spontanée et de la structure de phase pseudo-cubique de la céramique BFO, la céramique ferroélectrique à base de BF-BT est potentiellement susceptible d'applications dans le domaine du stockage diélectrique de l'énergie. Ces aspects justifient l'intérêt des études menées sur les céramiques à base de BFO et qui font l'objet des travaux de cette thèse. Ainsi, la modification du dopage a été exploitée pour améliorer les propriétés ferroélectriques et piézoélectriques des

céramiques piezoélectriques BFO-PT. De même, les mécanismes de pinning des défauts et ceux liés aux courants de fuite ont été étudiés en lien avec les propriétés de stockage d'énergie dans BFO-PT. Les principales contributions sont résumées ci-dessous:

(1). Les précurseurs à base de plomb ont une influence significative sur les propriétés électriques de la céramique piézoélectrique à base de BF-PT alors qu'une faible quantité de la phase riche en Bismuth est précipitée aux limites de grains des céramiques BF-PT préparées à partir de $Pb_3O_4$. Avec ce même précurseur, une forte concentration de lacunes d'oxygène et de $Fe^{2+}$ est créée dans la céramique et engendre des courants de fuite significativement plus élevés que les échantillons préparés à partir de PbO. Cette étude confirme d'une part que les courants de fuite élevés dans les céramiques piezoélectriques à base de BF-PT sont liés à la valence mixte des ions Fer et à la formation de lacunes d'oxygène. D'autre part, l'étude souligne que la nature du précurseur à base de Pb joue un rôle critique dans l'élaboration de céramiques piézoélectriques à base de BF-PT possédant une forte résistivité.

(2). Une nouvelle céramique ferroélectrique de formule $(0.76\text{-}x)BiFeO_3\text{-}0.24PbTiO_3\text{-}xBa(Sn_{0.2}Ti_{0.8})O_3$ a été élaborée par une méthode de réaction à l'état solide. Dans cette structure, l'incorporation des ions $Ba^{2+}$ à grand rayon ionique dans le site A de la pérovskite et des ions $Sn^{4+}$ dans le site B génère une diminution de la tétragonalité (*c/a*), ce qui améliore la commutation des domaines ferroélectriques. En outre, une large région de coexistence de phases est formée avec un taux de BST allant de 0,13 à 0,28. Le coefficient piézoélectrique atteint la valeur $d_{33}$~200 pC/N tout en maintenant une température de Curie élevée ($T_c$~500 °C) et une température de dépolarisation élevée ($T_d$~450 °C) pour une composition de 0.6BFO-0.24PT-0.16BST. Ces performances sont nettement améliorées par rapport aux autres céramiques piézoélectriques à base de BF-PT.

(3). La comparaison des propriétés diélectriques et ferroélectriques pour les céramiques a été effectuée pour les céramiques BF-PT-BST avec ou sans poling. Il

est montré que l'accrochage (pinning) des murs de domaines par les défauts tels que $Fe^{2+}/Fe^{4+}$ et les sites de lacunes d'oxygène, provoque la nano-saturation des cycles *P-E* dans les céramiques BF-PT-BST sans poling. Par contre, avec le poling, les courbes *P-E* et ceux des contraintes *S-E*, sont déplacées le long de l'axe *E* avec le champ de polarisation interne crées par les dipôles liés aux défauts. Comme ces dipôles sont difficiles à aligner sur la direction du champ électrique appliqué, on procède par l'augmentation de la température ou la diminution de la fréquence du champ électrique pour favoriser l'alignement. Ce procédé contribue donc à la diminution du champ de polarisation interne. En outre, avec la diminution de la teneur en BFO, on limite progressivement la différence dans les propriétés ferroélectriques et du champ de polarisation interne pour les différentes céramiques BF-PT-BST avec ou sans poling. Ce comportement est probablement lié à la réduction de la concentration des défauts chargés dans les céramiques considérées.

(4). L'influence du dopage Mn sur la conductivité, les propriétés diélectriques et ferroélectriques de la céramique $0.7BiFeO_3$-$0.3PbTiO_3$ a été systématiquement étudiée. Cette approche vise à limiter le fort courant de fuite de la céramique pure 0.7BF-0.3PT qui compromet sérieusement son utilisation comme dispositifs piézoélectriques. De plus, pour la même céramique BFO-PT, la courbe des pertes diélectrique versus la température montre un pic de relaxation dans la gamme de température de 30-250 °C dans la gamme de fréquences de 100 Hz-1 MHz. L'énergie d'activation calculée montre que le pic de relaxation est lié aux sites de lacunes d'oxygène doublement ionisés. Aussi, le dopage Mn avec une faible quantité de l'ordre de 0.15 wt.% réduit considérablement le courant de fuite de la céramique BF-PT. Toutefois, lorsque la teneur en Mn augmente (0.45 wt.%), le courant de fuite de la céramique ré-augmente à nouveau. Cet effet peut être attribué aux porteurs de charges qui résultent des fluctuations de charges facilement réalisables pour les ions Mn et Fe dans les sites B de la céramique.

(5). Les céramiques à base de BF-BT-BMN sans plomb et avec dopage Mn ont été élaborées par le processus conventionnel de réaction à l'état solide. La technique

de broyage à haute énergie a été utilisée pour moduler la taille des grains céramiques et étudier son effet sur les propriétés diélectriques, ferroélectriques et de stockage de l'énergie. Les céramiques BF-BT-BMN à grains fins montrent un net élargissement de la courbe $\varepsilon$-$T$ et des cycles $P$-$E$ étroits associés à une faible polarisation rémanente $P_r$. La densité de stockage d'énergie ($W_{re}$) augmente considérablement de 0.16 J/cm$^3$ à 1.27 J/cm$^3$ avec la réduction de la taille des grains de telles céramiques. Ce résultat souligne la corrélation entre la microstructure de la céramiques et montre que la réduction de la taille du grain est une méthode efficace pour améliorer les propriétés de stockage de l'énergie des ferroélectriques à base de $BiFeO_3$.

# Contents

# Chapter 1 Introduction

## 1.1 Overview of ferroelectric/piezoelectric materials

The research on ferroelectric materials has a history of one hundred years. In the 1950s, the discovery of barium titanate ($BaTiO_3$, BT) ceramics accelerated the in-depth research and development of perovskite-structure piezoelectric ceramics. Among them, lead zirconate titanate ($Pb(Zr,Ti)O_3$, PZT) is the most important and performant piezoelectric material. It is suitable for a large-scale production and is used in key materials of basic electronic components such as actuators, sensors and transducers. After a century of research, ferroelectric materials play an essential role in modern information technology and the advancement of human science and technology.

### 1.1.1 Basic characteristics of ferroelectrics

A ferroelectric is a material that has spontaneous polarization within a certain temperature range, and the application of the electric field can switch the orientation states of the polarization [1-3]. According to the crystallographic symmetry, only a total of 10 point groups have spontaneous polarization, called polar point groups. If the spontaneous polarization is reversible under an external electric field, the material is called “ferroelectric”, as shown in Fig. 1.1(a).

A distinctive feature of ferroelectric materials is the behavior of the polarization under the electric field. The relationship between the electric displacement $D$ and the electric field $E$ is nonlinear, which is called the polarization-electric field hysteresis ($P$-$E$) loops [3], as shown in Fig. 1.1(b). With the increase of the applied electric field, the domains are aligned with the direction of the field, the polarization increases until almost all domains tend to the saturation condition (saturation polarization $P_s$). When the applied electric field is reversed, some domains undergo a back-switch,

while most of them remain aligned, leading to a non-zero polarization at zero field (remnant polarization $P_r$). With the opposite field increasing, a similar rearrangement of the polarization is observed in the negative field part. The electric field at zero polarization is called the coercive field ($E_c$). In addition, the current-electric field (*I-E*) curves and the strain-electric field (*S-E*) curve are also characteristic of ferroelectric materials, as shown in Fig. 1.1(c) and (d). The current-electric field curves exhibit a positive and negative current peak, which is related to the domain reversal [4]. The electric field at the peaks is identical to the $E_c$.

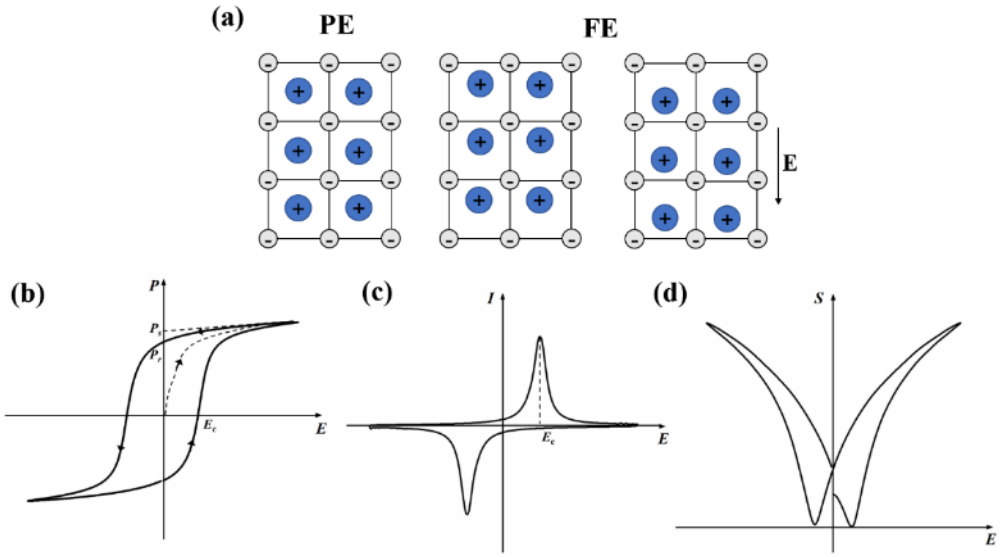


**Figure 1.1** (a) Formation of dipole moments: paraelectric (PE) state and ferroelectric (FE) states (before and after the application of an external field); (b) Typical hysteresis loops; (c) I-E loops; (d) Bipolar strain-electric-field curve.

## 1.1.2 Perovskite-type structure and tolerance factors

One of the most well-known structures for ferroelectric material is the perovskite-type $ABX_3$ structure [3, 5], such as $BaTiO_3$, $PbTiO_3$ and $BiFeO_3$. Due to their high tolerance to doping, the A- and B- sites can be occupied by a variety of different cations to form complex perovskites which can be described with the formula $(A',A'')(B',B'')O_3$. In PZT, the A-site is occupied by $Pb^{2+}$ ions, and $Zr^{4+}$ and $Ti^{4+}$ ions at the B-site. This feature allows the modification of specific physical properties for the ferroelectric material [6].

The tolerance factor $t$ is a powerful tool to predict the stability of the perovskite structure [7, 8]. According to the ion radius, $t$ is defined as:

$$t = \frac{r_A + r_X}{\sqrt{2}(r_B + r_X)} \quad \ldots (1.1)$$

where $r_A$, $r_B$ and $r_X$ represent the ion radius of A, B and X, respectively. If $t$=1, the crystal has an ideal cubic structure (Fig. 1.2(a)). If $t$>1, the B-site cation is smaller than the ideal value and can deviate from the center of the oxygen octahedron, which leads to a small polar distortion of the B-site, as shown in Fig. 1.2(b). If $t$<1, the A-site cation is smaller than the ideal value and cannot fill the oxygen octahedron, which leads to the rotations and tilting of the $BO_6$ octahedra, as shown in Fig. 1.2(c). It is generally considered that the perovskite structure is stable at 0.88<$t$<1.09, beyond which the crystal tends to other aristo-type structures [9].

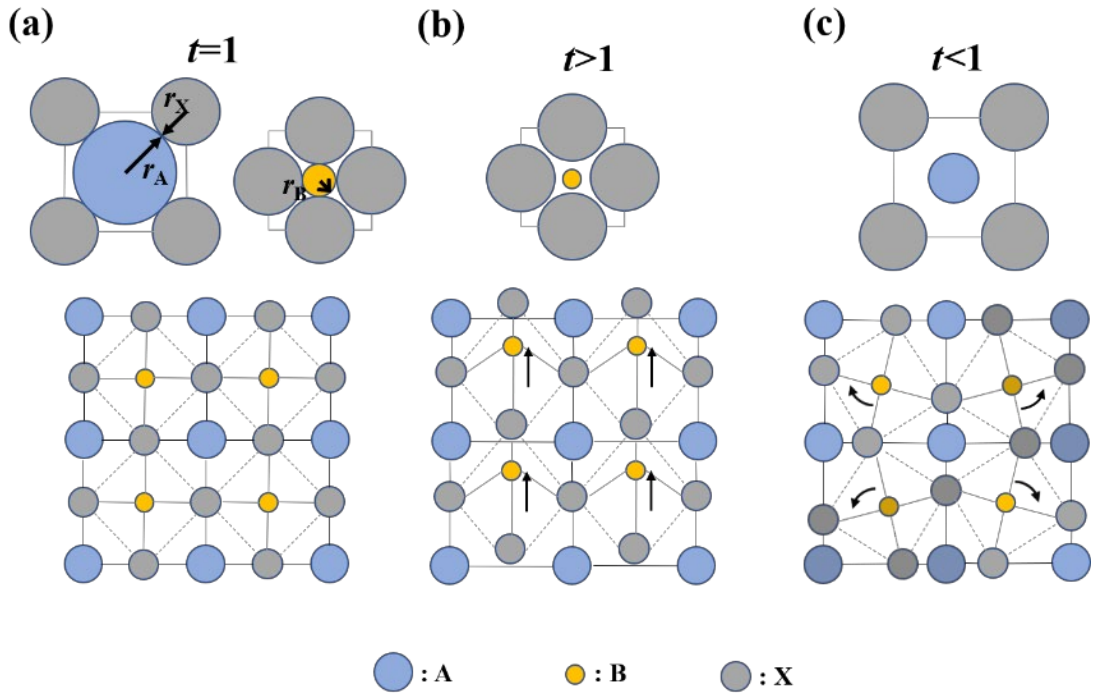


**Figure 1.2** Tolerance factor t: (a) $t$=1; (b) $t$>1; (c) $t$<1.

## 1.1.3 Advance in morphotropic phase boundary (MPB)

It is well known that morphotropic phase boundary (MPB) plays an important role in the piezoelectricity enhancement of perovskite-type piezoelectric materials

[10]. The origin of ultrahigh performance at the MPB for the ferroelectric materials has been intensively investigated. Initially, it was shown that the ferroelectrics at the MPB (rhombohedral (R)-tetragonal (T) phase) have 14 equivalent polarization directions, which is the main reason for their high electromechanical performance [11, 12]. With the development of material characterization techniques, a monoclinic phase was shown between the preciously established R and T regions using synchrotron X-ray diffraction. It was believed that the polarization rotation has a lower energy barrier along the rhombohedral-monoclinic-tetragonal path, which is conducive to the enhancement of its electromechanical performance [13, 14]. In addition, the thermodynamic Landau model developed concluded that the enhanced piezoelectricity at MPB can be ascribed to the facilitated polarization rotation due to the flattening of the Gibbs free energy anisotropy [15, 16].

On the other hand, the ferroelectric domain was proposed to explain the origin of the enhanced piezoelectricity at the MPB. Fig. 1.3 shows the domain structures of the PZT ceramics using a high-resolution transmission electron microscope (TEM) [17, 18]. Two domain structures can be clearly observed in the composition of PZT-53/47 at the MPB. A large number of nanodomains are embedded in the microdomains, and the angle between the nano- and microdomain walls is approximately 45°, as shown in Fig. 1.3(b). For the composition of PZT-45/55 (T phase) and PZT-60/40 (R phase), the lamellar and the herringbone-like domain configurations can be found in Fig. 1.3(a) and (c), respectively. Similarly, a hierarchical nano-/microscale domain configuration was found in the $Pb(Mg_{1/3}Nb_{2/3})O_3$-$PbTiO_3$ [19] and $(K,Na)NbO_3$ system at the MPB [20], as shown in Fig. 1.4(a) and (b), respectively. These studies have shown that the MPB is favorable for the formation of miniaturized nanodomains in ferroelectric ceramics, which is believed to provide the main contribution to high electrical properties for ferroelectric ceramics.

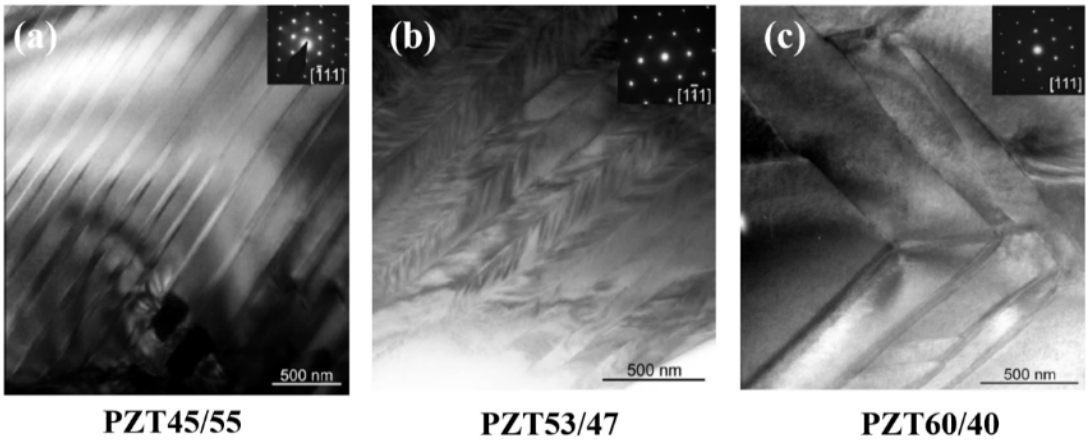


**Figure 1.3** Ferroelectric domain configurations of $Pb(Zr_{1-x},Ti_x)O_3$ piezoelectric ceramics with different content of Zr/Ti [18].

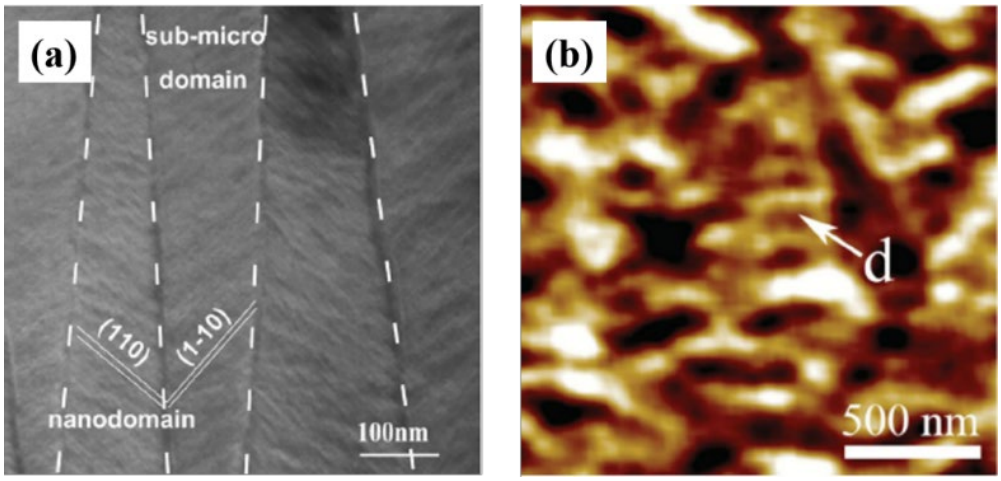


**Figure 1.4** (a) TEM bright field images of ferroelectric domain configurations of PMN-PT based ceramics with MPB structure [19]; (b) PFM images of ferroelectric domain configurations of KNN based ceramics with MPB structure [20].

Ren et al. [21-23] reported a lead-free system $Ba(Ti,Zr)O_3$-$(Ba,Ca)TiO_3$ (BZT-BCT) with a surprisingly ultrahigh piezoelectric coefficient of $d_{33}$~620 pC/N at the multi-phase-coexisting point, which is superior to other reported lead-free system, as shown in Fig. 1.5(a). Besides, it can be seen from Fig. 1.5(b) that the energy profile in the vicinity of the (tri-critical) triple point with a flat free energy landscape and a low energy barrier facilitates the polarization rotation. Thus, a vanishing polarization anisotropy is the main origin for the ultrahigh piezoelectricity

in BZT-BCT ceramics.

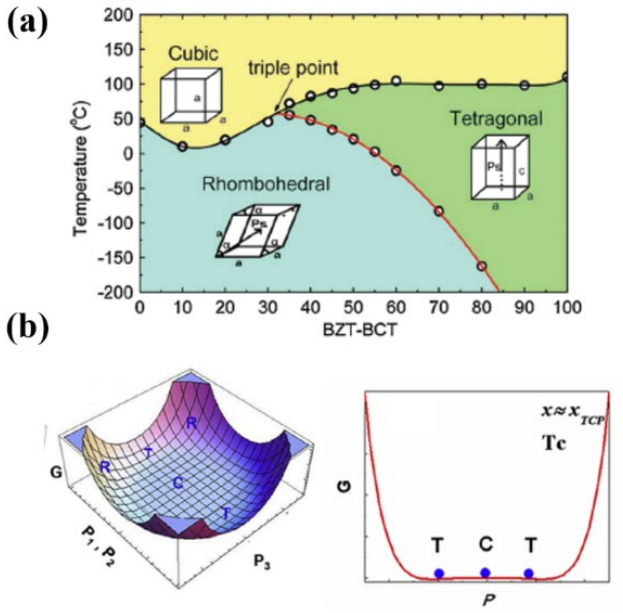


**Figure 1.5** (a) The phase diagram of BZT-BCT based ceramics [22]; (b) The (1-10) projection of the free energy profiles for the BZT-BCT based ceramics at the tricritical point and the corresponding 2D free energy profiles [23].

## 1.2 Overview of high-temperature piezoelectric ceramics

With the development of modern science and technology, the requirements for the stability of ferroelectric materials under external fields have become an important research task, especially in the fields of application at high temperatures. For example,

sensors in automotive electronics need to withstand high temperatures of about 150 ℃, which will be close to 500 ℃ in the future; the aircraft and aerospace industries have more stringent requirements for high-temperature (>>500 ℃) applications [24]. For piezoelectric ceramics, the Curie temperature ($T_c$) is an important parameter, which indicates the critical temperature when the phase structure of the material changes from the paraelectric phase (high symmetry) to the ferroelectric phase (low symmetry). When the temperature exceeds $T_c$, the oriented dipoles in the direction of poling of the poled piezoelectric ceramics will turn to

random distribution (depolarization), resulting in a decrease or disappearance of the piezoelectric coefficient. That is, piezoelectric materials can exhibit piezoelectricity only when the temperature is lower than the $T_c$. While the actual use temperature of piezoelectric ceramics is generally much lower than its Curie temperature. The commercial PZT piezoelectric ceramics have a $T_c$ of 365 °C, but their actual use temperature is only 200 °C due to the occurrence of depolarization at high temperatures [25, 26]. Therefore, it is first necessary to explore a ferroelectric system with a high $T_c$ for the development of high-temperature piezoelectric ceramics applications [27].

## 1.2.1 High Curie temperature piezoelectric ceramics

(1) Bismuth layer structure

The chemical formula of bismuth layer structure ferroelectrics is $(Bi_2O_2)^{2+}(A_{m-1}B_mO_{3m+1})^{2-}$, where A and B represent the cations at the A- and B-sites, and m is the number of octahedral layers, which ranges from 1 to 6. The basic feature of the structure is that the $(Bi_2O_2)^{2+}$ layer separates the quasi-perovskite layer $(A_{m-1}B_mO_{3m+1})^{2-}$ and is arranged according to certain rules. Several bismuth layered structure ferroelectric ceramics are commonly studied, such as $Bi_4Ti_3O_{12}$ (m=3), $CaBi_4Ti_4O_{15}$ (m=4), $SrBi_2Nb_2O_9$ (m=2), $Bi_3TiNbO_9$ (m=2) and $SrBi_4Ti_4O_{15}$ (m=4). This system is widely used in high-temperature sensors because of its high Curie temperature (500 °C-900 °C), low dielectric constant, low aging rates, high anisotropic electromechanical properties and high mechanical quality factor. However, the large coercive field makes the ceramics quite difficult to be poled; only a small piezoelectric coefficient $d_{33}$ (<20 pC/N) can be realized [28, 29]. The piezoelectric properties can be improved to some extent by the texturing process [30, 31] and suitable chemical doping [32, 33], but the piezoelectric coefficient $d_{33}$ of modified bismuth layered structured ferroelectrics remain less than 50 pC/N due to its inherent low piezoelectric activity.

(2) Tungsten bronze structure

The chemical formula of tungsten bronze structure ferroelectrics is $(A1)_2(A2)_4(C)_4(B1)_2(B2)_8O_{30}$. The $BO_6$ oxygen octahedra are connected as vertices to form the skeleton of the whole structure, stacked in a plane perpendicular to the fourfold axis and with different orientations. This particular organization facilitates the modification of the structure and the material properties. Among them, $PbNb_2O_6$ (PN) is the most widely studied tungsten bronze structure ferroelectric, which shows a high Curie temperature (about 570 °C), an ultralow mechanical factor (large bandwidth), and a high piezoelectric coefficient anisotropy ($d_{33}/d_{31}$) [34, 35]. However, the PN ceramics are easy to deform and crack during the preparation process, the quality of the ceramics is poor, which restricts its wide application and development. The difficult sintering for PN based ceramics is generally improved by the ion doping and the addition of sintering aids. For example, using $Ba^{2+}$ to replace $Pb^{2+}$ can effectively promote the sintering process of PN ceramics, thereby increasing its piezoelectric coefficient ($d_{33}$~180 pC/N), while reducing the Curie temperature ($T_c$~400 °C) [36].

(3) Corundum Structure:

The $LiNbO_3$ ferroelectric with corundum structure shows ultra-high Curie temperatures ($T_c$~1150 °C), which is widely used in transducers and sensor devices. The Czochralski method is generally used to prepare $LiNbO_3$ single crystal, and the polarization process is completed by applying a relatively small electric field at a temperature slightly lower than $T_c$. One disadvantage of $LiNbO_3$ is that the piezoelectric coefficient is very low ($d_{33}$~~6 pC/N) [37, 38]. In addition, $LiTaO_3$ single crystal is another widely studied corundum-type structure ferroelectric [39], with a $T_c$ of 720 °C, a piezoelectric coefficient $d_{33}$ of 9 pC/N, and a pyroelectric coefficient of $-1.8\times10^4$ C/m$^2$K [24, 40]. Although this system shows a high Curie temperature, its usage temperature range generally does not exceed 600 °C due to the decrease in resistance at high temperature [24].

(4) Perovskite structure:

As mentioned above, perovskite is one of the most important structure in ferroelectric materials. The $PbTiO_3$ (PT) has a $T_c$ of 490 °C, however, in order to

avoid cracking during sintering and poling processes, the PT must be modified to reduce the tetragonality *c/a* [41, 42]. For the lead-free (K,Na)$NbO_3$ (KNN) system, doping with $Li^+$ can increase its $T_c$ to 479 °C, and has a piezoelectric coefficient $d_{33}$~176 pC/N [43-45]. However, the high sintering process requirements limit the use of this system in practical applications. Another lead-free system, $BiFeO_3$ (BFO), possesses a $T_c$ of 830 °C and a large spontaneous polarization. These features make it a very promising high-temperature piezoelectric ceramic [46]. In 2015, Song et al. [47] prepared $BiFeO_3$-$BaTiO_3$-based piezoelectric ceramics by a water-quenching process, and the system shows a high Curie temperature ($T_c$~454 °C) and a high piezoelectric coefficient ($d_{33}$~402 pC/N), which is comparable to that of commercial PZT systems, as shown in Fig. 1.6. In addition, the Bi(Me)$O_3$-$PbTiO_3$ binary solid solution has the advantages of a high Curie temperature and a high piezoelectric response. Such ferroelectric systems summarized in Fig. 1.7 [24-26, 32-33, 48-56] possess a perovskite structure and a high piezoelectric response. This makes them suitable for applications in workable devices.

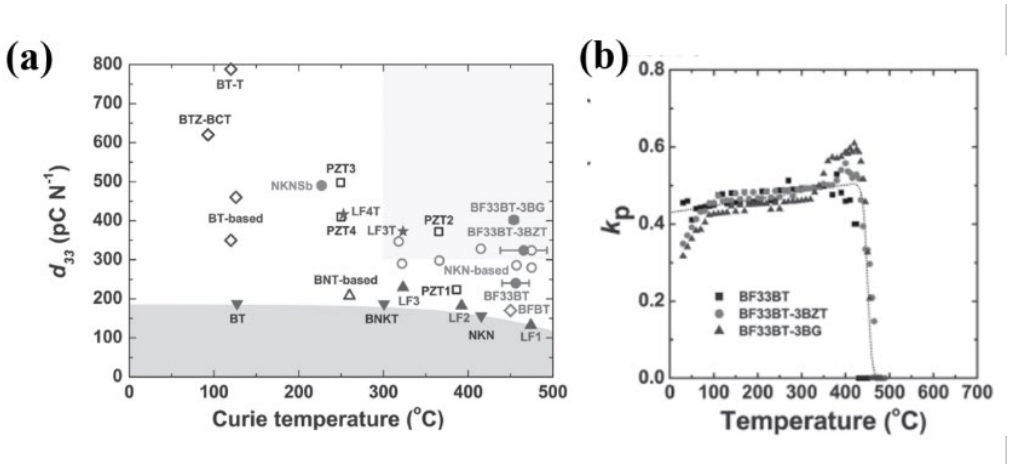


**Figure 1.6** (a) The $d_{33}$ and $T_c$ of various piezoceramics; (b) The $k_p$ of $BiFeO_3$-$BaTiO_3$ based ternary ceramics versus temperature [47].

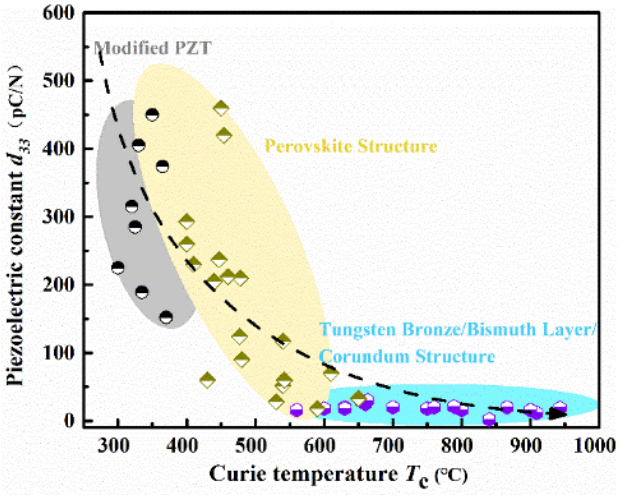


**Figure 1.7** The $d_{33}$ and $T_c$ for different kinds of high-temperature piezoelectric ceramics.

## 1.2.2 Advances in $Bi(Me)O_3$-$PbTiO_3$-based ceramics

$Bi(Me)O_3$-$PbTiO_3$ binary solid solution is a promising high-temperature piezoelectric ceramic, where Me is metal cations such as Sc、Fe、In、Yb、Y, also includes $Mg_{1/2}Ti_{1/2}$、$Zn_{1/2}Ti_{1/2}$、$Ni_{1/3}Nb_{2/3}$、$Ni_{1/2}Ti_{1/2}$ and other ions based composites. The most representative of this system is (1-x)$BiScO_3$-x$PbTiO_3$ (BS-PT) based high-temperature piezoelectric ceramics, which were first designed and synthesized by Eitel et al. [57, 58] in 2001. It was found that the 0.36BS-0.64PT ceramic with the MPB structure exhibits excellent properties: Curie temperature $T_c$~450 °C, piezoelectric coefficient $d_{33}$~450 pC/N, residual polarization strength $P_r$~32 μC/cm$^2$, and planar electromechanical coupling coefficient $k_p$~0.56, which shows great application potential in the field of high-temperature piezoelectric devices. However, the high cost of Sc limits the large-scale production and application for BS-PT based ceramics. Cheng et al. [59] first prepared $BiGaO_3$-$PbTiO_3$ (BG-PT) piezoelectric ceramics with a tetragonal phase structure, and the ferroelectric-paraelectric phase transition temperature is about 495 °C by differential scanning calorimetry. The relative dielectric constant of BG-PT ceramic is about 200, but its ferroelectric properties were not characterized. In addition, pure $BiInO_3$-$PbTiO_3$ (BI-PT) ceramics were prepared by the sol-gel method [60], with tetragonality $c/a$~1.082 and Curie temperature $T_c$~582 °C, but the ceramics were difficult to pole. Zhang et al. [61] found

the pure BI-PT-based ceramics can be prepared by solid-state reaction method when the PT content is higher than 75 %. They also studied the performance of 0.15BI-0.85PT+1.5mol%Nb ceramic which exhibited excellent properties: $T_c$~542 °C, $d_{33}$~60 pC/N, $d_{15}$~80 pC/N. Gao et al. [62] found that although $BiYbO_3$-$PbTiO_3$ (BY-PT) piezoelectric ceramics show a high Curie temperature $T_c$~590 °C, the pyrochlore phase $Yb_2Ti_2O_7$ is easily produced during the preparation process, which leads to a low piezoelectric coefficient $d_{33}$~17 pC/N. It was also found that BY-PT-BT ternary solid solutions show a reduced Curie temperature $T_c$~505 °C, while their piezoelectric coefficient slightly increases ($d_{33}$~34 pC/N) [63].

The $Bi(Me)O_3$-$PbTiO_3$ based piezoelectric ceramics in which Me is the composite ions also have been extensively studied. Randall et al. [64] first prepared (1-x)$Bi(Mg_{1/2}Ti_{1/2})O_3$-x$PbTiO_3$-based ceramics and systematically investigated their structure and piezoelectric properties. It was found that the composition near x=0.37 is located at the MPB and shows a high piezoelectric coefficient $d_{33}$~220 pC/N and a high Curie temperature $T_c$~478 °C. Similarly, $Bi(Ni_{2/3}Nb_{1/3})O_3$-x$PbTiO_3$ based piezoelectric ceramics also have a MPB structure, but the Curie temperature of the MPB composition is only 275 °C[65]. Yu et al. [66] prepared $Bi(Zn_{1/2}Ti_{1/2})O_3$-$PbTiO_3$-$BiFeO_3$ based piezoelectric ceramics using a multiple calcination process, and the MPB composition shows the excellent performance: $T_c$~560 °C, $d_{33}$~30 pC/N and tan$\delta$~0.02. In fact, there are many $Bi(Me)O_3$-$PbTiO_3$ based piezoelectric ceramics that have been prepared and studied [57, 59, 61-62, 67-70], as shown in Table 1.1. It can be seen from Table 1.1 that all of these materials have relatively high Curie temperatures, but the piezoelectric coefficients of all compositions except BS-PT are on the low side. In general, an increase in piezoelectric coefficient is accompanied by a decrease in Curie temperature for the ceramics. It should be pointed out that $BiFeO_3$-$PbTiO_3$ based piezoelectric ceramics with the MPB structure have a high Curie temperature $T_c$~600 °C, which will be introduced in detail in the next section.

**Table 1.1** The electric properties of $Bi(Me)O_3$-$PbTiO_3$ based ceramics.

| Materials | $T_c$ (°C) | $d_{33}$ (pC/N) | $k_p$ (%) | tan$\delta$ | Rf |
|---|---|---|---|---|---|
| $0.36BiScO_3$-$0.64PbTiO_3$ | 450 | 460 | 0.56 | 0.027 | [57] |
| $BiGaO_3$-$PbTiO_3$ | 495 | - | - | 0.032 | [59] |
| $BiFeO_3$-$PbTiO_3$ | 650 | | | 0.035 | [67] |
| $BiInO_3$-$PbTiO_3$+Nb | 542 | 60 | 0.11 | 0.02 | [61] |
| $BiYbO_3$-$PbTiO_3$ | 590 | 18 | - | 0.02 | [62] |
| $Bi(Mg_{1/2}Ti_{1/2})O_3$-$PbTiO_3$ | 478 | 220 | - | 0.063 | [64] |
| $Bi(Ga_{0.4}Fe_{0.6})O_3$-$PbTiO_3$ | 540 | 52 | - | 0.03 | [68] |
| $Bi(Ni_{2/3}Nb_{1/3})O_3$-$PbTiO_3$ | 273 | 140 | 0.22 | 0.11 | [65] |
| $Bi(Ni_{1/2}Ti_{1/2})O_3$-$PbTiO_3$ | 400 | 260 | | | [69] |
| $Bi(Zn_{1/2}Ti_{1/2})O_3$-$PbTiO_3$ | 700 | - | - | - | [70] |
| $Bi(Zn_{1/2}Ti_{1/2})O_3$-$PbTiO_3$-$BiFeO_3$ | 560 | 30 | - | 0.02 | [66] |

Eitel et al. [58] designed high-performance BS-PT-based high-temperature piezoelectric ceramics and concluded that the Curie temperature of $Bi(Me)O_3$-$PbTiO_3$ systems at the morphotropic phase boundary MPB increases as the tolerance factor of the $Bi(Me)O_3$ of the solid solution decreases. The tolerance factors of $BiScO_3$, $BiInO_3$ and $BiYbO_3$ are 0.907, 0.884 and 0.857, respectively, and the Curie temperatures of $BiScO_3$-$PbTiO_3$, $BiInO_3$-$PbTiO_3$ and $BiYbO_3$-$PbTiO_3$ at the MPB can reach about 450°C, 550°C and 600°C, respectively. Based on the experimental results, Suchomel et al. [71] also suggested that the tolerance factor of $Bi(Me)O_3$ can be used to qualitatively predict the position of the MPB for $Bi(Me)O_3$-$PbTiO_3$ system, that is, the position of MPB shifts towards the $PbTiO_3$-rich direction with the decrease of $Bi(Me)O_3$ tolerance factor. For the perovskite structure with a small tolerance factor, the B-site ions prefer a larger volume than the A-site ions, which results in the increase of A-site displacements when the A-site is occupied by the ferroelectrically active ions Pb and Bi [72]. It is generally found that the Curie temperature is proportional to the square of ionic displacements. Therefore, the small tolerance factor of the Bi-based perovskite structure means a large ionic displacement, which leads to a high Curie temperature

[73]. Grinberg et al. [72] used density-functional-theory calculations to predict more quantitatively the position of the MPB for $Bi(Me)O_3$-$PbTiO_3$ system. The relationship between the Curie temperature and the tolerance factor can be classified into two different categories depending on the Me ion species, i.e., B sites occupied by ferroelectrically active ions or non-ferroelectrically active ions, as shown in Fig. 1.8. In addition, Stringer et al. [74] proposed the concept of the tolerance factor difference ($\Delta t$=$|t_{Bi(Me)O_3}$-$t_{PbTiO_3}|$) and suggested that for every 0.01 increase in $\Delta t$, the Curie temperature of the $Bi(Me)O_3$-$PbTiO_3$ system increases by 12 °C compared to pure $PbTiO_3$ ($T_c$~490 °C).

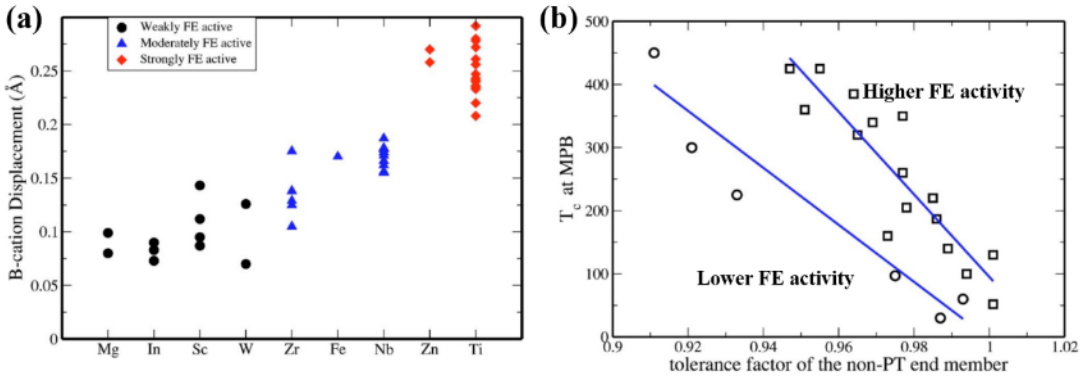


**Figure 1.8** (a) Distortion for the B cation in PT solid solutions; (b) $T_c$ of $Bi(Me)O_3$-$PbTiO_3$ based ceramics at MPB vs tolerance factor of $Bi(Me)O_3$ [73].

# 1.3 Advances in $BiFeO_3$-based ceramics

## 1.3.1 Overview of $BiFeO_3$-based ceramics

Bismuth ferrite ($BiFeO_3$, abbreviated as BFO) is an attractive lead-free ferroelectric material owing to the electron configuration of $Bi^{3+}$ being similar to $Pb^{2+}$ (lone $6s^2$ electron configuration) [46, 75]. BFO ceramics with distorted perovskite structure (space group R3c) show a G-type canted antiferromagnetic order below the Néel temperature ($T_N$~370 °C) and ferroelectric behavior below the Curie temperature ($T_c$~ 830 °C). According to theoretical calculations, the spontaneous polarization along the [111] direction of BFO is as high as 100 μC/cm$^2$, which is

comparable to that of traditional perovskite-type ferroelectrics BT and PT [76], as shown in Fig. 1.9. Experimentally, Wang et al. [77] successfully prepared the pure phase BFO thin films with high quality by the pulsed laser deposition (PLD) method for the first time, and the spontaneous polarization along the [001] direction reached 60 μC/cm$^2$. On the basis of this method, Li et al. [78] also prepared BFO thin films with spontaneous polarization along the [001] direction up to 100 μC/cm$^2$. These experimental results further confirm that BFO with large spontaneous polarization is a very promising ferroelectric material. However, BFO ceramics possess the feature of a semiconducting material with a bandgap (2.7 eV) at room temperature, and the pure BFO ceramic is difficult to stabilize due to the formation of secondary phases such as $Bi_2Fe_4O_9$ and $Bi_{25}FeO_{40}$ during the sintering process [46], which limit its application and development in the field of ferroelectric ceramics.

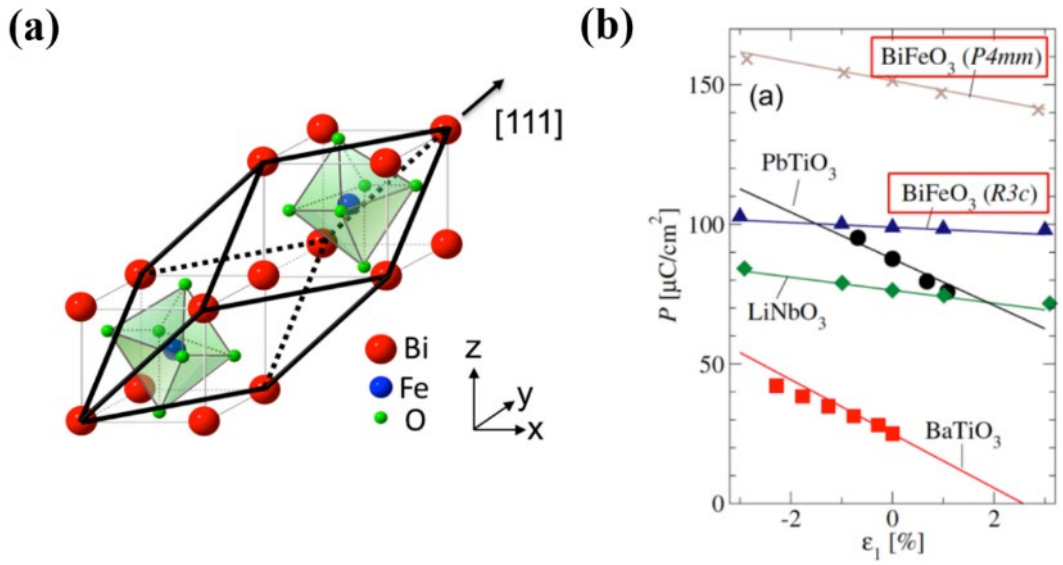


**Figure 1.9** (a) Structure of $BiFeO_3$ [75]; (b) The polarization for $BiFeO_3$, $BaTiO_3$, $PbTiO_3$ and $LiNbO_3$ as a function of epitaxial strain [76].

In 2004, Wang et al. [79] prepared a pure phase of BFO by a rapid liquid phase sintering technique. This material shows saturated hysteresis *P-E* loops that were as shown in Fig. 1.10. The generation of $Fe^{2+}$ and oxygen vacancies of BFO ceramics can be greatly suppressed by a very high heating rate and a short sintering time,

leading to the decrease of leakage current. In addition, the special processes for preparing pure phase BFO ceramics include microwave sintering, spark plasma sintering and sol-gel method [80-82], which will not be described in detail here.

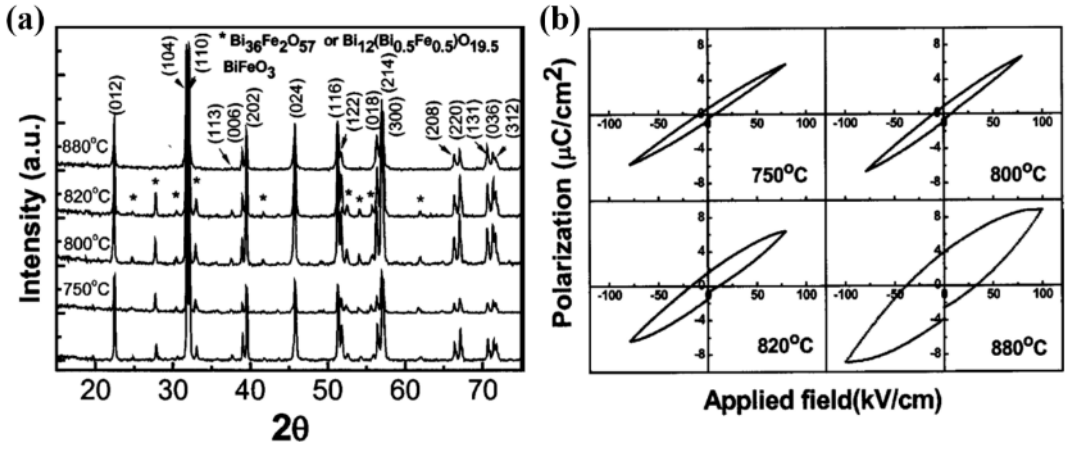


**Figure 1.10** (a) XRD pattern from the $BiFeO_3$ ceramic samples synthesized by the rapid sintering process and the conventional solid-state reaction; (b)The hysteresis loops of $BiFeO_3$ ceramics sintered by the rapid liquid phase sintering process at different temperatures [79].

On the other hand, the A- and B-site doping of BFO ceramics is also an effective way to improve their electrical properties. B-site substitution, mainly includes La, Sm, Nd, Yb, Ce, Dy, and Gd. For example, Chen et al. [83] reported that the Sm-doped $BiFeO_3$ ceramics have excellent electrical properties: piezoelectric coefficient $d_{33}$~45 pC/N, remnant polarization $P_r$~40 μC/cm$^2$, and Curie temperature $T_c$~550 ℃. A high piezoelectric coefficient ($d_{33}$~50 pC/N) and a high Curie temperature ($T_c$~550 ℃) can be achieved in La and Sm co-doped BFO ceramics [84]. In these reports, the main reason for the improvement of ferroelectric performance was attributed to the fact that doping elements can effectively reduce the leakage current of BFO ceramics by inhibiting the generation of impurity phases and $Fe^{2+}$ ions. While the relationship between phase structure (phase boundary) and performance improvement was rarely discussed. Yuan et al. [85] found that with the increase of La doping content, the phase structure of the $(Bi,La)FeO_3$ ceramic gradually changed from rhombohedral to triclinic and then to pseudo-tetragonal

phase, however, the piezoelectric coefficient decreased monotonically with the increase of La doping content. The results suggest that the phase boundary does not greatly affect the electrical properties of BFO ceramics. The evolution of phase structure and piezoelectric coefficient of BFO ceramics doped with different rare earth elements (Eu, Pr, Sm, La, Dy) are shown in Fig. 1.11 [86]. It can be found that the highest $d_{33}$ value can be achieved in doped-BFO ceramics (Eu, Pr, Sm and Dy) with rhombohedral phase. While the physical mechanism of the relationship between the rhombohedral phase structure and enhanced piezoelectricity has not been elucidated.

The substitution of Fe ions at the B-site mainly modifies the magnetic properties of BFO ceramics, and the effect on its ferroelectric properties is less pronounced than that of the A-site substitution. One of the representative element, Sc, can reduce the leakage current of ceramics, which is beneficial to obtain BFO ceramics with a high piezoelectric coefficient ($d_{33}$~46 pC/N) [87]. Also, co-substitution of A- and B-site has been widely studied, such as Sm+Sc, La+Ga, and Y+Mn [87-89]. Overall, cation substitution is beneficial to the preparation of BFO ceramics with a pure phase and low leakage current, which can effectively improve its ferroelectric and electrical properties. However, a large number of studies have shown that it is difficult to obtain the morphotropic phase boundary for BFO ceramics by cation substitution and then the enhancement of their piezoelectric properties is limited, with $d_{33}$ ranging from about 40 to 50 pC/N.

Thus, the $ABO_3$-type perovskite structure is introduced into BFO-based ceramics to further modify their ferroelectric and piezoelectric properties. Among them, the $BiFeO_3$-$PbTiO_3$ (BF-PT) with a rhombohedral-tetragonal phase boundary and the $BiFeO_3$-$BaTiO_3$ (BF-BT) with a rhombohedral-pseudo-cubic phase boundary are the two typical candidate materials, which will be introduced in detail below.

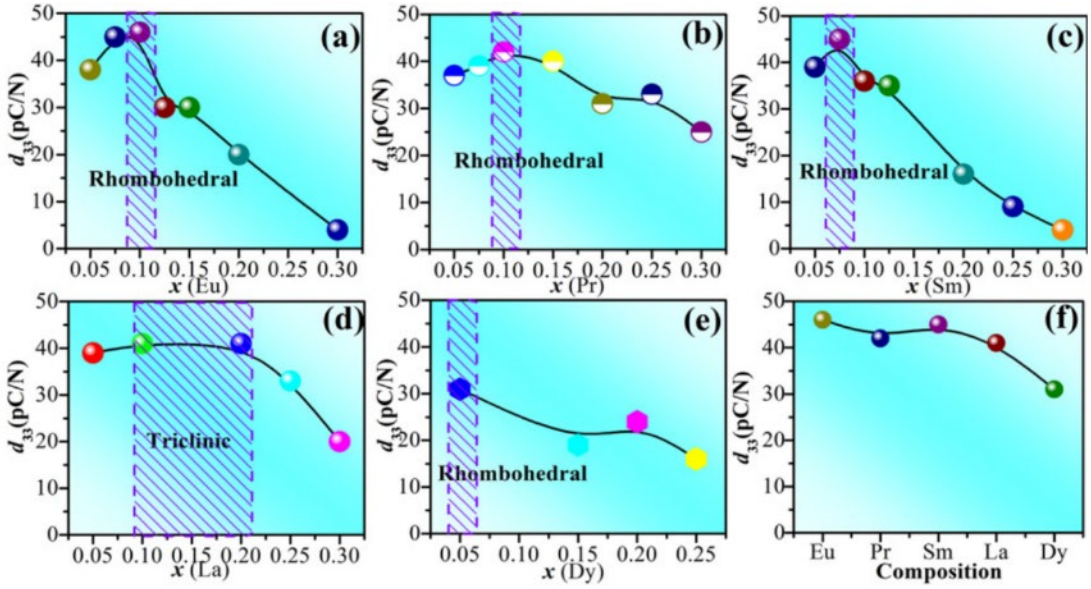


**Figure 1.11** The piezoelectric coefficient $d_{33}$ of BFO ceramics doped with different rare earth elements (Eu, Pr, Sm, La, Dy) [86].

## 1.3.2 Overview of $BiFeO_3$-$PbTiO_3$ ceramics

In the 1970s, Smith et al. [67] first reported $xBiFeO_3$-$(1-x)PbTiO_3$ (xBF-PT) binary solid solution, which attracted the attention of many researchers due to its high Curie temperature and the presence of morphotropic phase boundary. It remains controversial for the position and the width of the MPB in the xBF-PT based ceramics. Earliest, Fedulov et al. [90] suggested that the existence of a rhombohedral-tetragonal phase boundary in the xBF-PT system, located at the composition with x~0.66-0.73. In the MPB region, the ceramics exhibit a high Curie temperature up to about 700 °C. Subsequently, in 2003, Woodward et al. [91] proved that the MPB of the xBF-PT system is located at the composition with x~0.6-0.7 by the analysis of XRD and TEM. The coexistence of lamellar and perturbed domain structures can be obtained in the 0.7BF-0.3PT ceramics with the MPB. In addition, Ye et al. [92] reported the existence of MPB region in the composition with x~0.69-0.83. They revealed for the first time that not only the rhombohedral and tetragonal phase but also the orthorhombic phase was found at the MPB composition, as shown in Fig. 1.12.

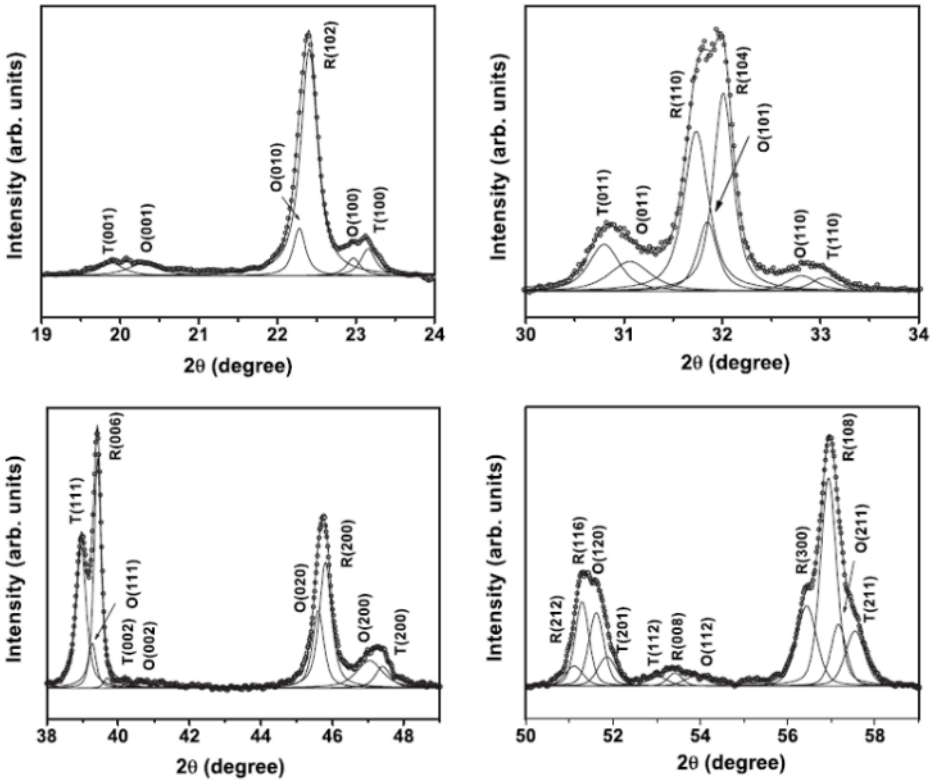


**Figure 1.12** XRD pattern of 72BF-28PT ceramics, in which the dots are the experimental data and the solid lines are the fitting data [92].

Bhattacharjee et al. [93] systematically studied the phase structure of the xBF-PT system. Firstly, in 2007, they proposed that the MPB of the xBF-PT system is located at the composition with 0.69<x<0.73, and the width of the phase boundary is only 0.03, which is much smaller than that reported previously. Subsequently, the coexistence of the monoclinic phase *Cc* and the tetragonal phase *P4mm* were observed in the MPB composition by the powder neutron diffraction [94-96]. Fig. 1.13 shows the evolution of the phase structure of the BF-PT ceramics before and after annealing. It can be seen that the internal stress of the BF-PT ceramic will lead to an increase in the width of the MPB [97]. Recently, Hooper et al. [98] constructed a Landau–Devonshire derived phase diagram of BF-PT binary solid solution, as shown in Figure 1.14. It can be found that the MPB (rhombohedral-tetragonal) is located at

0.696BF-0.304PT. There is controversy in the location of the phase boundary reported in different studies, which is mainly related to the large internal stress of the BF-PT based ceramics. Generally speaking, the grinding, polishing, crushing and annealing processes can have a large impact on the XRD structural characterization.

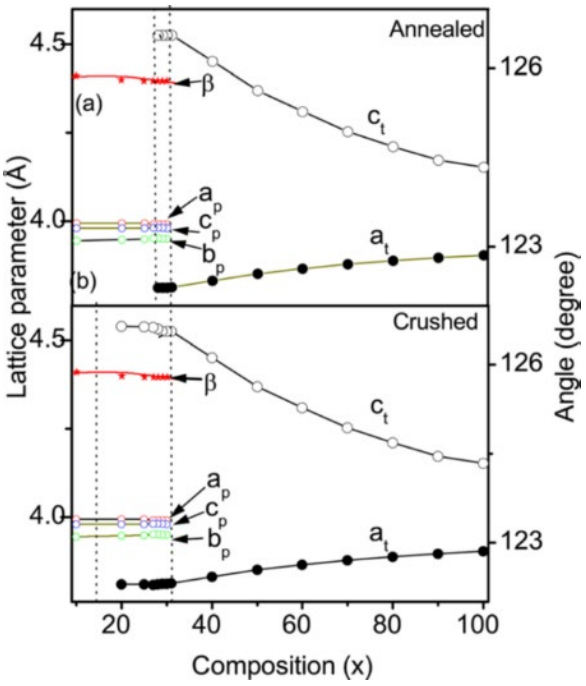


**Figure 1.13** Lattice parameters of (1-x)BF-xPT binary solid solution [97].

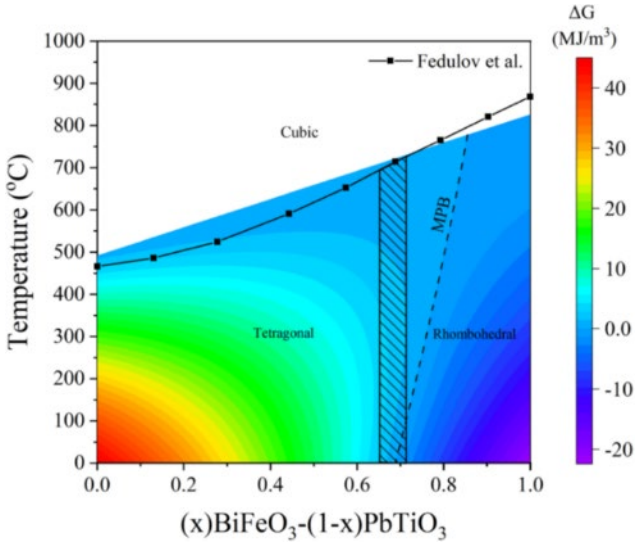


**Figure 1.14** Landau–Devonshire derived structural phase diagram of (1-x)BF-xPT solid solution [98].

It is worth noting that the BF-PT based ceramics near the MPB composition

show the largest tetragonality ($c/a$~1.18), which is much larger than that of the reported ferroelectric oxide perovskite [99]. However, the large tetragonality of ferroelectric ceramics leads to the high internal stress occurring at the transition temperature, which makes it different for the preparation of ceramics [100]. Besides, such a huge tetragonality of ferroelectric ceramics would suppress the domain switching, which leads to a decrease in piezoelectricity [101-102]. Therefore, in order to improve the electrical properties of the BF-PT system, it is necessary to reduce its abnormally large tetragonality $c/a$.

It is critical to find out the origin of such a huge tetragonality for the improvement of the BF-PT system. Similar to BF-PT, the tetragonality of $Bi(Zn,Ti)O_3$-PT and $Bi(Zn,Nb)O_3$-PT compounds increases with the decrease of PT content [103, 104]. Matthew et al. [70] systematically examined the structure of $PbTiO_3$-$Bi(B_1B_2)O_3$ solid solutions, where $B_1B_2$ is taken as $(Zn_{1/2}Ti_{1/2})^{3+}$, $(Zn_{1/2}Zr_{1/2})^{3+}$, and $(Zn_{1/2}Sn_{1/2})^{3+}$, respectively, suggesting that only when the B-site is completely filled with ferroelectrically active cations ($Ti^{4+}$, $Zn^{2+}$) are likely to exhibit a huge tetragonality. They also revealed that the large tetragonal distortions were ascribed from a strong coupling between the A- and B-site off-center distortions. For the BF-PT system, it was shown that the partial covalent character of the Ti/Fe-O and Pb/Bi-O bonds leads to the shorter and longer pairs of bond lengths, which would be a key factor for the large tetragonality. Meanwhile, the ferroelastic coupled with magnetoelectric effect was another possible reason [93]. According to the MEM analyses of synchrotron diffraction data and first principles DFT calculations, Yashima et al. [105] proposed that the strong hybridization of (Bi,Pb)(6s,6p) and O(2p) orbitals for the BF-PT system was the main origin for its abnormally large tetragonality, as shown in Fig. 1.15.

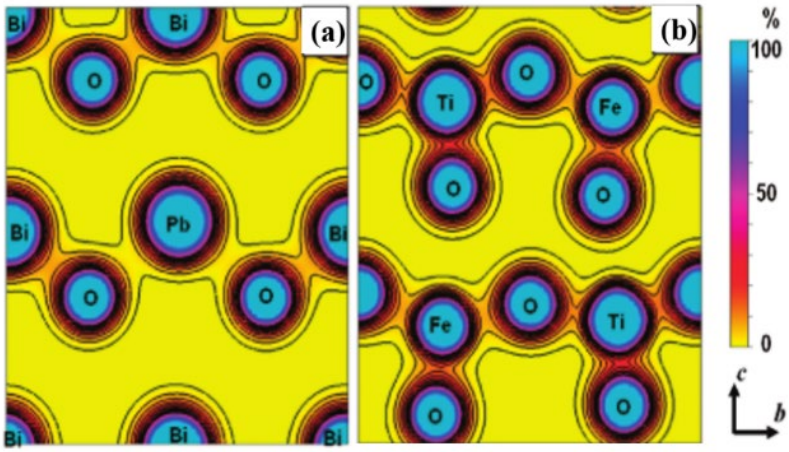


**Figure 1.15** Valence electron density distributions on the bc planes of 0.67BF-0.33PT ceramics [105].

Considering the high Curie temperature of the BF-PT system, several works so far have focused on the enhancement of its piezoelectric properties for the high-temperature application. Cheng et al. [68, 106-112] have made a large contribution on the modified BF-PT based piezoelectric ceramics, and good progresses were achieved. For example, the doping of $Ga^{3+}$ and $Mn^{2+}$ can effectively improve the insulation of ceramics; the addition of $Ga^{3+}$ increases the resistivity from $10^9$ Ωcm by 3 orders of magnitude to $10^{12}$ Ωcm; the addition of $La^{3+}$ significantly promotes the rotation of domains and reduces the coercive field, which leads to the high ferroelectric properties; a high piezoelectric coefficient ($d_{33}$~117 pC/N) and a high Curie temperature ($T_c$~450 °C) can be obtained in BF-PT ceramics doped with $Ti^{4+}$. In addition, Zuo et al. [113] also compared the effects of different doping elements on the properties of BF-PT systems and found that $Ta^{5+}$, $Nb^{5+}$, and $La^{3+}$ ion was more favorable for the preparation of improved electrical resistance ceramics, compared to $V^{5+}$, $Li^{+}$, and $Zn^{2+}$. According to the results of AC impedance spectroscopy, Ye et al. [114] concluded that the conduction mechanism of BF-PT based ceramics mainly comes from the hopping of electrons between $Fe^{2+}$ and $Fe^{3+}$, while the contribution of ion conduction is not significant. For BF-PT-based ternary solid solutions, Fan et al. [115] found that the addition of $BaZrO_3$ into BF-PT ceramics could effectively reduce the tetragonality *c/a* from 1.18 to 1.02, thus promoting the domain switching

and increasing their piezoelectric coefficient ($d_{33}$~270 pC/N). However, BF-PT-BZ system exhibits a low Curie temperature ($T_c$~270 °C), which is not favorable for piezoelectric devices at high temperatures. According to the phase diagram of the $BiFeO_3$-$PbTiO_3$-$PbZrO_3$ ternary system [116, 117], the composition at the MPB with piezoelectric coefficient of 64 pC/N and Curie temperature of 560 °C can be achieved in this system. It is worth mentioning that in 2018 Ranjan et al. [118] designed $BiFeO_3$-$PbTiO_3$-$LaFeO_3$ ternary solid solutions with an ultrahigh electrostrain ($S$~1.3 %), which is the maximum strain value reported in polycrystalline ceramics, as shown in Fig. 1.16. They also revealed that the ultrahigh electrostrain is mainly originated from the large spontaneous lattice strain, the domain miniaturization, and the large reverse switching of the non-180° domains. All in all, BF-PT-based ceramics with unique structures (MPB, ultrahigh *c/a*) and high Curie temperature are a very promising high-temperature piezoelectric ceramic. The main issues include: how to suppress the formation of charged defects to improve the insulation of ceramics, how to reduce the tetragonality to improve the domain switching, and how to balance the Curie temperature and the piezoelectric properties.

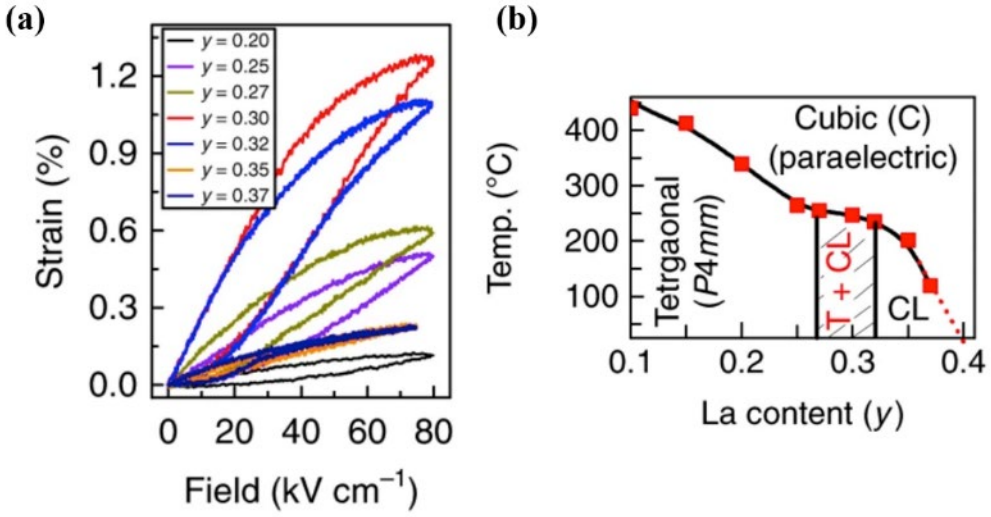


**Figure 16** (a) The unipolar strain-electric-field curve of $0.55Bi_{1-y}La_yFeO_3$-$0.45PbTiO_3$ for different La concentration; (b) The phase diagram of BLF-PT based ceramics [118].

### 1.3.3 Overview of $BiFeO_3$-$BaTiO_3$ ceramics

The $BiFeO_3$-$BaTiO_3$ binary solid solution with a morphotropic phase boundary is a class of lead-free system with excellent performance. In 2000, Mahesh et al. [119] studied the variation of the lattice parameters of the BF-BT binary solid solution with BFO content, as shown in Fig. 1.17(a). It can be seen that with the decrease of the BFO content, the structure gradually changes from the rhombohedral phase to the cubic phase and finally transforms to the tetragonal phase. Thus, BF-xBT system has rhombohedral-cubic and cubic-tetragonal phase boundaries, which are located at the BFO content of 67 % and 6 %, respectively. According to the results of the dielectric properties and the differential scanning calorimetry, Leontsev et al. [120] make some corrections on the basis of Mahesh' phase diagram, as shown in Fig. 1.17(b). It shown that a pseudo-cubic phase appears in the composition range of x~0.25-0.4. The cubic phase of BF-BT system is identified by the absence of splitting peaks in the XRD pattern, but the XPD only reflects the average structure of the crystal. Combined with superlattice diffraction spots of rhombohedral from TEM and the analysis of ferroelectric properties, it can be seen that this average cubic structure is not a completely symmetrical structure. In fact, BF-BT ceramics have a structure in which the polar phase distributed in the cubic matrix, this ferroelectric structure defined as a pseudo-cubic phase [121, 122]. In addition, considerable research efforts have been devoted to the improvement of the piezoelectric properties for the BF-BT system [47, 121-123]. For example, as mentioned above, the modified BF-BT ceramics prepared by a water-quenching process have a high piezoelectric coefficient while maintaining a high Curie temperature, which is comparable to that of lead-based ceramics [47]. The reasons for the enhancement of the ferroelectric and piezoelectric properties for the BF-BT system are similar to those of the BF-PT system, which are mainly derived from a combination of several factors: the formation of morphotropic phase boundary, the reduction of leakage current, and a dense ceramic. It should be pointed out that the BF-BT system with pseudo-cubic structure is often accompanied by large electrostrain and polarization response under an electric field. This feature

indicates that the BF-BT system has great application prospects in the fields of electrostrain and energy storage.

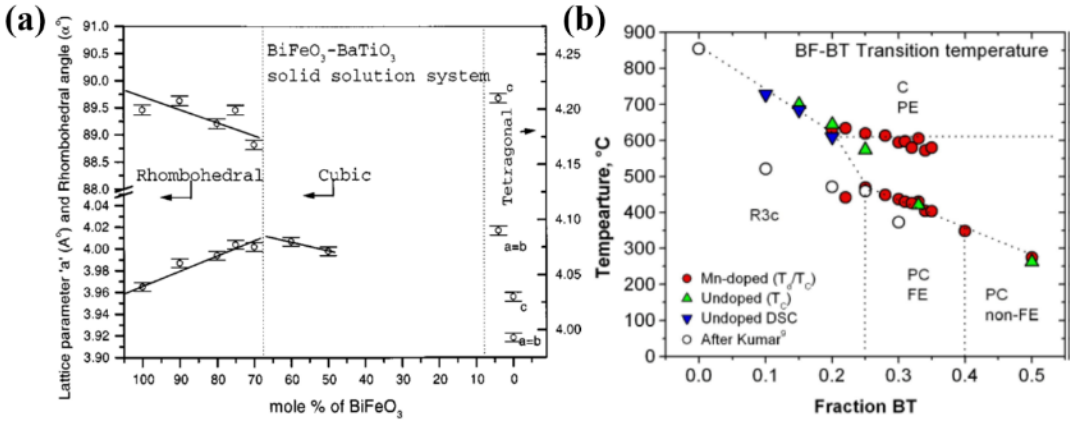


**Figure 17** (a) Variation of lattice parameters for the BF-BT system [119]; (b) Revised phase diagram for the BF-BT system [120].

In recent decades, particular attentions have been drawn for the ferroelectric capacitors, which have been widely investigated as promising candidates for energy storage devices because of their high energy density and fast charge-discharge capabilities [124-126]. Generally, the energy density of ferroelectric materials mainly derives from the switching of the reversible domain under an electric field, which is calculated by the following equation:

$$W = \int_0^{P_{max}} EdP \quad \ldots(1.2)$$

$$W_{re} = \int_{P_r}^{P_{max}} EdP \quad \ldots(1.3)$$

$$\eta = \frac{W_{re}}{W} \quad \ldots(1.4)$$

where $W$ and $W_{re}$ represent the total energy density and the recoverable energy density, $P_{max}$ and $P_r$ represent the maximum polarization and the remnant polarization at the electric field, $\eta$ is the energy storage efficiency. Hence, in order to design relevant ferroelectric structures with a high recoverable energy density, the main requirement lies in a large polarization difference $\triangle P$ ($\triangle P = P_{max}-P_r$) along with a high dielectric breakdown strength ($E_b$). Lead-free BF-BT based ceramic is an attractive lead-free ferroelectric with a large polarization, which offers exciting

opportunities to the energy storage materials. The reversible energy storage density of 1.56 J/cm$^3$ and 1.66 J/cm$^3$ can be obtained in the BF-BT-Ba($Mg_{1/3}Nb_{2/3}$)$O_3$ and BF-BT-La($Mg_{1/2}Ti_{1/2}$)$O_3$ system, respectively [127, 128]. Li et al. [129] investigated the energy storage performance of ($Sr_{0.7}Bi_{0.2}$)$TiO_3$-modified BF-BT based ceramics with a reversible energy storage density of 1.74 J/cm$^3$ and a fast discharge time of 25-30 ns, and found that the system shows the ergodic relaxor characteristics. Liu et al. [130, 131] designed two system, BF-BT-Sr($Al_{0.5}Nb_{0.5}$)$O_3$ and BF-BT-Ba($Zn_{1/2}Ta_{2/3}$)$O_3$ by the strategy of constructing weakly coupled short-range polar structures. Ultrahigh energy density of 1.74 J/cm$^3$ can be achieved in the 0.6BF-0.34BT-0.06BZT ceramics, which superior to the previous reports on BFO based ceramics, as shown in Fig. 1.18. The main strategy of these studies is to increase a local compositional disorder in the underlying structures by introducing non-isovalent cations into A- and B-site of BF-PT ceramics. As a consequence, a low remnant polarization and a high reversible energy storage density can be achieved in ferroelectric ceramics. In short, exploiting the energy storage applications for the BF-BT system is a promising work.

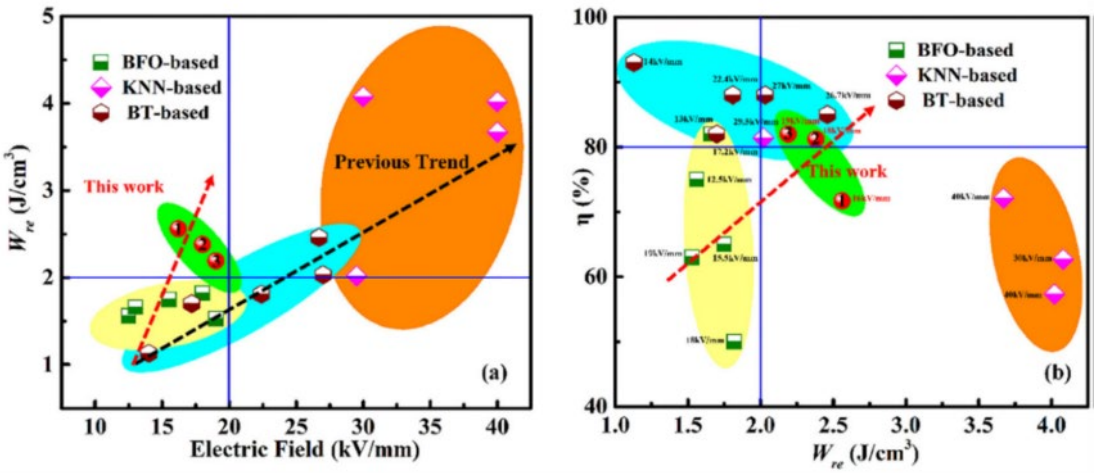


**Figure 1.18** A comparison of energy storage properties ($W_{re}$ and $\eta$) among the canonical lead-free ferroelectric ceramics [131].

# Chapter 2 Experimental procedures and characterization techniques

## 2.1 Raw materials

The chemical components for the experiments were selected as high-purity oxide and carbonate raw materials. Specific information about chemical raw materials is shown in Table 2.1.

**Table 2.1** Raw materials for BiFeO3-based ferroelectric ceramics

| Chemical components | Purity | Place of production |
|---|---|---|
| $Fe_2O_3$ | 99.77% | Aladdin chemical reagent company |
| $Bi_2O_3$ | 99.60% | Sinopharm chemical reagent company |
| PbO | 99.00% | Aladdin chemical reagent company |
| $Pb_3O_4$ | 96.69% | Sinopharm chemical reagent company |
| $TiO_2$ | 99.48% | Aladdin chemical reagent company |
| $BaCO_3$ | 99.80% | Sinopharm chemical reagent company |
| $ZrO_2$ | 99.84% | Kemiou chemical reagent company |
| $SnO_2$ | 99.50% | Aladdin chemical reagent company |
| MgO | 99.99% | Aladdin chemical reagent company |
| $Nb_2O_5$ | 99.99% | Aladdin chemical reagent company |
| PVA | - | Sinopharm chemical reagent company |

## 2.2 Preparation of $BiFeO_3$-based ceramics

The ceramic samples in this experiment were prepared by a conventional solid-state method, and the preparation process is shown in Fig. 2.1. The detailed preparation processes are as follows:

(1) Dry and weight: All raw materials were dried at 120 ℃ for 6 h to evaporate adsorbed water. Then, they were carefully weighted according to the stoichiometric ratio.

(2) One-time ball milling: The starting stoichiometric powders were wet mixed by the planetary ball milling for 8-10 h at 350 r/min, and the anhydrous ethanol is selected as the ball mill medium.

(3) Calcination: After drying, the precursor powders were calcined at 780 ℃ for 4 hours. The ramping rate is 5 ℃/min.

(4) Second-time ball milling: The resultant powders were ball milled again for 8 hours.

(5) Pressed into pellets: The dried powders were mixed with 8 wt.% polyvinyl alcohol (PVA), then pressed into pellet disks with a diameter of 12 mm and a thickness of 1.5 mm under the uniaxial pressure of 200 MPa.

(6) Remove organics: The pellets were slowly heated at 550 ℃ for 4 h to remove the binder. The ramping rate was 1 ℃/min.

(7) Sintering: The compacts were sintered at the temperature from 980 ℃ to 1020 ℃ for 2 hours. The ramping rate is 5 ℃/min. To decrease the volatilization of Bi and Pb, the sintered samples were surrounded by powders of the same composition.

(8) Coated electrode: A layer of silver paste was applied to the ceramic by screen printing, then the organic solvent was removed at a temperature of 720 ℃ to obtain a ceramic sample plated with electrodes.

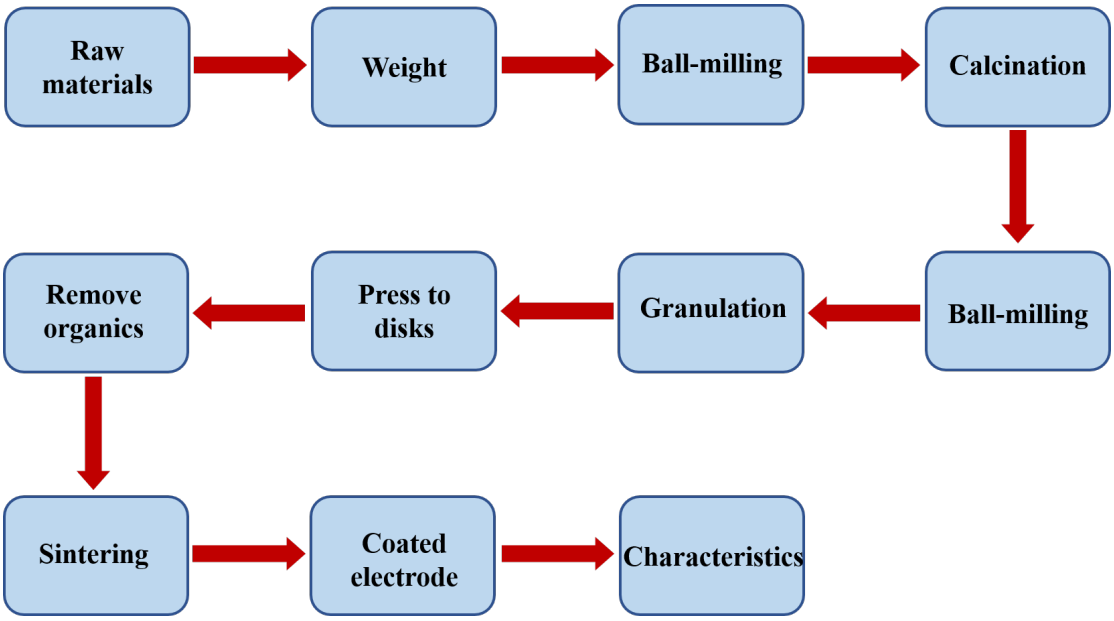


**Figure 2.1** Schematic of process of $BiFeO_3$-based ferroelectric ceramics.

## 2.3 X-ray diffraction (XRD)

XRD technique was used to qualitatively and quantitatively analyze phase structures and unit cell parameters of the $BiFeO_3$-based ceramics. The XRD experiments were performed on Rigaku D/max-2550V with the wavelength of Cu Kα1 is 0.15406 nm. The test voltage is 40 kV, the current is 30 mA, the scanning step is 0.02°, and the scanning range 2θ is between 10°-90°. The GSAS software based on the Rietveld method was used for the refinement of the XRD patterns to obtain quantitatively the phase structure and unit cell parameters of the ceramic samples. In addition, an XRF diffractometer (Empyrean-Panalytical) was used for the high temperature X-ray diffraction experiments.

## 2.4 Scanning electron microscopy (SEM)

The microscopic morphology and element composition of the $BiFeO_3$-based ceramics were characterized by scanning electron microscopy (SEM). Field emission scanning electron microscope (Hitachi S-4800) was used to characterize the surface morphology and the grain size of ceramics. In addition, an X-ray energy

spectrometer (EDS) is used to analyze the element's distribution of the grain and the grain boundary for the ceramic sample, and the content of each element can be obtained quantitatively. In the present work, in order to not change the grain boundary composition, ion beam etching was used to observe the grain and grain boundaries instead of the usual thermal etching method.

## 2.5 Transmission electron microscopy (TEM)

The ferroelectric domain structure of the $BiFeO_3$-based ceramics was characterized using a high-resolution transmission electron microscope (JEOL ARM200F) from Japan, with an accelerating voltage of 200 kV. TEM has a higher magnification and resolution than SEM, which can characterize the fine structure of ceramic samples more clearly. In addition, the instrument is equipped with a selected area electron diffraction (SAED) system to obtain diffraction patterns of the ceramic samples.

## 2.6 Piezoresponse force microscopy (PFM)

Piezoresponse force microscopy (PFM) has been widely used as an effective tool for studying the domain structures in ferroelectrics. Fig. 2.2 shows the schematic set-up of PFM. Due to the inverse piezoelectric effect of the material, the sample can vibrate under an applied AC electric field. PFM is used to characterize the high-resolution ferroelectric domain morphology and the domain switching process by testing the piezoelectric vibration of the sample. The used scanning probe microscope was a Seiko SPA400/3800N with an Agilent33120 signal generator and Ametek 7280DSP for the signal processing. For the experiments, the samples need to be thinned below 0.1mm and polished.

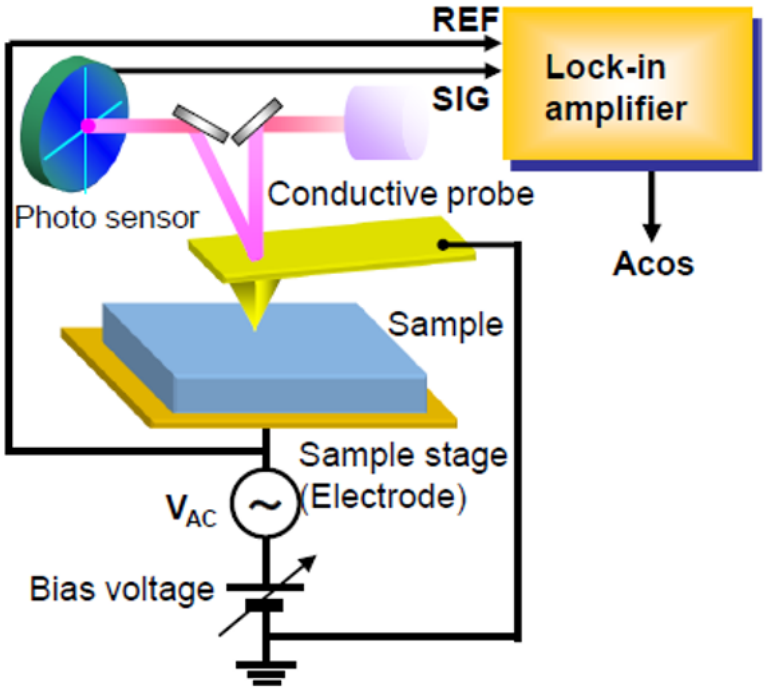


**Figure 2.2** Schematic set-up of piezoelectric force microscopy (PFM).

## 2.7 X-ray photoelectron spectrum (XPS)

XPS is an important tool to study the valence state and content of elements for the materials. The basic principle deals with an X-rays beam irradiating the surface of the material and leading to electrons emission from deep shells. The detection of the X-ray photoelectrons and measuring their energy, we may obtain the binding energy $E_B$ according to the equation below:

$$E_B = h\nu - E_K - \phi \qquad \ldots (2.1)$$

with $E_K$ the energy of the photoelectron, $h\nu$ the energy of the X-ray, and $\phi$ the work function of the sample. In general, the electron binding energy vary with the chemical elements along with the chemical valence states and local environments of the atoms. Therefore, based on the values of the electron binding energy, it is possible to determine the valence state of the elements. In present work, an XPS instrument (ESCAlab250, Thermo Fisher Scientific, America) was used to analyze the valence state of Fe, Bi and O for the $BiFeO_3$-based ceramics.

## 2.8 Mössbauer spectrum

Mössbauer spectroscopy is based on the recoil-free emission and absorption of gamma rays in solids [132]. This technique can provide the information on the hyperfine interactions and the local electronic and magnetic fields at the nucleus. Fig. 2.3 shows a schematic Mössbauer experiment with a single absorption line. $^{57}Fe$ Mössbauer spectrum is sensitive to the chemical valence and surrounding of Fe nuclei which provides information about the electronic density of the nuclei (isomer shift, IS), the electric field gradient (quadrupole splitting, QS) and the magnetic environment (magnetic hyperfine splitting, HF). In present work, the valence state of Fe for the $BiFeO_3$-based ceramics can be obtained according to the mean refined values of hyperfine parameters obtained from Mössbauer spectrum.

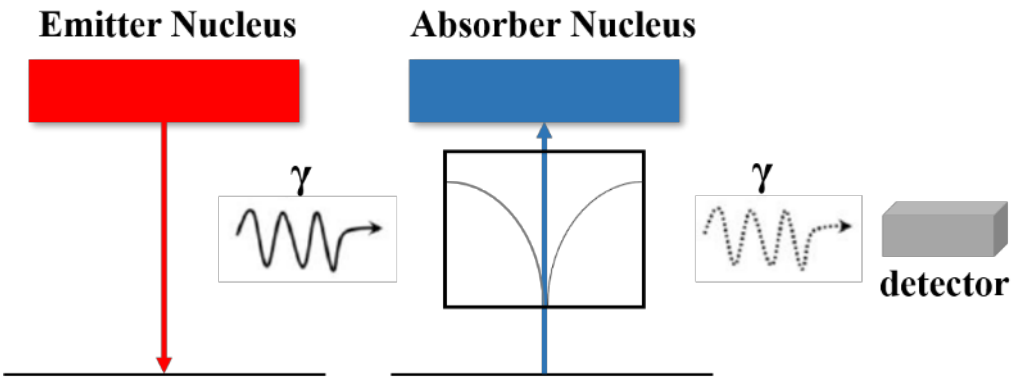


**Figure 2.3** Schematic of Mossbauer spectrum with a single absorption line.

## 2.9 Electrical properties

### 2.9.1 Dielectric properties

The dielectric properties such as the dielectric constant and loss of the $BiFeO_3$-based ceramics were measured by the Agilent 4294A impedance analyzer. The high-temperature dielectric system is based on the impedance analyzer, with a temperature controller and signal acquisition system, as shown in Fig. 2.4. The frequency range is 40 Hz-1 MHz, and the temperature range is room temperature~800 ℃. For the high-temperature dielectric system, the general

frequency is 100 Hz, 1 kHz, 10 kHz, 100 kHz and 1 MHz. The relative dielectric constant of the ceramics is calculated from the measured capacitance, and the formula is as follows:

$$\varepsilon = \frac{Cd}{\varepsilon_0 S} \quad \ldots (2.2)$$

Where $C$ is the capacitance of the test sample (F), $\varepsilon_0$ is the vacuum dielectric constant, which is $8.85\times10^{-12}$ F/m, and $d$ and $S$ are the thickness and the electrode area of the sample (m, $m^2$), respectively.

Novocontrol Broadband Dielectric/Impedance Spectrometer (Broadband Dielectric/Impedance Spectrometer) was also used to accurately characterize the AC impedance spectrum of the ceramics. The temperature range is -150 ℃ to 300 ℃, and the test frequency range is between 0.01 Hz-10 MHz. It can accurately measure the electrical properties such as the dielectric, AC conductivity and AC impedance of the sample, which is very helpful for the analysis of the conduction and the relaxation behaviors of the $BiFeO_3$-based ceramics.

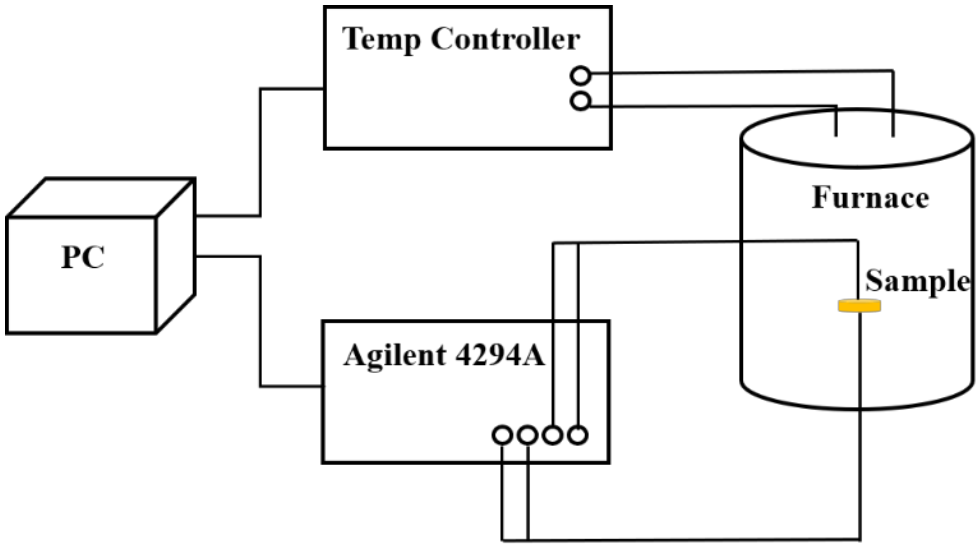


**Figure 2.4** Schematic of high-temperature of dielectric spectrum.

## 2.9.2 Ferroelectric properties

The ferroelectric properties of samples were carried out by using a ferroelectric analyzer ($f$=10 Hz) at room temperature (Model TF 2000E, aixACCT Samples, Germany). The $P$-$E$ hysteresis loops are obtained by the improved Sawyer-Tower

circuit [133], as shown in Fig. 2.5. An AC electric field is applied to the ferroelectric samples, and the value of the horizontal axis in the oscilloscope is proportional to the electric field. At the same time, the polarization of the ferroelectric material is determined by the voltage of the linear capacitor $C_0$ in series. The hysteresis loops of the ceramic sample indicate the ferroelectric properties, including parameters such as the remnant polarization, the maximum polarization and the coercive field. On the other hand, the energy storage density and efficiency can also be obtained through the hysteresis loops. In addition, the temperature controller was used to measure the ferroelectric properties at high temperature. The test temperature range is from room temperature to 200 °C.

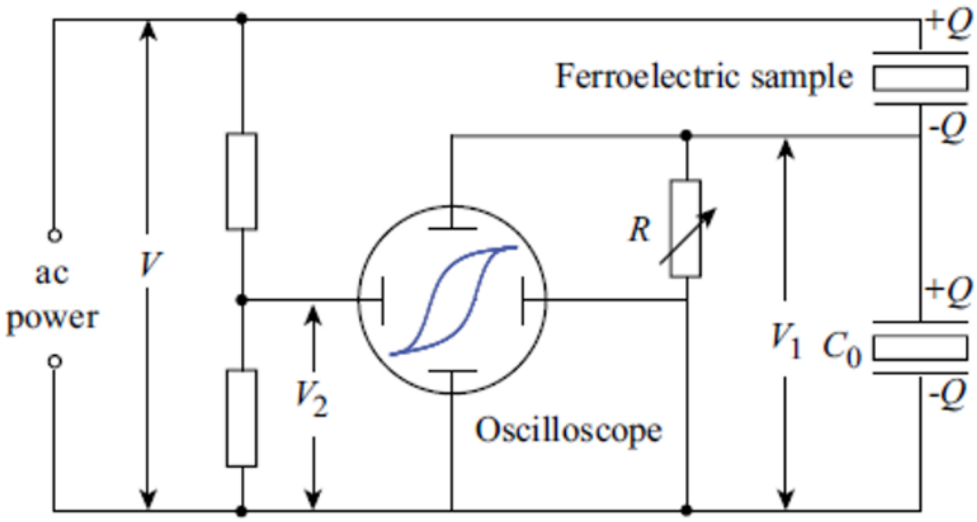


**Figure 2.5** Measurement circuit (Sawyer-Tower) of hysteresis loops [133].

## 2.9.3 Piezoelectric properties

After poling, the piezoelectric coefficient $d_{33}$ of samples was tested by a quasi-static piezoelectric meter (ZJ-3A, Institute of Acoustics, Chinese Academy of Sciences). The schematic representation of the experiment measuring the quasi-static piezoelectric constant $d_{33}$ is shown in Fig. 2.6. An alternating force with a frequency of 110 Hz and a magnitude of 0.25 N is applied along the longitudinal direction of the sample, and the quasi-static $d_{33}$ value of the sample is obtained by comparing the ratio of the charge generated in the longitudinal direction of the sample to the charge

of the standard reference sample.

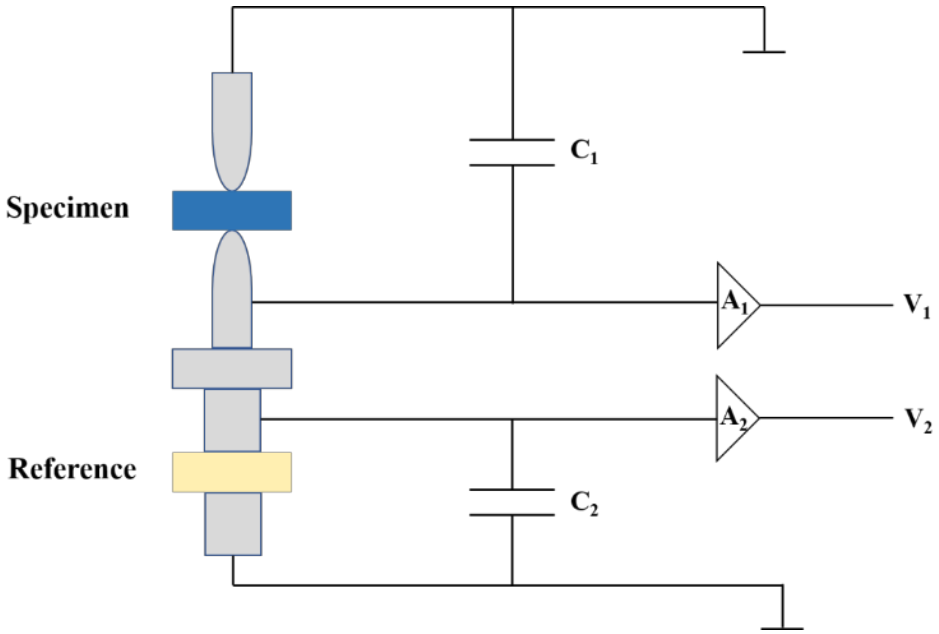


**Figure 2.6** Schematic of measuring quasi-static piezoelectric constant $d_{33}$.

On the other hand, the planar electromechanical coupling coefficient $k_p$ stands for the coupling between the mechanical energy and electrical energy of the piezoelectric ceramics. The value of $k_p$ can be obtained by the resonance-anti-resonance methods. The calculation formula is as follows:

$$k_p = \sqrt{\frac{f_a - f_r}{f_r} \cdot \frac{n^2 - (1-\sigma^2)}{1+\sigma}} \quad \ldots (2.3)$$

Where $f_r$ and $f_a$ denote the resonant frequency and anti-resonance frequency (Hz), respectively; $n$ is the parameter related to the Poisson's ratio; $\sigma$ is the Poisson's ratio of the material, which can be obtained by the following equation:

$$\sigma = \frac{5.332 f_r - 1.867 f_{r1}}{0.6054 f_{r1} - 0.1910 f_r} \quad \ldots (2.4)$$

where $f_{r1}$ is the third resonant frequency.

# Chapter 3 BF-PT based high Curie temperature ceramics

## 3.1 Introduction

Ferroelectric materials with $ABO_3$ structure, such as barium titanate (BT), lead zirconate titanate (PZT), and $Pb(Mg_{1/3}N_{2/3})O_3$-$PbTiO_3$ relaxor ferroelectric, etc., are dominant materials used as capacitors, sensors, actuators and transducers owing to their excellent dielectric and piezoelectric properties [13, 134, 135]. It is commonly known that the working temperature range for piezoelectric devices is limited by their respective Curie temperature ($T_c$), because of the depolarization and phase transition. However, the $T_c$ of these high-performance ferroelectric ceramics is no more than 400 °C, which would restrict their usage range in high-temperature (>200 °C). On the other hand, up to now, the piezoelectric coefficient ($d_{33}$) of high $T_c$ ferroelectric ceramics such as tungsten bronze and bismuth layer structure is normally lower than 100 pC/N [24, 25]. Thus, the requirement for high $T_c$ ferroelectric ceramics with a high piezoelectric coefficient remains an important research task for high-temperature piezoelectric actuators and sensors.

Bismuth ferrite ($BiFeO_3$, abbreviated as BFO) is an attractive lead-free ferroelectric material owing to the electron configuration of $Bi^{3+}$ being similar to $Pb^{2+}$ (lone $6s^2$ electron configuration). More precisely, BFO ceramics with distorted perovskite structure (space group $R3c$) exhibit a large ferroelectric spontaneous polarization (~100 μC/cm$^2$) and a high Curie temperature (~830 °C) [46]. Meanwhile, BFO ceramics feature a semiconducting nature with a lower bandgap (2.7 eV) at room temperature, and the pure BFO ceramic is difficult to prepare due to the formation of secondary phases such as $Bi_2Fe_4O_9$ and $Bi_{25}FeO_{40}$ during the sintering process [136]. The complex perovskite $(BiFeO_3)_x$-$(PbTiO_3)_{1-x}$ (BF-PT) compounds is characterized by a high $T_c$ ~630 °C for the composition with $0.27<x<0.31$, which recently

considered as the most promising high $T_c$ ferroelectric solid solutions [67, 137]. However, two main factors restrict their efficient polarization, leading to the low $d_{33}$ values. This behavior can be related to BF-PT system in the vicinity of the MPB where a large tetragonality occurs, enhancing the internal compatibility stresses which suppress the domain switching [137]. The other reason is that high leakage current and dielectric loss make it difficult to be proper electrical poled for ceramics. Thus, there is a growing number of reports devoted to $d_{33}$ enhancement by site engineering. However, the general principles for its rational use have not yet been well achieved.

In terms of the BF-PT based ceramics, $Pb_3O_4$ powder was rarely selected as the starting materials for the preparation of ceramics. Meanwhile, the effects of different lead raw materials on ceramic properties have not yet been realized. Therefore, we chosen both PbO and $Pb_3O_4$ powder as the lead raw materials in the preparation of BF-PT based ceramics. On the one hand, our aim is to investigate the effects on the electrical properties of the ceramics with different lead raw materials, on the other hand, to research the mechanism of high leakage current in BF-PT based ceramics. It turned out that the comprehensive electrical properties of BF-PT(PbO) sample were better than that of BF-PT($Pb_3O_4$) sample, which was quite different from other reports of lead-based piezoelectric ceramics. A key result from this study was the finding that in terms of the BF-PT based ceramics, the ceramics using $Pb_3O_4$ as raw material were more likely to induce the fluctuation of the Fe valence and the oxygen deficiency, resulting in an increase in leakage current.

On the basis of the proper preparation process, we propose to design a structure with a weak tetragonality that enhances the domain switching by introducing $Ba^{2+}$ at A-site and $Sn^{4+}$ at B-site in BF-PT solutions. From the point of electron configuration aspects, the 6*s* orbital of $Ba^{2+}$ has no lone pair electrons, meanwhile, $Sn^{4+}$ has no "$3d^0$" electron configuration and hence it is not supposed to be a ferroelectric-active ion. These A/B-sites substitution ions would decrease the covalent character of A-O and B-O bonds and weaken the long-pair activity, greatly contributing to the reduction of the structure tetragonality. Besides, based on ionic radius considerations, the large ionic radius of $Ba^{2+}$ (CN=12, $r_{Ba^{2+}}$=1.61 Å) at A-sites compared to that of $Bi^{3+}$

(CN=12, $r_{Bi}^{3+}$=1.36 Å), could fill the empty space (oxygen cuboctahedra) fully, suppressing the tilt of oxygen octahedra. A relevant strategy concerning the formation of the morphotropic phase boundary was also taken into account in the ternary system. With the introduction of $Ba(Sn_{0.2}Ti_{0.8})O_3$ (cubic phase) [138] to the $BiFeO_3$ (rhombohedral phase) and $PbTiO_3$ (tetragonal phase), the complex phase coexistence regions are expected to be obtained in the new system. Here, a novel ferroelectric $BiFeO_3$-$BaTiO_3$-$Ba(Sn_{0.2}Ti_{0.8})O_3$ (abbreviated as BF-PT-BST) solid solution was fabricated by a conventional solid-state reaction method. A high piezoelectric coefficient with a high $T_c$ was achieved simultaneously in this new system.

## 3.2 Experimental

In the first subsection, $Pb_3O_4$ and PbO as two kinds of lead raw materials have been used for the preparation of $0.55BiFeO_3$-$0.25PbTiO_3$-$0.2Ba(Zr_{1/4}Ti_{3/4})O_3$ ceramics (abbreviation as 'BF-PT(PbO)' and 'BF-PT($Pb_3O_4$)'). In addition, on the basis of proper preparation process, modified $BiFeO_3$-based ceramics were fabricated based on the chemical formula of (0.76-x) $BiFeO_3$-$0.24PbTiO_3$-x$Ba(Sn_{0.2}Ti_{0.8})O_3$ (x=0.1, 0.13, 0.16, 0.18, 0.20, 0.22, 0.24, 0.26, 0.28, 0.30) using a conventional solid-state reaction method. The detailed preparation process is shown in Chapter 2 of this thesis.

## 3.3 Effects on the electrical properties of BF-PT based ceramics with different lead raw materials

### 3.3.1 Phase and microstructure

Fig. 3.1 shows the X-ray diffraction patterns and SEM images of ceramic samples. The XRD patterns were taken from as-ground powders and the SEM images were taken from fresh fracture surfaces. Both samples show pure perovskite lattice structures. The XRD patterns indicate that there is no difference in phase

structure for both samples. In terms of microtopography, the grain sizes can be greatly influenced by different lead raw materials. The grains size in the BF-PT(PbO) sample is in the range of 10 to 15 μm, which is larger than the grain size of BF-PT($Pb_3O_4$) sample (about 5 μm). A possible explanation for the reduction in grain size is that the second phase accumulated at grain boundaries and could inhibit grain growth in the BF-PT($Pb_3O_4$) system. Similar phenomenon was also observed in other ceramics [139]. It will be further discussed below.

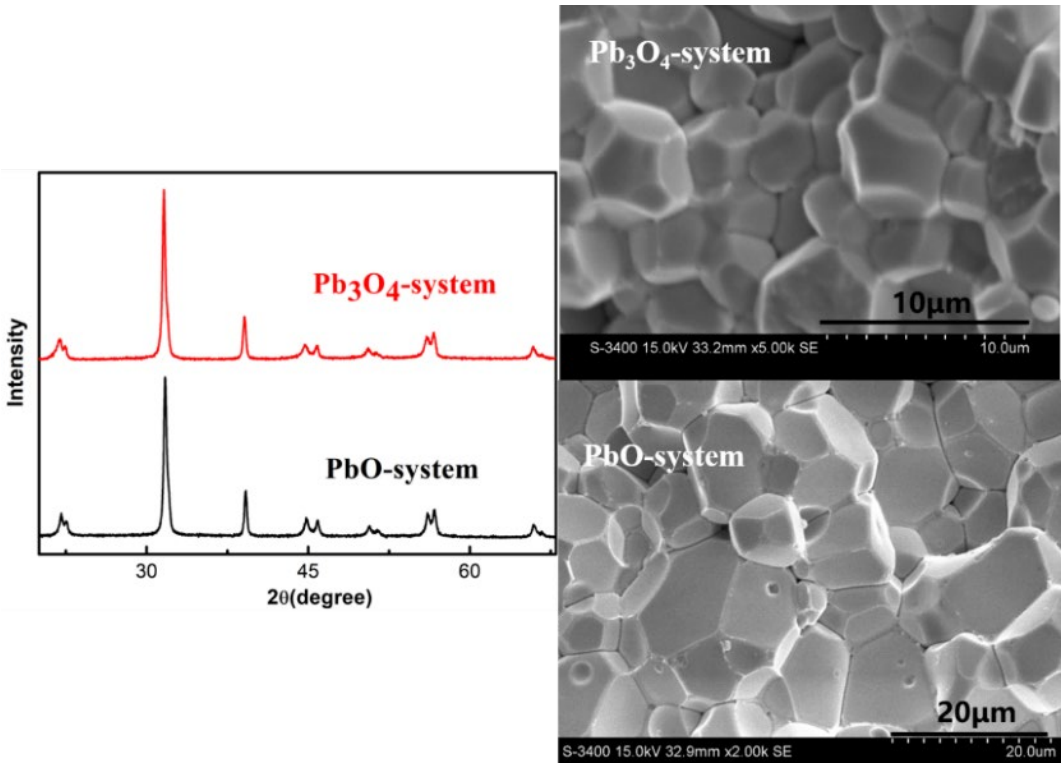


**Figure 3.1** The XRD patterns and the SEM images of the ceramics with different lead raw materials.

## 3.3.2 Dielectric and ferroelectric properties

Fig. 3.2 shows the frequency dependence of the dielectric loss measured at 25 ℃ for ceramics with different lead raw materials. It was found that the tendency of the dielectric loss is similar as a function of frequency for both samples. As illustrated in Fig.3.2, as the frequency increases, a relaxation peak occurs and corresponds to the dominant effect of the polarization loss. As the frequency continues to increase, the loss caused by both mechanisms decreases with increasing the frequency. The

dielectric loss can be described by the following formula:

$$\tan\delta = \tan\delta_p + \tan\delta_G = \left(\frac{(\varepsilon_S-\varepsilon_\infty)\omega\tau}{\varepsilon_S+\varepsilon_\infty\omega^2\tau^2}\right) + \frac{\gamma}{\varepsilon_0\omega\varepsilon_r'}\frac{1}{\varepsilon_\infty+(\varepsilon_S-\varepsilon_\infty)/(1+\omega^2\tau^2)} \quad \ldots (3.1)$$

Where tan$\delta$ represents the dielectric loss, tan$\delta_P$ and tan$\delta_G$ represent the polarization loss and the leakage loss. It should be noted that the dielectric loss is almost attributed to the leakage loss at low frequencies ($\omega\tau \leq 1$). In addition, it can be seen that the relaxation peak of BF-PT($Pb_3O_4$) sample moves towards a high frequency compared with that of BF-PT(PbO) sample, indicating that the dielectric loss caused by leakage current is important in BF-PT($Pb_3O_4$) sample.

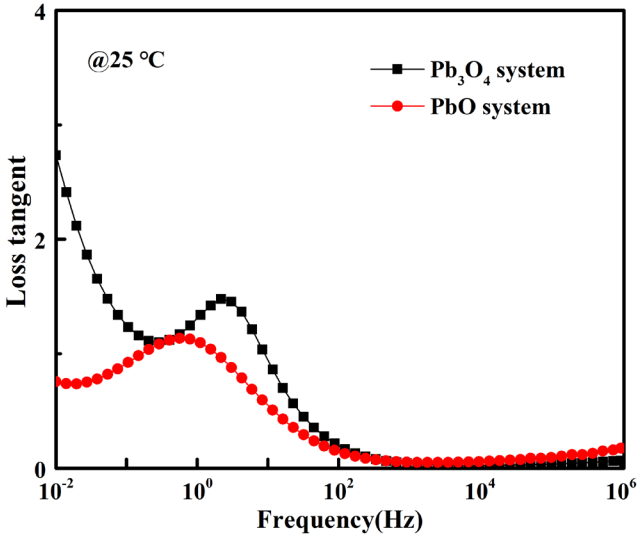


**Figure 3.2** The frequency dependence of the dielectric loss measured at 25°C for ceramics with different lead raw materials.

Fig. 3.3 shows the temperature dependence of $\varepsilon_r$ and tan$\delta$ for the ceramics with different lead raw materials (measured at 100 kHz). There is almost no difference in the phase transition temperature for these two samples. However, it should be pointed out that the dielectric loss of the BF-PT(PbO) sample has a minor change under the phase transition temperature. On the contrary, the BF-PT($Pb_3O_4$) sample has poor temperature stability and the high dielectric loss above 200 °C because of the high conductivity in the BF-PT($Pb_3O_4$) sample, which is consistent with the results obtained from Fig 3.2. In addition, the dielectric constant of the BF-PT(PbO) sample is higher than that of the BF-PT($Pb_3O_4$) sample in the test temperature range, especially at the phase transition point. It must be mentioned that the reduction of

dielectric constant is in agreement with the reduction in the grain sizes which affect the dielectric properties in ceramics as it was intensively investigated [140, 141]. According to the dielectric mixing rules and brick-wall model, the reduction of grain size leads to a change in the number of grain boundaries, resulting in a decreasing dielectric constant.

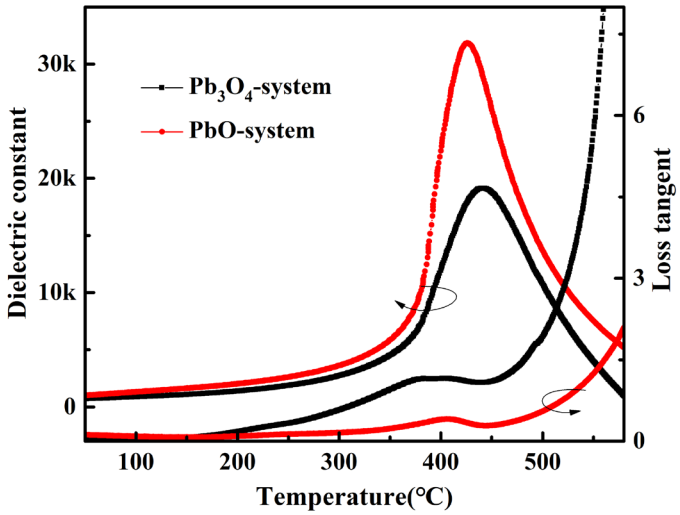


**Figure 3.3** The temperature dependencies of $\varepsilon_r$ and tanδ for the ceramics with different lead raw materials.

Fig. 3.4 presents the *P-E* hysteresis loops measured at 10 Hz at room temperature for ceramics with different lead raw materials. There is an obvious difference of ferroelectric properties in the two samples. The BF-PT($Pb_3O_4$) sample exhibits a round hysteresis loop, which indicates that the high leakage current is considered to be the dominant factor for the *P-E* relationship as it was also observed in other ferroelectric materials [133, 142]. However, for the BF-PT(PbO) sample, the effect of leakage current is small and the real hysteresis loop is more indicative of the domain switching of the ferroelectric materials. It was shown that the leakage current of the BF-PT(PbO) sample is lower than that of BF-PT($Pb_3O_4$) sample. It should be noted also that the polarization of ceramics by the traditional solid-state synthesis method is usually small compared to thin films, single crystals, or according to the results from theoretical calculations. Therefore, although first-principles calculations indicated that the huge spontaneous polarization in

$BiFeO_3$, the spontaneous polarization of BF-PT(PbO) sample is only 20 μC/cm$^2$.

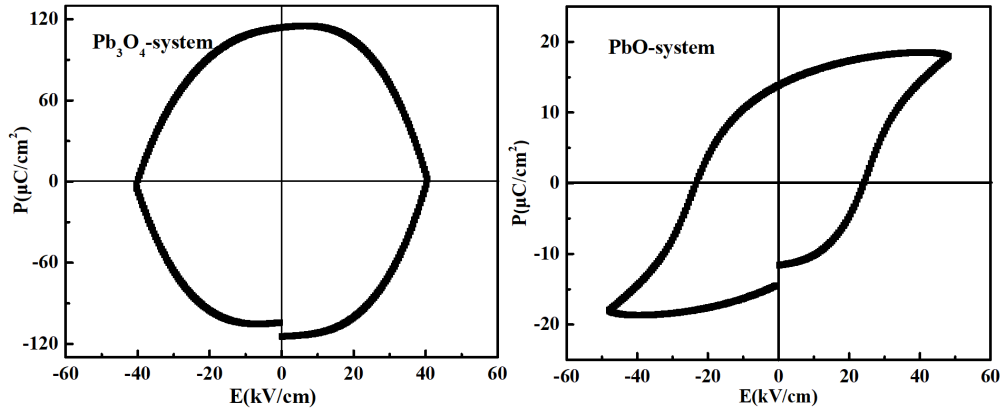


**Figure 3.4** The electric field dependence of the electrical polarization for ceramics with different lead raw materials.

## 3.3.3 EDS analysis

Why are there such big differences in ferroelectric and dielectric properties for ceramic samples with different lead raw materials? In order to verify the composition of grains and grain boundaries of ceramics, two samples were characterized using SEM equipped with energy dispersive X-ray spectroscopy (EDS). In this experiment, in order not to change the grain boundary element composition, ion beam etching was used to observe the grain and grain boundaries instead of the usual thermal etching method. The ion beam etching surface images and EDS analysis results of ceramics with different lead raw materials are shown in Fig. 3.5. We can see that the backscattered electron SEM image of the BF-PT($Pb_3O_4$) sample has a clear difference in the contrast between grain and grain boundaries, in which the white contrast is shown as grain boundaries. However, the difference in contrast between grains and grain boundaries of the BF-PT(PbO) sample is not clear. A line scan elemental analysis along the grain and grain boundaries in two samples was carried out. It can be seen that there is basically no difference in the elemental composition of grains and grain boundaries for the BF-PT(PbO) sample. Nevertheless, for the BF-PT($Pb_3O_4$) sample, the content of Bi increases obviously at the grain boundary, while other elements do not change, indicating that there is a Bi-rich grain boundary phase, corresponding to the white contrast phase of the

backscattered electron SEM image.

To further explore elemental composition, we then select the grain and grain boundary respectively for point element analysis (Fig. 3.6). As shown in Table 3.1, all elements can be observed in the ceramics, and the measured atomic percentage in grain is approximately consistent with the stoichiometric ratio. On the contrary, the measured percentage of Bi in grain boundary is significantly higher than the theoretical value. It is confirmed that the second phase deviated from perovskite phase exists at the grain boundary. However, this Bi-rich grain boundary phase is not observed in the XRD patterns, possibly due to the low content of the second phase.

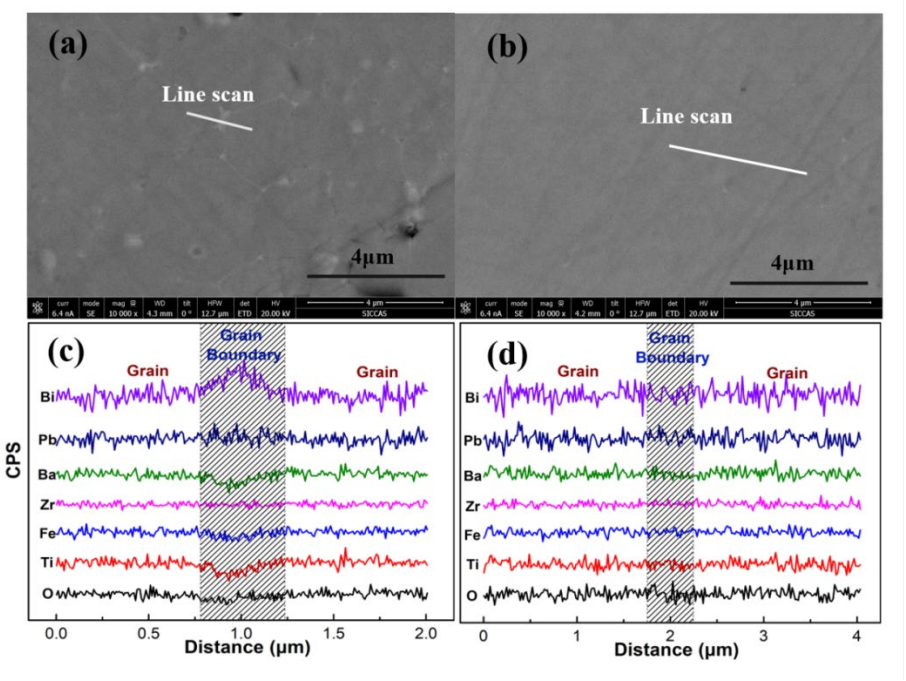


**Figure 3.5** The ion beam etching surface images and EDS analysis of ceramics with different lead raw materials.

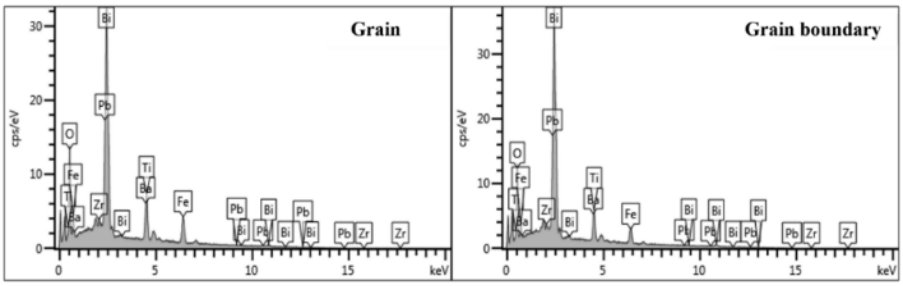


**Figure 3.6** The point element EDS analysis for the grain and the grain boundary of BF-PT($Pb_3O_4$) ceramics.

**Table 3.1** The intended composition, the actual compositions as determined by EDX.

| Element | Cal. Atomic% | Prac. Atomic% (Grain) | Prac. Atomic% (Grain boundary) |
|---|---|---|---|
| O | 60.00 | 57.60 | 58.03 |
| Ti | 8.00 | 8.17 | 7.13 |
| Fe | 11.00 | 11.80 | 8.98 |
| Zr | 1.00 | 1.17 | 0.92 |
| Ba | 4.00 | 3.87 | 3.61 |
| Pb | 5.00 | 5.67 | 5.33 |
| Bi | 11.00 | 11.71 | 16.01 |

## 3.3.4 XPS analysis

It is generally accepted that the fluctuation of the chemical valence state and the oxygen vacancy are important factors for leakage current and electrical properties in the $BiFeO_3$ based ferroelectric ceramics. XPS analysis for Bi 4f, O 1s and Fe 2p core level binding energy spectra of ceramics with different lead raw materials are shown in Fig. 3.7 (a)-(c), and the fitting results were presented in Table 3.2. Fig. 3.7 (a) shows the core level binding energy spectra of Bi 4f. For both samples, two strong peaks at ~158 and ~163 eV in the XPS spectra correspond to Bi $4f_{7/2}$ and Bi $4f_{5/2}$ respectively, which is a characteristic of $Bi^{3+}$ [143]. Most surprisingly, two weak peaks near the characteristic peak of $Bi^{3+}$ are found only in the BF-PT(PbO) sample, which have a smaller binding energy of $Bi^{3+}$, representing the existence of bismuth ion with a lower valence state. This result indicates that Bi ions were reduced partially during the sintering process. Furthermore, it can be seen from the table that the content of this peak is very low (~2 %). A possible explanation is that the bismuth ions with lower valence state are related to the Bi-rich grain boundary phase observed in the backscattered electron SEM image. Fig. 3.7(b) shows the core level binding energy spectra of O 1s. It can be seen that all samples have an asymmetric peak, which can be divided into two peaks, indicating that the oxygen vacancy ($V_{\ddot{O}}$) exists in the samples besides the intrinsic $O^{2-}$ ion. The lower binding energy peak (at ~529 eV) corresponds to the intrinsic $O^{2-}$ ion in the perovskite ceramic, while the higher binding energy peak (at ~ 531 ev) belongs to the oxygen vacancy [143]. The ratio of

the fitted peak areas is shown in Table 3.2, the concentration ratios of $O^{2-}$ and oxygen vacancy in different samples are 42.10:57.90 and 55.81:44.19, respectively, which implies that the content of oxygen vacancy in the BF-PT($Pb_3O_4$) sample is higher than that in the BF-PT(PbO) sample. In addition, the core level binding energy spectra of Fe $2p_{3/2}$ is displayed in Fig. 3.7(c). It can be observed that the coexistence of $Fe^{3+}$ and $Fe^{2+}$ ions in both samples. The peak at ~709 eV is regarded as $Fe^{2+}$, while the peak at ~711 eV is regarded as $Fe^{3+}$. According to the quantitative data in Table 3.2, the concentration ratios of $Fe^{2+}$ in the ceramics with $Pb_3O_4$ and PbO source are 56.83 % and 21.13 %, respectively.

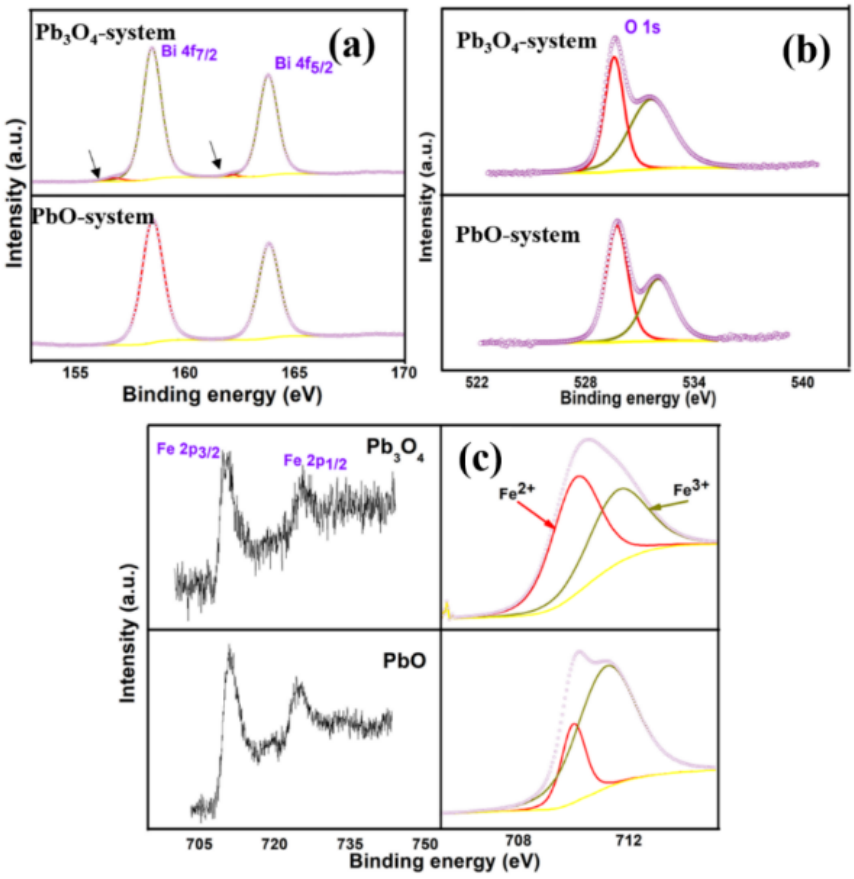


**Figure 3.7** XPS analysis for Bi 4f, O 1s and Fe 2p core level binding energy spectra of ceramics with different lead raw materials.

**Table 3.2** Fitted peaks of O 1s, Fe 2p and Bi 4f.

| O 1s | Peaks | Atomic % | $Fe\ 2p_{3/2}$ | Peaks | Atomic % | Bi 4f | Peaks | Atomic % |
|---|---|---|---|---|---|---|---|---|
| $Pb_3O_4$ | 529.27 | 42.1 | $Pb_3O_4$ | 709.87 | 56.83 | | 158.45 | 55.45 |
| sample | 531.17 | 57.9 | sample | 711.39 | 43.17 | $Pb_3O_4$ | 163.76 | 42.76 |
| PbO | 529.64 | 55.81 | PbO | 709.85 | 21.13 | sample | 156.76 | 1.23 |
| sample | 531.93 | 44.19 | sample | 711.05 | 78.87 | | 162.14 | 0.56 |
| | | | | | | PbO | 158.52 | 56.86 |
| | | | | | | sample | 163.83 | 43.14 |

For traditional lead-based piezoelectric ceramics, such as $Pb(Zr, Ti)O_3$ (PZT), $Pb(Mg_{1/3}Nb_{2/3})O_3$ (PMN), and $(Pb, La)(Zr, Ti)O_3$ (PLZT) etc., $Pb_3O_4$ and PbO powder are the main two kinds of lead raw materials. It can be found that different lead raw materials have a minor effect on the properties of lead-based piezoelectric ceramics, and the choice of lead raw materials has not been considered. Lu et al. [144]. systematically investigated the effects on electric properties of PMN-PT ceramics with different starting materials ($Pb_3O_4$ and PbO), demonstrating that the dielectric properties of the PMN($Pb_3O_4$) sample were higher than that of the PMN(PbO) sample, owing to the pyrochlore phase was suppressed effectively in PMN($Pb_3O_4$) sample. The similar results were also observed in PLZT ceramics [145]. These were attributed to the fact that the chemical activity of $Pb_3O_4$ powder is higher than that of common PbO powder. It is commonly known that the $Pb_3O_4$ will be decomposed to PbO at 560 ℃, as shown in the following chemical formula [146]:

$$Pb_3O_4 \rightarrow 3PbO+1/2O_2 \quad \ldots(3.2)$$

Where the newly generated PbO powder with the fresh surface and small particle size would be beneficial to the sintering behavior and the formation of pure perovskite phase. In terms of the BF-PT based ceramics, the high chemical activity of $Pb_3O_4$ facilitates the formation of Bi-rich second phase at the grain boundary for BF-PT($Pb_3O_4$) sample, which leads to the smaller grain size compared with

BF-PT(PbO) sample. Meanwhile, the concentration of the oxygen vacancy and $Fe^{2+}$ ion in BF-PT($Pb_3O_4$) sample is significantly higher than that in BF-PT(PbO) sample, which exactly confirms the cause of high conductivity in BF-PT($Pb_3O_4$) sample.

# 3.4 Structure and properties of (0.76-x)BF-0.24PT-xBST ceramics

## 3.4.1 Phase and microstructure

Fig. 3.8 shows the X-ray diffraction patterns of (0.76-x)BF-0.24PT-xBST powders sintered at an optimal temperature. All the ceramic samples exhibit pure perovskite structure with no trace of the pyrochlore phase. Detailed XRD profiles of (200) diffraction lines in the 2θ range of 44°-46° are also shown in Fig. 3.8. Only one peak can be observed in the composition of x=0.1, indicating the involvement of a rhombohedral (R) phase structure. With increasing x, it can be refined with three peaks, corresponding to $(200)_R/(200)_{PC}$, $(200)_T$ and $(002)_T$, respectively. As a result, the samples with the composition range $0.13<x<0.28$, exhibit a morphotropic phase boundary (MPB) structure. As x=0.3, there are no detectable splitting peaks from the XRD pattern, indicating its high symmetrical structure (cubic phase). It is known that a cubic centrosymmetric crystal would exhibit the paraelectric phase without ferroelectricity. Nevertheless, the ferroelectric property can be obtained for x=0.3 from the following analysis outlined below. Indeed, the composition of x=0.3 exhibits a pseudo-cubic (PC) structure, instead of the R structure characterized by a split in the (111) peak. This result is consistent with previous reports on the pseudo-cubic perovskite ceramics [121, 122, 147].

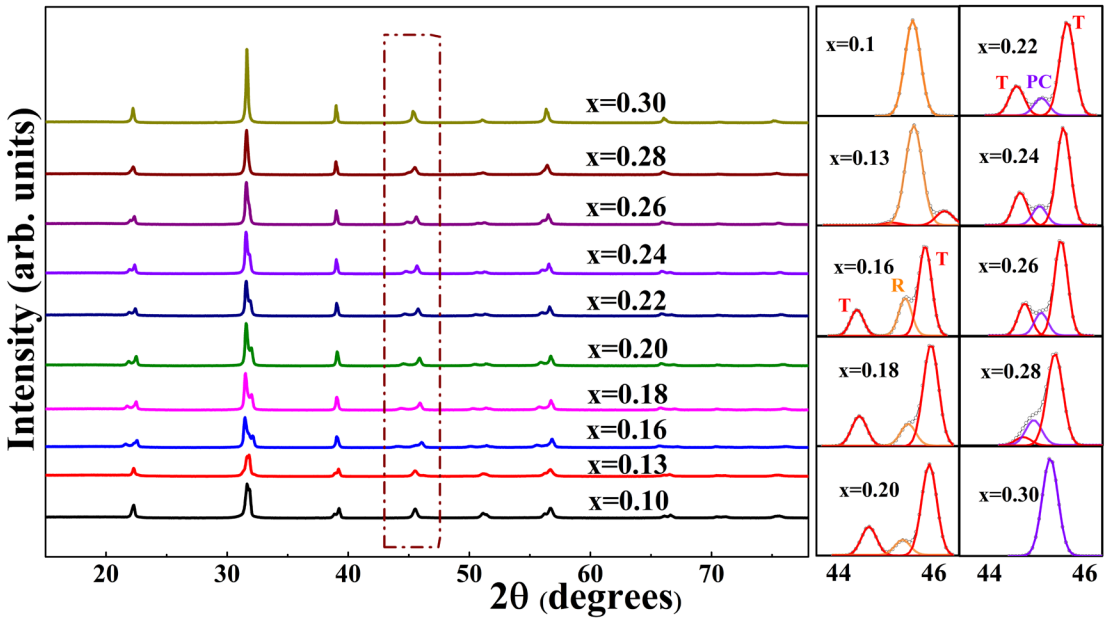


**Figure 3.8** Powder XRD patterns of (0.76-x)BF–0.24PT–xBST ceramics (x=0.10-0.30), and locally magnified (200) diffraction peaks.

As mentioned earlier, there are the MPB structures in the composition of 0.13<x<0.28. Accordingly, the *R3c*、*P4mm* and *Pm-3m* space groups relevant to the $BiFeO_3$-$PbTiO_3$ compounds were considered in the Rietveld refinements for BF-PT-BST samples with the best refinement results shown in Fig. 3.9. In the present work, the composition range 0.13<x<0.20 leads to the coexistence of R and T phases abbreviated as $MPB_1$, while the coexistence of T and PC phases abbreviated as $MPB_2$ is obtained with the composition range 0.22<x<0.28. According to the results from Rietveld refinements, the fraction of each phase as well as the lattice parameters $a_T$($b_T$), $c_T$ and tetragonality ($c_T/a_T$) are shown in Fig. 3.10(a) and (b), respectively. With increasing the content of BST, the evolution of the structure gradually changes from pure R phase to R+T phase, then to T+PC phase and finally to PC phase. In addition, an obvious trend from Fig. 3.10(b) is manifested by the decrease of the tetragonality with increasing the content of BST. The replacement of the large radius $Ba^{2+}$ at A-site along with the non-ferroelectric-active $Sn^{4+}$ at B-site, greatly weakens the covalent character of A-O and B-O bonds leading to a decrease of parameter *c* and an increase of parameter *a* [93].

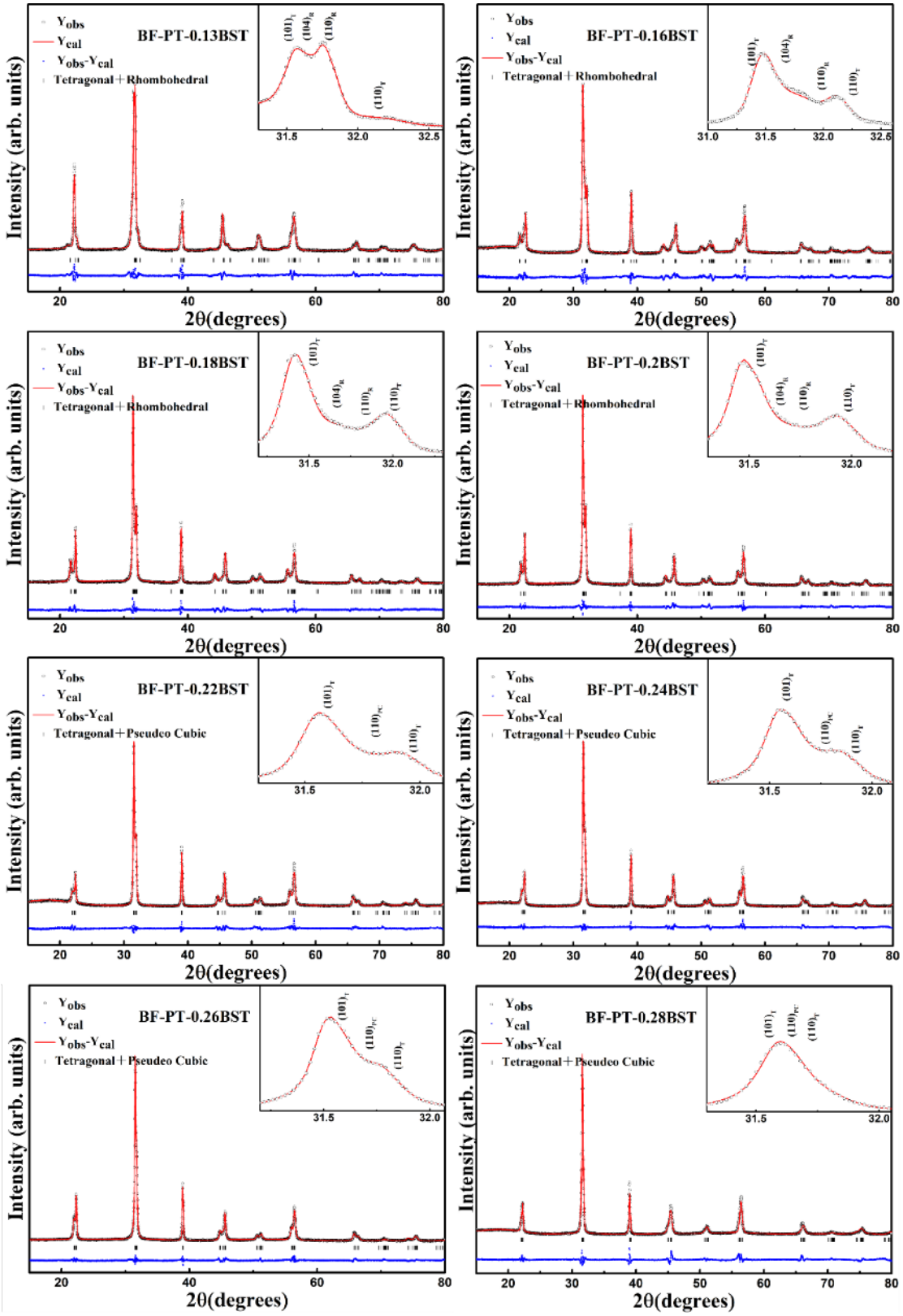


**Figure 3.9** XRD patterns with Rietveld refinement of (0.76-x)BF-0.24PT-xBST ceramics

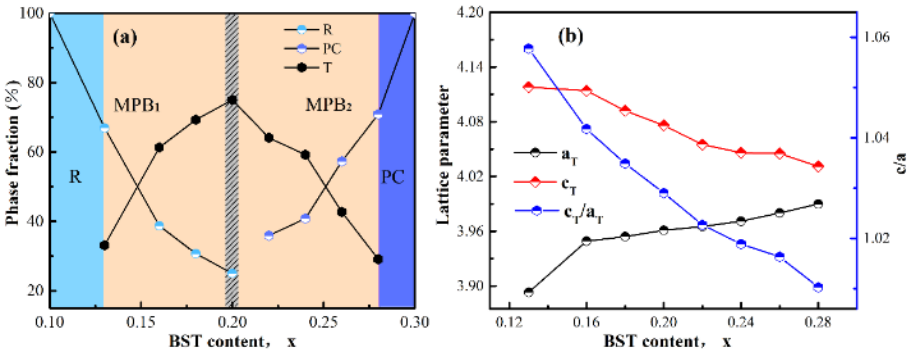


**Figure 3.10** Phase fraction and lattice parameters of (0.76-x)BF-0.24PT-xBST ceramics.

Fig 3.11 shows the SEM images of the fresh fracture surfaces for BF-0.24PT-xBST ceramics (x=0.1, 0.18, 0.24, 0.30). It can be seen that all samples exhibit a dense microstructure with a limited porosity. The typical grain size of about 3-5 μm remains unchanged with the variations of the composition.

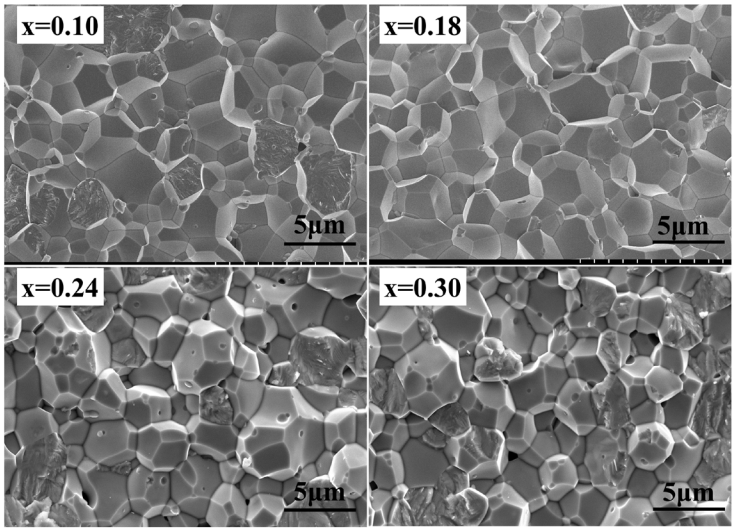


**Figure 3.11** SEM images of the fresh fracture surfaces of (0.76-x)BF-0.24PT-xBST ceramics (x=0.1, 0.18, 0.24, 0.30).

The (110), (111) and (200) diffraction peaks for (0.76-x)BF-0.24PT-xBST (x=0.13, 0.20, 0.26) ceramics as a function of temperature are shown in Fig. 3.12. Firstly, as can be seen from Fig. 3.12(a), the (111) peaks of all samples gradually move toward a lower angle with increasing temperature, indicating an increase in the unit cell volume. This result is related to the lattice expansion at the high temperature. The splitting of (110) and (200) peaks gradually change to the single peaks with the

increase of temperature, indicating the evolution from asymmetric to symmetric structure. In order to observe the phase transition process more clearly, Fig. 3.12(b) shows the Color map of (200) peaks for the ceramics. It can be clearly observed that the phase transition temperature of the BF-PT-0.13BST, BF-PT-0.2BST and BF-PT-0.26BST ceramics are about 500 ℃, 450 ℃ and 400 ℃, respectively. This result shows that the ceramics have a high Curie temperature. In the following, the dielectric properties will be studied to further confirm the Curie temperature of the ceramic samples.

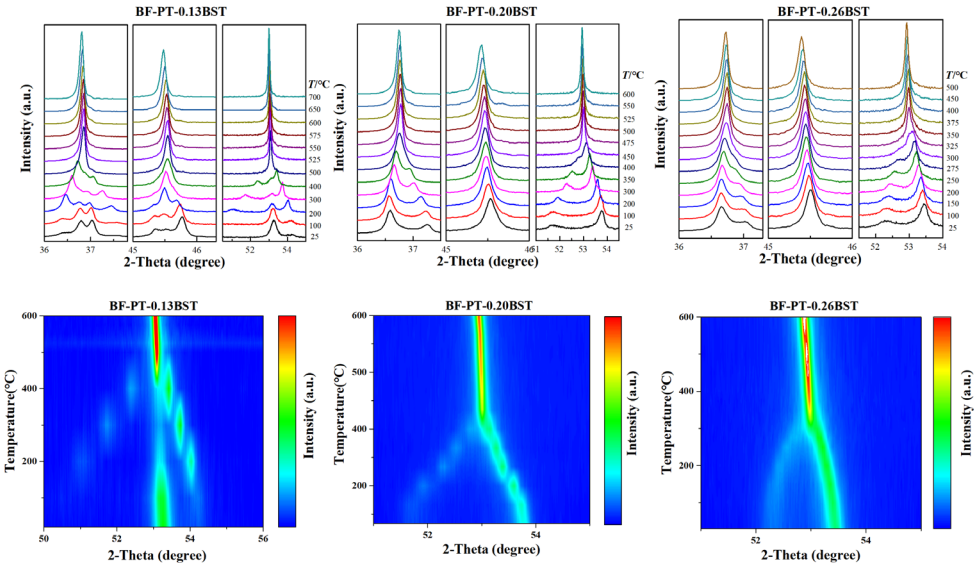


**Figure 3.12** (a) Temperature dependence of XRD patterns of (0.76-x)BF-0.24PT-xBST (x=0.13, 0.20, 0.26) ceramics; (b) Color map.

## 3.4.2 Dielectric properties

The temperature dependence of dielectric constant and loss tangent of (0.76-x)BF-0.24PT-xBST ceramics measured at 100kHz are shown in Fig. 3.13(a) and (b). Obviously, the substitution of BST into the BF-PT solid solution remarkably affects the dielectric properties. It can be observed that the temperature at the dielectric constant maxima ($T_m$) decreases monotonously with the increase of the BST content. It decreased from 557℃ at x=0.10 to 328 ℃ at x=0.30. The drop in ferro-to-paraelectric transition temperature is due to the weakly structural distortion for the perovskite ferroelectric ceramics [148]. As shown in Fig. 3.13(b), the

compositions with high $BiFeO_3$ content show pronounced dielectric loss peaks at high temperature. The drastic increase of the loss tangent at high temperature results from the enhanced contribution from thermally activated conductivity. In addition, with increasing the BST content, the dielectric constant maxima ($\varepsilon_m$) rapidly decreased accompanied by a drastic broadening of the dielectric peak. Fig. 3.14 presents the temperature and frequency dependence of dielectric constant of all ceramic samples. The ceramic samples with high BST content show frequency dispersion and diffuse phase transition behavior at $T_m$. It is generally accepted that the diffuse characteristics of the ferroelectric-paraelectric phase transition can be described by a modified Curie-Weiss law $1/\varepsilon-1/\varepsilon_m = (T-T_m)^\gamma/C$. The plots of fitting data for all ceramics are shown in Fig. 3.15. The diffusion exponent ($\gamma$) shown in Fig. 3.13(b), increases from 1.28 to 1.82 with increasing the BST content from 0.1 to 0.3. The admixture of $(Sn_{0.2}Ti_{0.8})^{4+}$ ions in BF-PT would lead to the disordered distribution of different ions ($Sn^{4+}$, $Ti^{4+}$, $Fe^{3+}$) on the equivalent lattice sites, which may contribute to the relaxor-like behavior [149]. In general, perovskite ferroelectrics with pseudo-cubic structures are accompanied by a ferroelectric order at the nanoscale and exhibit the relaxor-like dielectric behaviors [147].

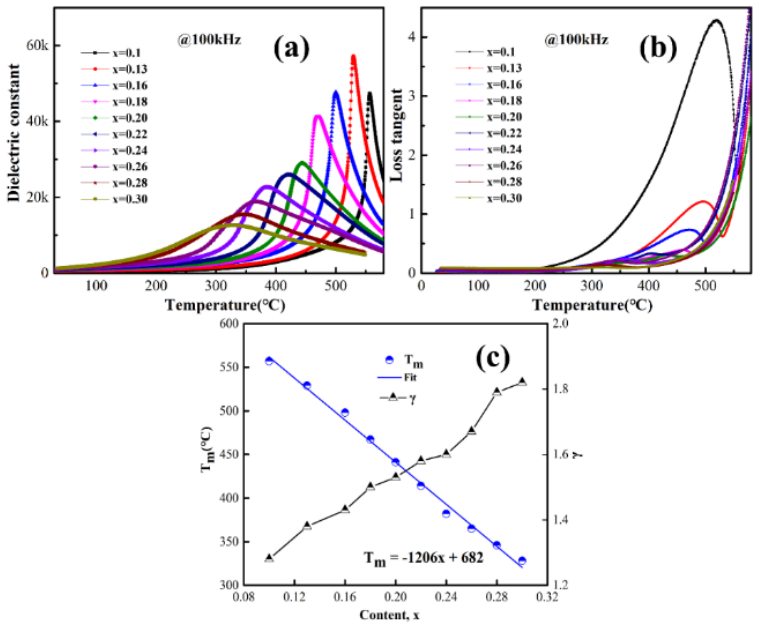


**Figure 3.13** (a) Dielectric constant; (b) loss tangent as a function of temperature for (0.76-x)BF-0.24PT-xBST ceramics; and (c) $T_m$ and $\gamma$ values as a function of x.

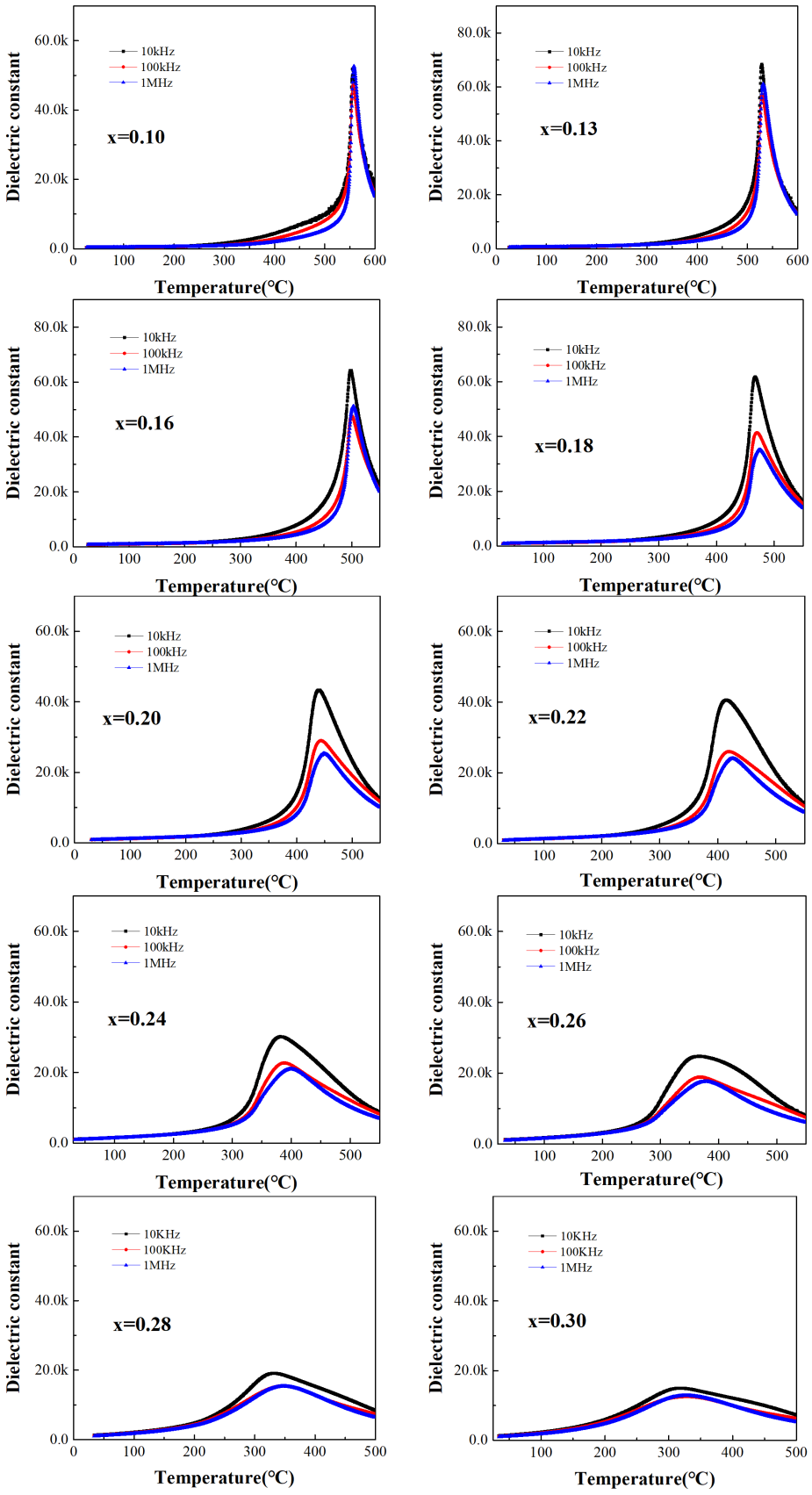


**Figure 3.14** Dielectric constant $\varepsilon$ as a function of temperature with different frequency for (0.76-x)BF-0.24PT-xBST ceramics.

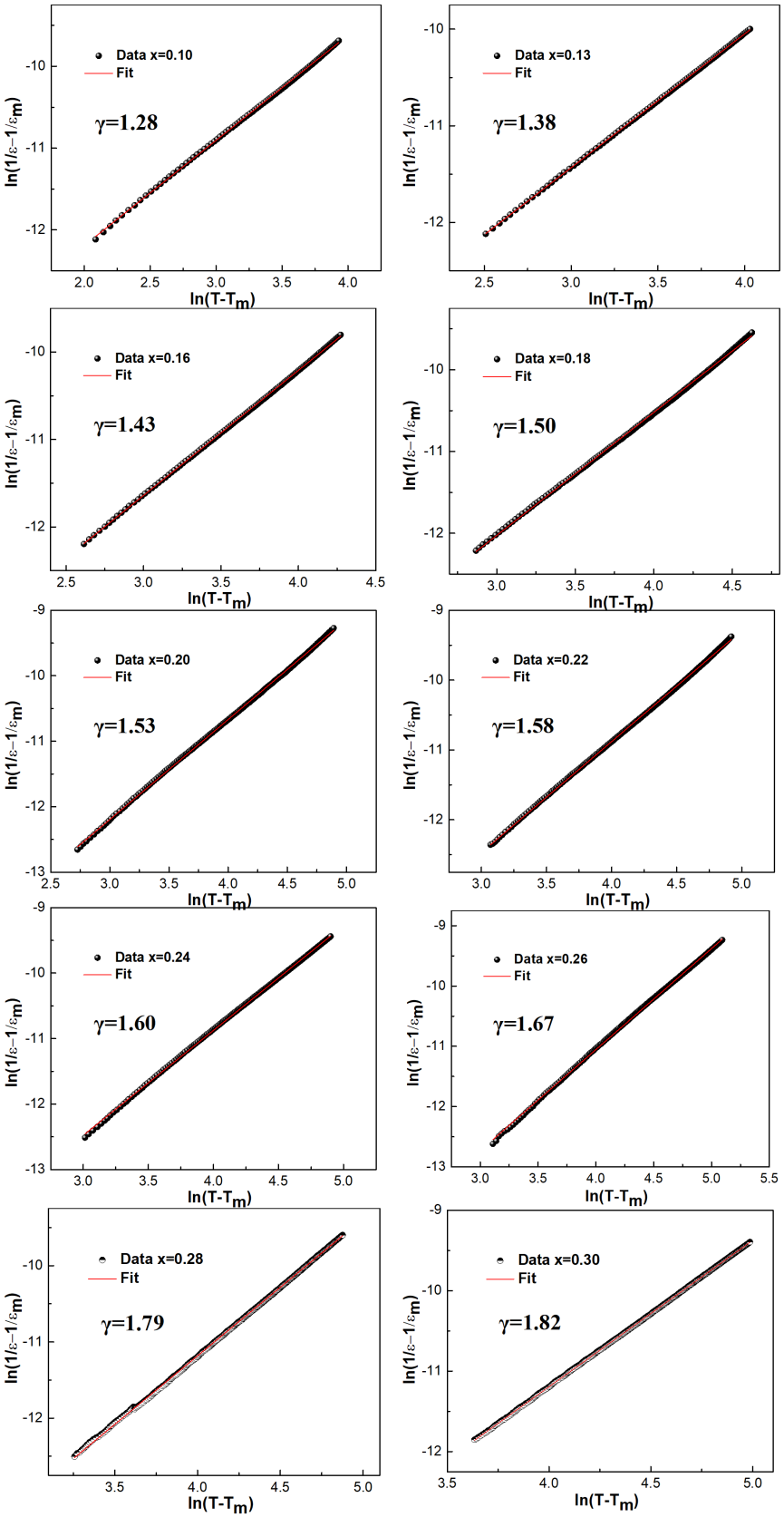


**Figure 3.15** Plots of $\ln(1/\varepsilon\text{-}1/\varepsilon_m)$ vs. $\ln(T\text{-}T_m)$ for the (0.76-x)BF-0.24PT-xBST ceramics.

### 3.4.3 Ferroelectric and piezoelectric properties

Fig. 3.16(a)-(c) shows the bipolar polarization hysteresis (*P*-*E*) loops, bipolar and unipolar *S*-*E* loops of (0.76-x)BF-0.24PT-xBST ceramics measured at 10 Hz, respectively. The shapes of hysteresis loops reflect the movement of the domain in the ferroelectric materials. In the case of the samples with low BST content, the hysteresis loop cannot reach the saturation level due to the high tetragonality, which suppresses the domain switching [101, 102]. With the decrease of tetragonality, well-saturated hysteresis loop can be observed under the same electric field. The substitution of BST into the BF-PT solutions leads to a decrease of tetragonality and a decrease of the internal compatibility stresses, which facilitates the domain switching. Fig. 3.16(d) shows the coercive field ($E_c$) and unipolar strain ($S$) depend on the compositions. As the BST content increases, the coercive field decreases and electric fled-induced strain increases.

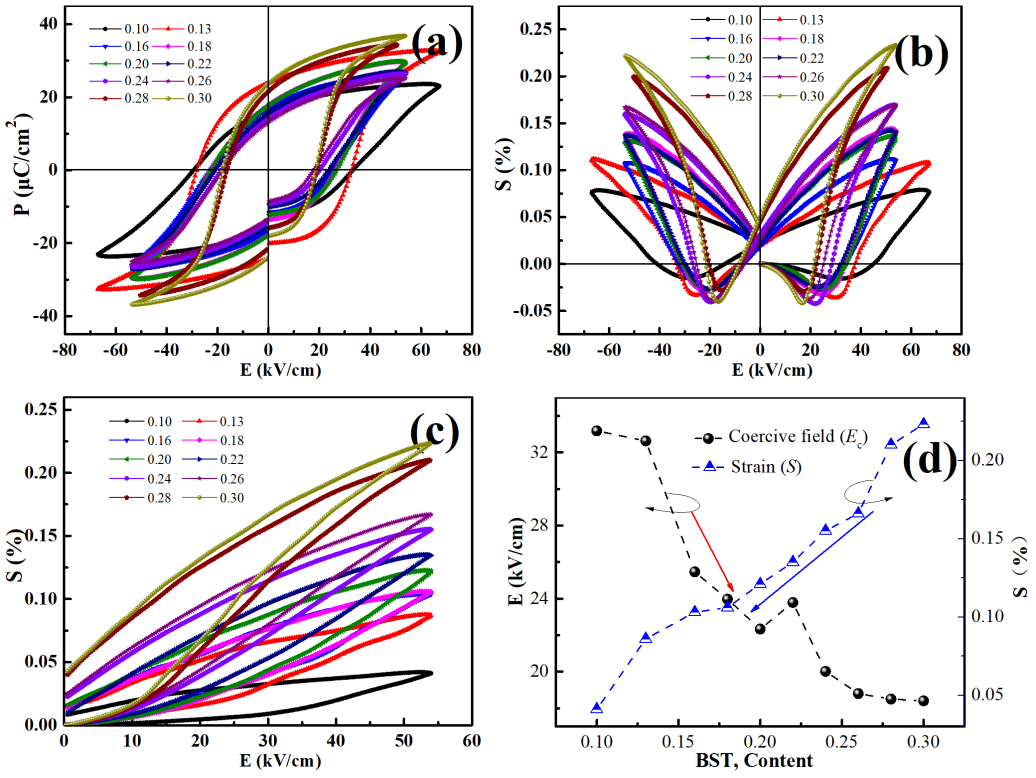


**Figure 3.16** (a) Bipolar polarization hysteresis loops; (b) bipolar *S*-*E* loops; (c) unipolar *S*-*E* loops of (0.76-x)BF-0.24PT-xBST ceramics at room temperature; (d) $E_c$ and unipolar strain values with varying BST content.

To evaluate the comprehensive properties of BST modified BF-PT solutions, the phase structure, tetragonality $c/a$, $\varepsilon$ (@1 kHz), tan$\delta$ (@1 kHz) $T_m$, $E_c$, $d_{33}$, electromechanical coupling factor $k_p$ and the strain $S$ of all samples are summarized in Table 3.3. It can be seen that the $d_{33}$ increases obviously with the phase structure evolving to the MPB regions, then reaches the maximum value 255 pC/N at the composition of BF-PT-0.2BST. Notably, obtaining the maximum piezoelectric constant can be correlated with the transition from $MPB_1$ (R+T) to $MPB_2$ (PC+T) for this composition as similarly reported in the system $Ba(Zr,Ti)O_3$-$(Ba,Ca)TiO_3$ [21-23]. The detailed reason will be discussed later in the domain characterization. It is worth noting that the electrostrain increases monotonously with x, while the maximum $d_{33}$ is obtained in the $MPB_1$ composition. Similar behavior has been widely reported in the BNT-based ceramics with strong strain responses [150]. The field-induced reversible phase transition from nonpolar to polar state contributes to the high electrostrain. The compositions with x>0.2 contain increased pseudo-cubic phase, where the nonpolar state may dominate in the high BST content samples (x=0.3). Therefore, although the maximum field-induced strain is obtained in the composition of x=0.3, the reversible domain evolution will lead to a low piezoelectric coefficient $d_{33}$. The $T_c$ of ferroelectrics decreases due to the weakening of the structural distortion when the BST content increases. In other words, the enhancement of piezoelectric performance is achieved in detriment of a high structural distortion (high $T_c$). Even so, a novel BF-PT based ternary system was designed with a high piezoelectric coefficient while retaining high Curie temperature, compared to other reported systems.

**Table 3.3** The structure and electric properties of (0.76-x)BF-0.24PT-xBST ceramics.

| Composition | Phase | $c_T/a_T$ | $T_m$ (°C) | $\varepsilon$ @1kHz | tan$\delta$ @1kHz | $E_c$ (kV/cm) | $d_{33}$ (pC/N) | $k_p$ | Strain(%) 55kV/cm |
|---|---|---|---|---|---|---|---|---|---|
| x=0.10 | R | - | 557 | 381.0 | 0.019 | 33.18 | 71 | 0.26 | 0.041 |
| x=0.13 | R+T | 1.058 | 529 | 571.3 | 0.015 | 32.63 | 121 | 0.41 | 0.086 |
| x=0.16 | R+T | 1.042 | 498 | 870.5 | 0.019 | 25.47 | 202 | 0.39 | 0.103 |
| x=0.18 | R+T | 1.035 | 467 | 945.8 | 0.017 | 23.97 | 245 | 0.42 | 0.106 |
| x=0.20 | R+T | 1.029 | 441 | 978.3 | 0.018 | 22.33 | 255 | 0.43 | 0.121 |
| x=0.22 | PC+T | 1.023 | 414 | 1066.6 | 0.019 | 23.78 | 232 | 0.36 | 0.135 |
| x=0.24 | PC+T | 1.019 | 382 | 1192.9 | 0.022 | 20.02 | 226 | 0.37 | 0.155 |
| x=0.26 | PC+T | 1.016 | 365 | 1287.3 | 0.025 | 18.8 | 206 | 0.32 | 0.166 |
| x=0.28 | PC+T | 1.010 | 346 | 1403.2 | 0.036 | 18.50 | 160 | 0.31 | 0.210 |
| x=0.30 | PC | - | 328 | 1465.8 | 0.042 | 18.40 | 110 | 0.31 | 0.223 |

## 3.4.4 High thermal stability

In addition, the stability of the piezoelectric performance after a thermal treatment is an important criterion for high-temperature piezoelectric materials. Thus, the variation of $d_{33}$ values after annealing the high-$T_c$ samples is shown in Fig. 3.17. Initially, $d_{33}$ keeps the stable values with increasing the annealing temperature. Then, a decline of $d_{33}$ occurs after annealing at temperatures near $T_c$, which corresponds to a depolarization temperature ($T_d$) about 450 °C. The $T_d$ of BF-PT-BST ceramics are higher than those of other perovskite ceramics, such as commercial PZT-5 (270 °C) or the high-performance $BiScO_3$-$PbTiO_3$ (370 °C) [151]. The best achieved value of $d_{33}$ value in BF-PT-0.16BST ceramic exceeds 200 pC/N even though the annealing temperature is up to 450 °C, which demonstrates an extremely high-temperature performance. Those results further reveal that the high thermal stability in BF-PT-BST ceramics, which is crucial to the high-temperature application of piezoelectric materials.

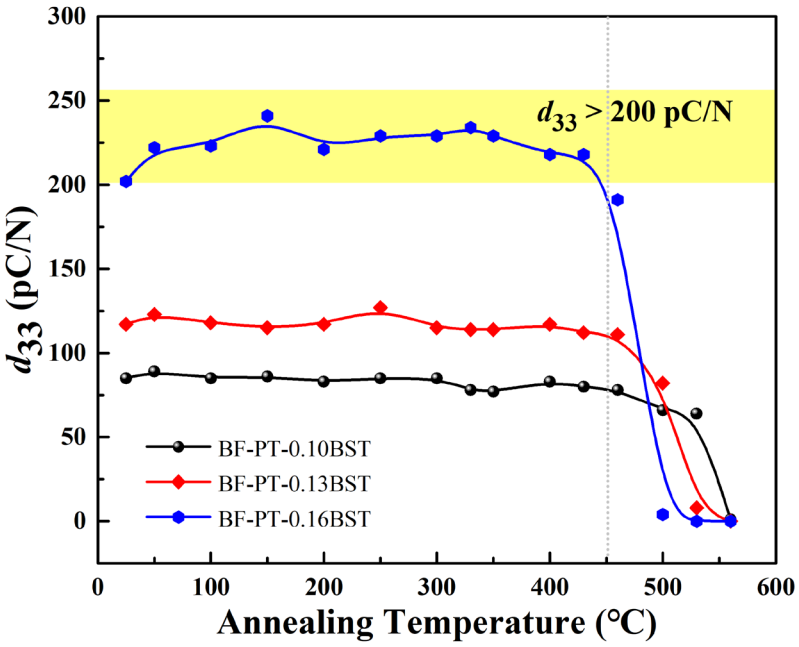


**Figure 3.17** The variation of $d_{33}$ values after thermal annealing for selected samples.

## 3.4.5 Domain configuration

Fig. 3.18 (a) and (b) show the electron diffraction (SAED) patterns on selected area of x=0.20 samples. It can be seen from Fig. 3.18(a) that the indices of lattice planes (100), (110), (210) and interplanar distances are consistent with the *P*4mm phase obtained by Rietveld refinement of the XRD patterns. Meanwhile, the electron diffraction pattern in Fig. 3.18(b) corresponds to the *R*3c phase. This result further confirms the coexistence of R and T phase in x=0.20 samples. In addition, the TEM bright-field images of domain configurations taken from x=0.20 samples are shown in Fig. 3.18(c). It can be clearly observed a large number of stripe-like nanodomains areas in TEM images. The representative strip-like nanodomains with an average width of 1.9 nm are shown in the inset. Typical nanoscale domains of 1-2 nm have been previously reported in KNN based ceramics, causing a giant piezoelectric response [152]. Previous reports revealed that the polymorphic phase regions are favorable for the formation of nanodomains in ferroelectric ceramics [19, 20]. The nanodomains aligned in a ferroelectric matrix can facilitate the polarization rotation and enhance the piezoelectric response [17, 20, 152], which is the main origin of the high piezoelectricity in the BF-PT-0.2BST ceramics.

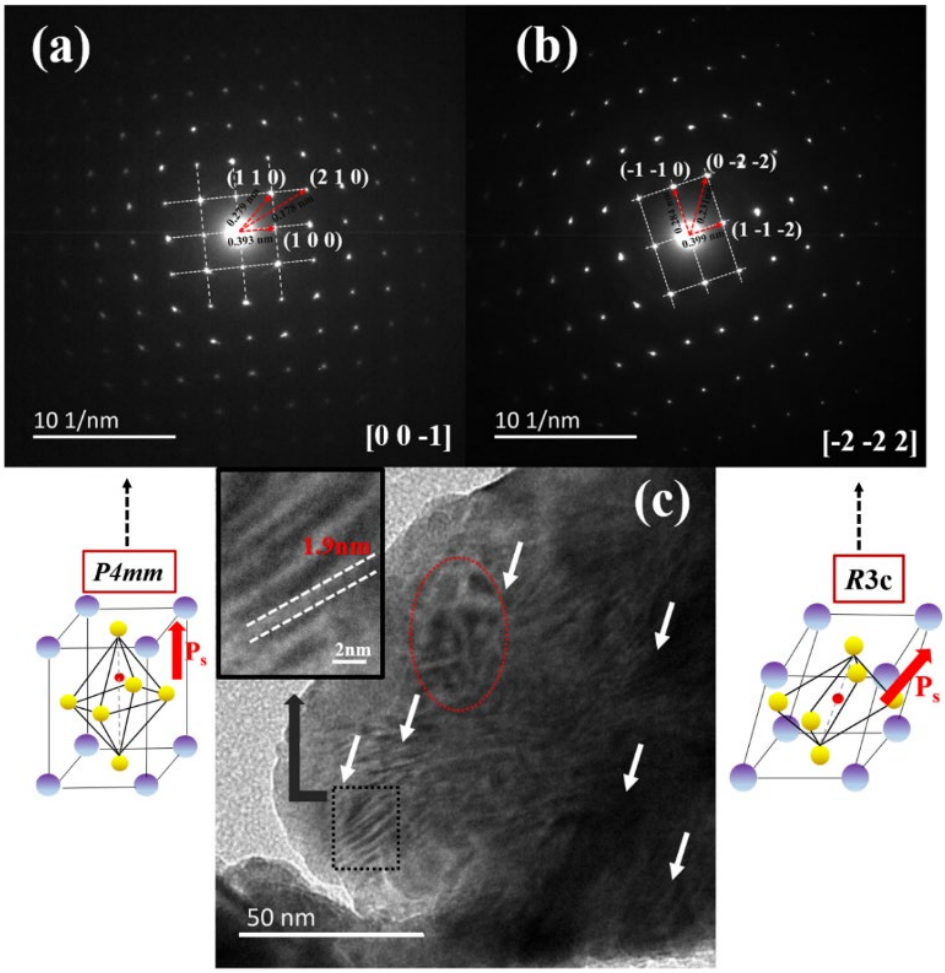


**Figure 3.18** (a)(b) SAED patterns taken from different grains of BF-PT-0.2BST ceramics correspond to tetragonal and rhombohedral phase, respectively; (c) TEM bright-field images of domain configurations of BF-PT-0.2BST ceramics.

## 3.4.6 The comparison of $d_{33}$ versus $T_c$

The comparison of $d_{33}$ versus $T_c$ values for other high curie temperature ceramics reported previously is shown in Fig. 3.19 [24, 25, 58, 66, 107, 115, 117, 153-159]. In terms of BF-PT based piezoelectric ceramics, high $d_{33}$ were recently achieved by the addition of $ABO_3$ compound or substitutional doping with the rare earth elements. Fig. 3.19(a) shows the comparison of comprehensive performance for modified BF-PT based ceramics. It should be pointed out that a high $T_c$ (>450 °C) is usually coupled with a lower $d_{33}$ (<100 pC/N) for the majority of BF-PT based ceramics. Piezoelectric properties of ceramics tend to be inversely proportional to the Curie temperature. By

introducing BST to BF-PT-based ceramics, substantially enhanced piezoelectricity was observed in the designed system. Furthermore, it can be seen from Fig. 3.19(b) that although high $d_{33}$ values were obtained in the commercially available PZT family, their $T_c$ was quite low (<400 °C). Piezoelectric ceramics with non-perovskite structures such as tungsten bronze and bismuth layer were found to possess higher Curie points, but with low $d_{33}$ values due to the structural limitation. $BiScO_3$-$PbTiO_3$ ceramics with a high $T_c$ possess good piezoelectricity ($T_c$ =450 °C, $d_{33}$=460 pC/N), which is superior to other $PbTiO_3$-$BiMeO_3$ based ceramics, nevertheless, costly ingredients ($Sc_2O_3$) greatly limit their practical application. In the present work, 0.6BF-0.24PT-0.16BST ceramic samples not only exhibit a large $d_{33}$ about 200 pC/N, but also a high $T_c$ about 500 °C. Thus, the relations composition-structure-property support that the BST-modified BF-PT based ferroelectric materials have great potential as high-temperature piezoelectric materials.

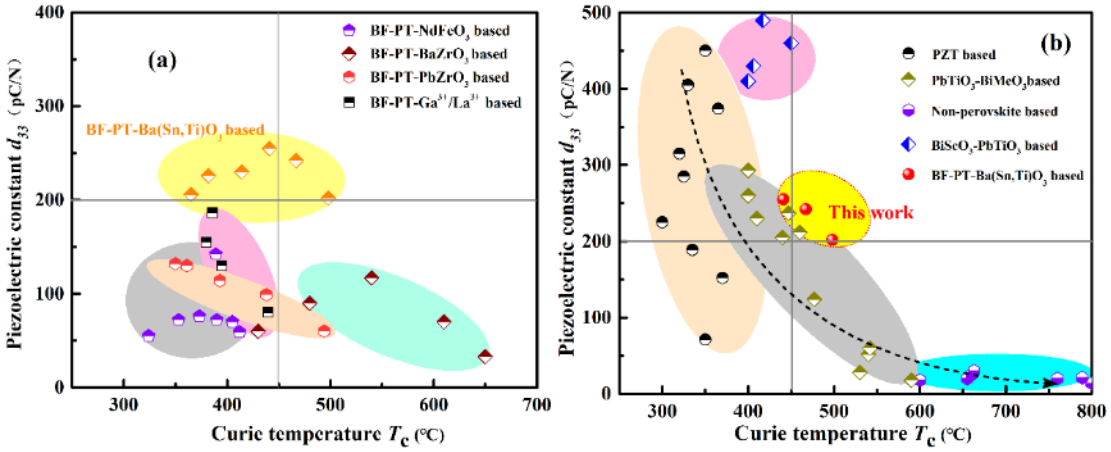


**Figure 3.19** A comparison of the $d_{33}$ and $T_c$ values among (a) the modified BF-PT-based ceramics reported previously; and (b) the canonical high Curie temperature ferroelectric ceramics.

## 3.5 Conclusions

In summary, PbO and $Pb_3O_4$ powder as the lead raw materials were used in the preparation of $BiFeO_3$-$PbTiO_3$ based ceramics. The structure and electrical properties of the ceramics have been analyzed. On the basis of the proper preparation

process, a novel modified $BiFeO_3$-based ferroelectric ceramics with both high $T_c$ and high $d_{33}$ were prepared by a conventional solid-state reaction process. The main results are summarized below:

(1) It turned out that the comprehensive electrical properties of $BiFeO_3$-$PbTiO_3$(PbO) sample were better than that of $BiFeO_3$-$PbTiO_3$($Pb_3O_4$) sample, which was quite different from other reports of lead-based piezoelectric ceramics. The concentration of the oxygen vacancy and $Fe^{2+}$ ion in $BiFeO_3$-$PbTiO_3$($Pb_3O_4$) sample is significantly higher than that in $BiFeO_3$-$PbTiO_3$(PbO) sample, which exactly confirm the cause of high conductivity in $BiFeO_3$-$PbTiO_3$($Pb_3O_4$) sample. The results demonstrated for the first time that the different lead raw materials have great influence on the performance of $BiFeO_3$-$PbTiO_3$ based piezoelectric ceramics.

(2) For the BF-PT-BST system, the incorporation of large ionic radius $Ba^{2+}$ at A-site and non-ferroelectric-active $Sn^{4+}$ at B-site generated a decrease of the tetragonality degree *c/a*. A wide multiphase coexistence region was formed with the content of BST ranging from 0.13 to 0.28.

(3) The enhanced piezoelectric coefficient ($d_{33}$~200 pC/N) was achieved while maintaining a high Curie temperature ($T_c$~500 °C) and a high depolarization temperature ($T_d$~450 °C) for the composition of 0.6BF-24PT-0.16BST. It indicates that the BST-modified BF-PT based ferroelectric ceramics have great potential as high-temperature piezoelectric materials.

(4) The enhanced piezoelectric properties can be correlated with a weakly distorted structure (low tetragonality) along with the wide morphotropic phase boundary (MPB) in the novel $BiFeO_3$-based ceramics. Furthermore, the presence of nanodomains (~2 nm) in the investigated MPB ceramics, which contributes to reducing domain wall energy and promoting the switching of domains.

# Chapter 4 Defect and pinning effect in $BiFeO_3$-based ceramics

## 4.1 Introduction

Defects or defect dipoles can have an important effect on the properties of ferroelectric materials. It is generally believed that the soft (donor) doping in Pb-based ceramics can cause lead vacancies, which favors the motion of ferroelectric domains. At this point, the ferroelectric ceramics realizes a small coercivity field $E_c$ and a small mechanical quality factor $Q_m$. In contrast, hard (acceptor) doping in Pb-based ceramics can cause high oxygen vacancy concentrations, which the defects are expected to strongly suppress the domain switching. Whatever the doping type, donors and acceptors produce different types of defects, which can alter the microstructure and electrical properties of the ferroelectric ceramics. As the characteristics of hard ferroelectric ceramics lie in higher $E_c$ and $Q_m$ factor, the study of the interaction between defects and ferroelectric domains plays an important role in modifying the performances of ferroelectric ceramics.

The hysteresis (*P-E*) loop reflects the characteristics of ferroelectric domains switching under the electric field. A sufficiently large electric field can make the ferroelectric domains oriented along its defined direction. When a reverse electric field is applied, these ferroelectric domains will be rotating while under positive and negative electric fields, ferroelectrics exhibit a symmetrical *P-E* loop. However, the anomalous *P-E* loops are often observed in some hard-doped piezoelectric ceramics, such as Mn-doped $Pb(Zr,Ti)O_3$, $BaTiO_3$ and $(Sr,Pb)TiO_3$ [160-163]. It is expressed as “double *P-E* hysteresis loops with the reduced remnant polarization" and “shifted *P-E* hysteresis loops along the field axis”. These anomalous *P-E* loops mainly originate from the influence of the interaction between defects and ferroelectric domains in hard-doped ferroelectric ceramics. Based on the different positions of the

defects, two models are mainly proposed to explain the interaction of defects dipoles with domains, namely the "volume effect" and the "boundary effect" [164, 165]. The former describes that the defects in piezoelectric ceramics occupy the lowest energy position in the lattice. According to the symmetry-conforming property of point defects, a defect dipole is formed along the direction of spontaneous polarization. Under the applied electric field, the defect dipole is not easy to switch and provides a restoring force to switch back the spontaneous polarization. The latter mainly means that the defects are driven by the electric and elastic forces to diffuse to the domain walls or grain boundaries and fix their positions, thereby hindering the motion of the ferroelectric domains.

On the other hand, it is generally believed that there are the defects such as Bi vacancies, oxygen vacancies, and $Fe^{2+}/Fe^{4+}$ can exist in the $BiFeO_3$-based ceramics, resulting in high leakage current of the ceramics [46]. It should be noted that the charged defects not only affect the ferroelectric properties, but also have a significant impact on the behavior of the ferroelectric domain switching. Yuan *et al*. [166] investigated the phenomenon of double *P-E* hysteresis loops in the $BiFeO_3$ ceramics and concluded that it was related to the restoring force of the defect dipoles. Rojac *et al*. [167] found that the charged defects in $BiFeO_3$ ceramics can inhibit domain wall movement and the mobility of the domain walls could be increased by quenching at temperatures higher than the Curie temperature. Geng *et al*. [168] combined scanning transmission electron microscopy (STEM), electron energy loss spectroscopy (EELS) and piezoresponse force microscopy (PFM) to reveal the pinning behavior of charged domain walls by oxygen vacancies in $BiFeO_3$ flims. Although many studies have been carried out, the relationship of pinning behavior with poling process, temperature, and electric field is still disputable.

In the previous chapter, we successfully prepared $BiFeO_3$-$PbTiO_3$-$Ba(Sn,Ti)O_3$ (BF-PT-BST) based high-temperature piezoelectric ceramics with high Curie temperature ($T_c$~500 °C) and high piezoelectric coefficient ($d_{33}$~200 pC/N), which have very promising applications in the field of high-temperature piezoelectric devices. However, practical applications of piezoelectric devices require

consideration of complex external environments (e.g., temperature, electric field, aging, and stress) that affect the ferroelectric and piezoelectric properties of ceramics. Meanwhile, the BF-PT-BST piezoelectric ceramics with high $BiFeO_3$ content exhibit the characteristics of domain wall pinning in the hard-doped ceramics, i.e., there are significant differences in the *P-E* loops for the unpoled and poled ceramics. It is necessary to have an in-depth study on the defect and domain wall pinning of BF-PT-BST based high-temperature piezoelectric ceramics.

Based on the above background, the present chapter aims to clarify the effects of the poling process, temperature, and electric field on the *P-E* loops and the electric field induced strain (*S-E* loops) for the BF-PT-BST based ceramics. Combining the phase structure, dielectric, leakage current and thermally stimulated discharge current properties for the unpoled and poled ceramics, a qualitative model is developed to explain the pinning phenomenon of BF-PT-BST based piezoelectric ceramics. The results provide some theoretical guidance for the performance optimization and practical application of BF-PT based ceramics

## 4.2 Experimental

(0.76-x)$BiFeO_3$-0.24$PbTiO_3$-x$Ba(Sn_{0.2}Ti_{0.8})O_3$ (BF-PT-BST) ceramics were prepared by a solid-state reaction method. The detailed preparation process is shown in Chapters 2 and 3 of this thesis. The ceramic samples were poled at 120 ℃ in a silicone oil bath under a DC field of 50 kV/cm for 30 min and placed at room temperature for 24h and then tested for electrical properties. The thermally stimulated discharge current for the poled ceramics were tested by Keithley 6517B micro galvanometer. The leakage current characteristics of ceramics were measured by the leakage current module of the ferroelectric analyzer.

## 4.3 Results

### 4.3.1 The ferroelectric properties for the unpoled and poled

## ceramics

Fig. 4.1(a) shows the *P-E* loops of the unpoled and poled $0.6BiFeO_3$-$0.24PbTiO_3$-$0.16Ba(Sn_{0.2}Ti_{0.8})O_3$ (0.6BF-0.24PT-0.16BST) ceramics. The unpoled 0.6BF-0.24PT-0.16BST ceramic shows a symmetrical *P-E* loop. While a pronounced asymmetric *P-E* loop can be observed in the poled ceramic. After poling, the remnant polarization $P_r$ and the maximum polarization $P_{max}$ of the poled ceramics increased significantly from 16.7 μC/cm$^2$ and 26.7 μC/cm$^2$ to 31.0 μC/cm$^2$ and 37.6 μC/cm$^2$, respectively. At the same time, the positive coercive field $E_+$ of the poled sample is maintained at about 25.6 kV/cm, while the negative coercive field $E_-$ increased from 22.6 kV/cm to 32.8 kV/cm. This phenomenon indicates that there is an internal bias field ($E_i$) in the poled 0.6BF-0.24PT-0.16BST ceramics, resulting in the shifted and asymmetric *P-E* hysteresis loops. The change of *P-E* hysteresis loops for unpoled and poled ceramics can also be understood from the current-electric field (*I-E*) loops, as shown in Fig. 4.1(b). After poling, the current peak at the negative electric field is shifted toward the high electric field, which indicates the high electric field for the domain switching. It also can be found that the poled ceramics exhibits a sharp current peak correlated with a large part of domain switching.

The formation mechanism of the internal bias field and its influence on the electrical properties have been reported in hard-doped PZT-based ceramics, mostly related to oxygen vacancies. It is well recognized that the formation of internal bias fields is correlated with defect dipoles (e.g., $(Fe'_{Zr,Ti} - V_O^{\cdot\cdot})^{\cdot}$) [133, 169]. After poling (high temperature and high DC electric field), the oxygen vacancies in the hard-doped piezoelectric ceramics migrate directionally and form defect dipoles arranged in the aligned polarization, creating an internal bias field. The defect dipoles can stabilize the domain configuration due to its low mobility under the electric field [160, 170, 171]. As a result, the shifted *P-E* hysteresis loops along the field axis can be observed in the poled 0.6BF-0.24PT-0.16BST ceramics. For the $BiFeO_3$-based ceramics, the lattice will inevitably produce oxygen vacancies due to the $Bi_2O_3$ is easy to volatilize at high temperature. It is reported that there are the

defects such as Bi vacancies, oxygen vacancies, and $Fe^{2+}/Fe^{4+}$ that can exist in the $BiFeO_3$-based ceramics [46, 172]. Therefore, the defect dipoles such as $(V_{Bi}''' - V_O^{\cdot\cdot})'$ and $(Fe_{Fe}' - V_O^{\cdot\cdot})^{\cdot}$ can be formed in the BF-PT-BST based ceramics, resulting in a large internal bias field.

Fig. 4.1(c) shows the bipolar electric field induced strain (*S*-*E* loops) for the unpoled and poled 0.6BF-0.24PT-0.16BST ceramics. It can be found that the strain is very small (~0.11 %) for the unpoled ceramics and the curve is symmetric. However, for the poled ceramics, the strain increased significantly to 0.39 %. Importantly, the *S*-*E* loops of the poled ceramics is similar to the *P*-*E* loops, showing an asymmetric shape. This phenomenon is also due to the formation of a large internal bias field (~29.9 kV/cm) for the ceramics after poling. It is worth noting that the poled 0.6BF-0.24PT-0.16BST ceramics show a strain memory effect [161], which can reach 0.26 %. On the one hand, the randomly distributed defects have sufficient energy to migrate in the poling direction, resulting in the decrease of the pinning effect. On the other hand, the domain wall density decreases during the poling process, which contributes to the mobility of the domains. As a result, these factors lead to a significant increase in the electrostrain of the ceramics after poling. Similarly, comparing the unipolar electric field induced strain of the unpoled and poled ceramics, as shown in Fig. 4.1(d), the unipolar strain along with the poling direction increases from 0.10 % to 0.14 % after poling process under an electric field of 55 kV/cm.

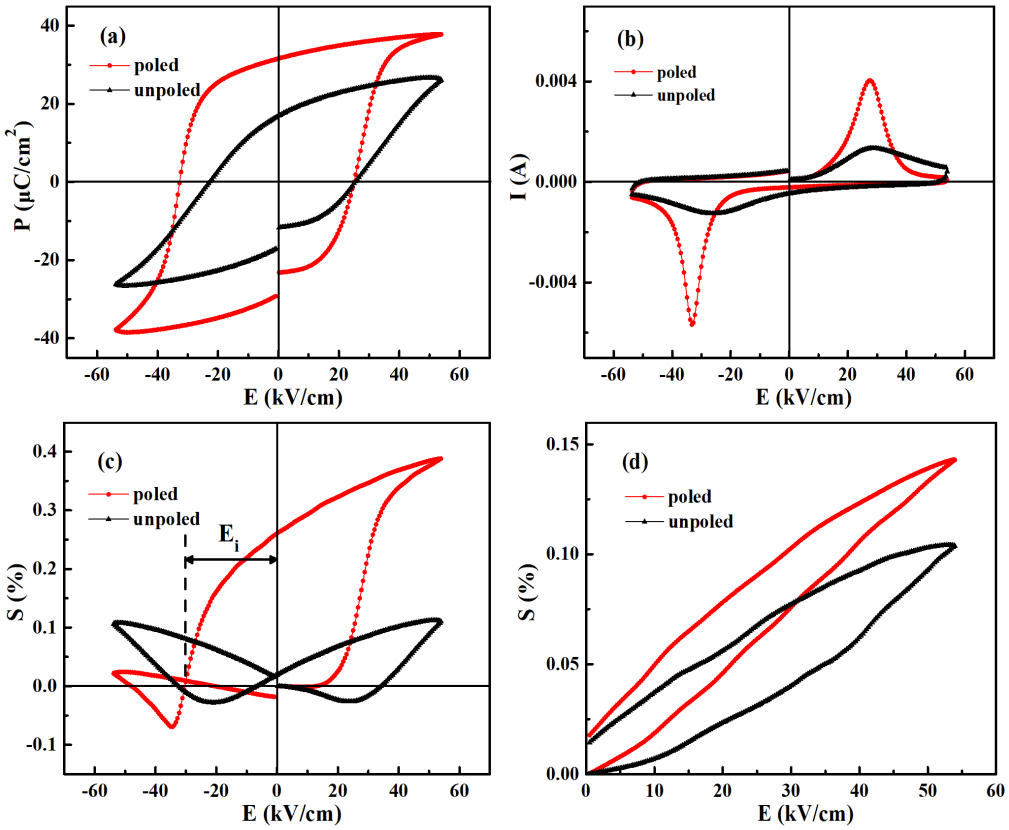


**Figure 4.1** (a) The bipolar polarization hysteresis (*P-E*) loops; (b) current-electric field *(I-E)* loops; (c) bipolar and (d) unipolar *S-E* loops of the poled and unpoled 0.6BF-0.24PT-0.16BST ceramics.

## 4.3.2 Formation of internal bias field

The XRD patterns of the unpoled and poled 0.6BF-0.24PT-0.16BST ceramic samples are shown in Fig. 4.2. Overall, there is no significant change in the phase structure of the ceramics before and after poling. According to the (200) peak, the fitting results show that the ratio of the rhombohedral (R) and the tetragonal (T) phase content for the ceramics changes slightly from 40/60 to 49/51 after the poling process. This phenomenon was also reported previously in BF-PT based piezoelectric ceramics [153], where the applied electric field led to a polarization rotation from $(100)_T$ to $(111)_R$ and a slight increase in the R phase content after the removal of the electric field. It should be noted that the slight increase in the R phase content for the poled ceramics does not cause a large structural phase-change in the material, such as the electric-field-induced phase-changes behavior reported in

$(Na_{1/2}Bi_{1/2})TiO_3$ (BNT) based piezoelectric ceramics[150]. Even if a slight increase in the R phase content will affect the ferroelectric properties of ceramics, it is impossible to make such a significant difference in *P-E* and *S-E* loops of the ceramics before and after poling. Therefore, it is reasonable to believe that the main reason for the significant changes in ferroelectric properties before and after poling is the defect dipoles effect.

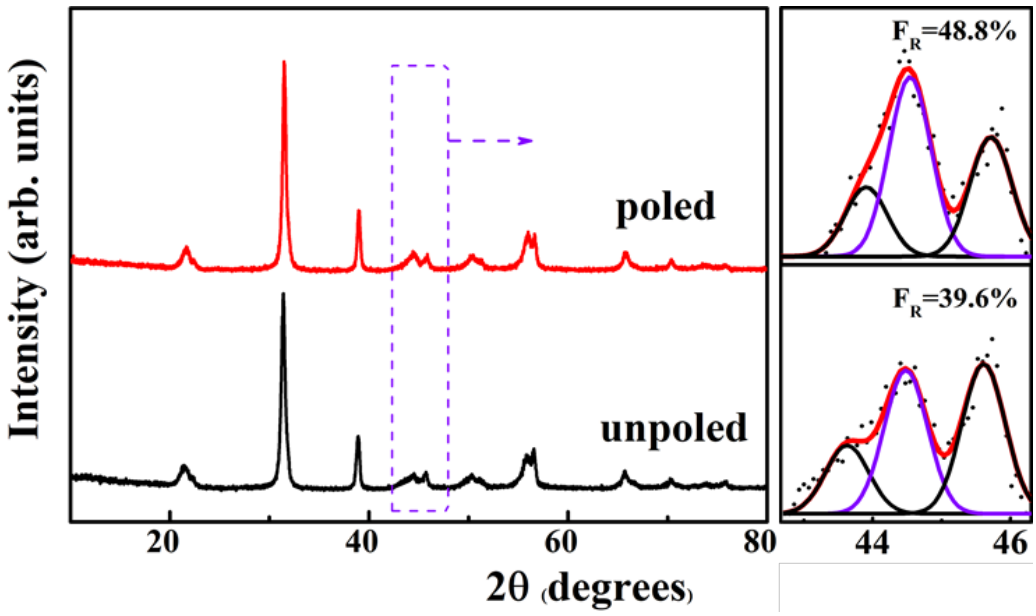


**Figure 4.2** XRD pattern of the poled and unpoled 0.6BF-0.24PT-0.16BST ceramics.

Fig. 4.3(a) shows the temperature dependencies of $\varepsilon_r$ and tanδ for the unpoled and poled 0.6BF-0.24PT-0.16BST ceramics. The poling process does not change the Curie temperature of ferroelectric ceramics, which is still up to about 500 ℃. It can be seen from the local magnification inset that the dielectric constant of the poled ceramics increases significantly at about 100 ℃. The abnormal increase in dielectric loss for poled ceramics may be related to the migration of oxygen vacancies at high temperatures [173]. In addition, the behavior of phase transitions and dipole rotation in ferroelectric ceramics was investigated by the thermally stimulated discharge current (TSDC) [165, 174]. Fig. 4.3(b) represents the TSDC curves for the poled 0.6BF-0.24PT-0.16BST ceramic samples, the test temperature range is -50℃ - 280 ℃, and the heating rate is 2 ℃/min. A current peak can be observed at about 100 ℃. Combined with the variation of piezoelectric properties after thermal

annealing in the previous chapter, it is clear that the 0.6BF-0.24PT-0.16BST ceramics have no intrinsic depolarization effect at about 100 °C. Therefore, the current peak should be related to the defect dipoles formed by oxygen vacancies. It is generally believed that the reorientation of defect dipoles involves the migration of oxygen vacancies. As the temperature rises, the oxygen vacancies can migrate by diffusion and the defect dipoles can be released and then leading to a thermally stimulated discharge current [165]. It should be noted that due to the limitation of the instrument testing temperature (below 300 °C), there is no current peak at the phase transition point (about 500 °C) in the current curve. The combined dielectric temperature spectrum and thermally excited current test results further confirm the presence of defect dipoles within the poled 0.6BF-0.24PT-0.16BST ceramics. A large internal bias field can be generated in the ceramics, which leads to its asymmetrical *P-E* and *S-E* loops.

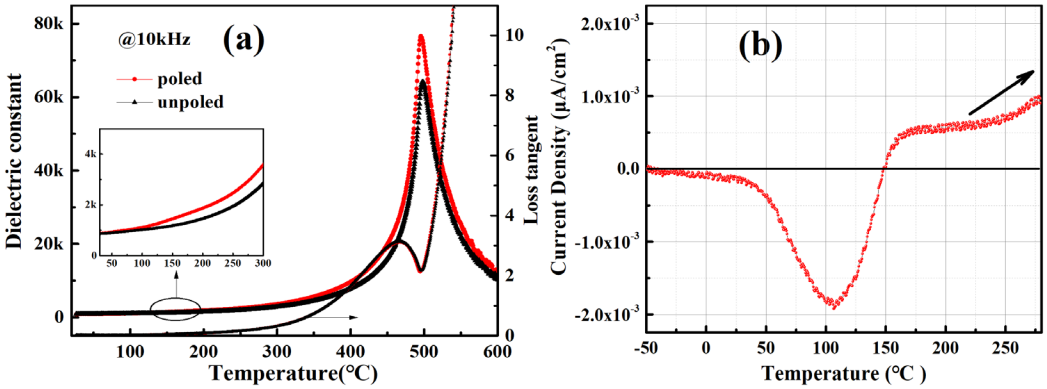


**Figure 4.3** (a) The temperature dependencies of $\varepsilon_r$ and *tan*δ for the poled and unpoled 0.6BF-0.24PT-0.16BST ceramics; (b) TSDC curves of the poled 0.6BF-0.24PT-0.16BST ceramics.

Fig. 4.4 shows the leakage current (*J-E*) curve of the unpoled and poled 0.6BF-0.24PT-0.16BST ceramics. First, the leakage current under 50 kV/cm electric field is less than $10^{-6}$ A/cm$^2$, which is lower than other reported BFO-based piezoelectric ceramics [175]. It is worth mentioning that the leakage current of the poled sample is significantly reduced, from $8.0\times10^{-7}$ A/cm$^2$ to $0.18\times10^{-7}$ A/cm$^2$. This result may be related to the redistribution of the charged defects (oxygen vacancies)

at the domain walls during the poling process. Borkar et al. [176] reported a significant reduction in leakage current for the Al-doped (Na,Bi)$TiO_3$-based piezoelectric ceramics after poling. They suggested that the effective poling process could neutralize the domain pinning and fill the oxygen vacancies at the grain boundaries. In present work, the analysis of leakage current performance for the ceramics further confirms that the poling process leads to the migration of defects.

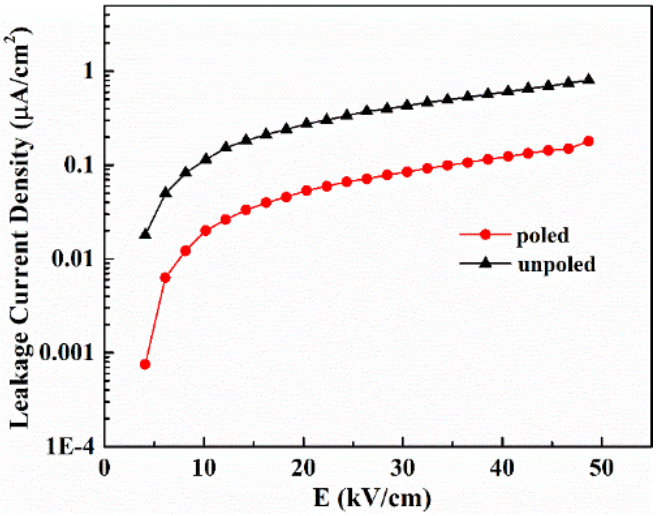


**Figure 4.4** Leakage current density as a function of electric field for the poled and unpoled 0.6BF-0.24PT-0.16BST ceramics.

## 4.3.3 Reorientation of defect dipoles

As discussed before, the reorientation of defect dipoles involves the migration of oxygen vacancies. It is reported that changing the temperature (increasing the temperature) or the electric field (decreasing the frequency) can make it easier for the migration of oxygen vacancies, thus leading to the reorientation of defect dipoles.

To verify the effect of temperature on the defect dipoles and the internal bias field, the *P-E* and *S-E* loops of the poled 0.6BF-0.24PT-0.16BST ceramics at different temperature are shown in Fig. 4.5. With the temperature increases, the shape of *P-E* and *S-E* loops gradually changes from asymmetric to symmetric. The normal hysteresis P-E loops for the poled ceramics can be obtained when the temperature is 120 ℃. As shown in Fig. 4.7(a), the value of $E_i$ of the ceramics

gradually decreases from 27.2 kV/cm to 0 kV/cm and the remnant polarization $P_r$ increases from 22.9 μC/cm$^2$ to 40.2 μC/cm$^2$ with the temperature increases from 25 °C to 180 °C. The above results indicate that the defect dipole effect weakens with increasing the temperature. The reason is mainly due to the oxygen vacancies having a large energy to migrate at high temperature, resulting in the rearrangement of defect dipoles with the direction of the applied electric field. In this case, the defect dipoles of the poled ceramics would be decoupled, so that the internal bias field disappears and the shape of *P*-*E* and *S*-*E* loops becomes symmetrical.

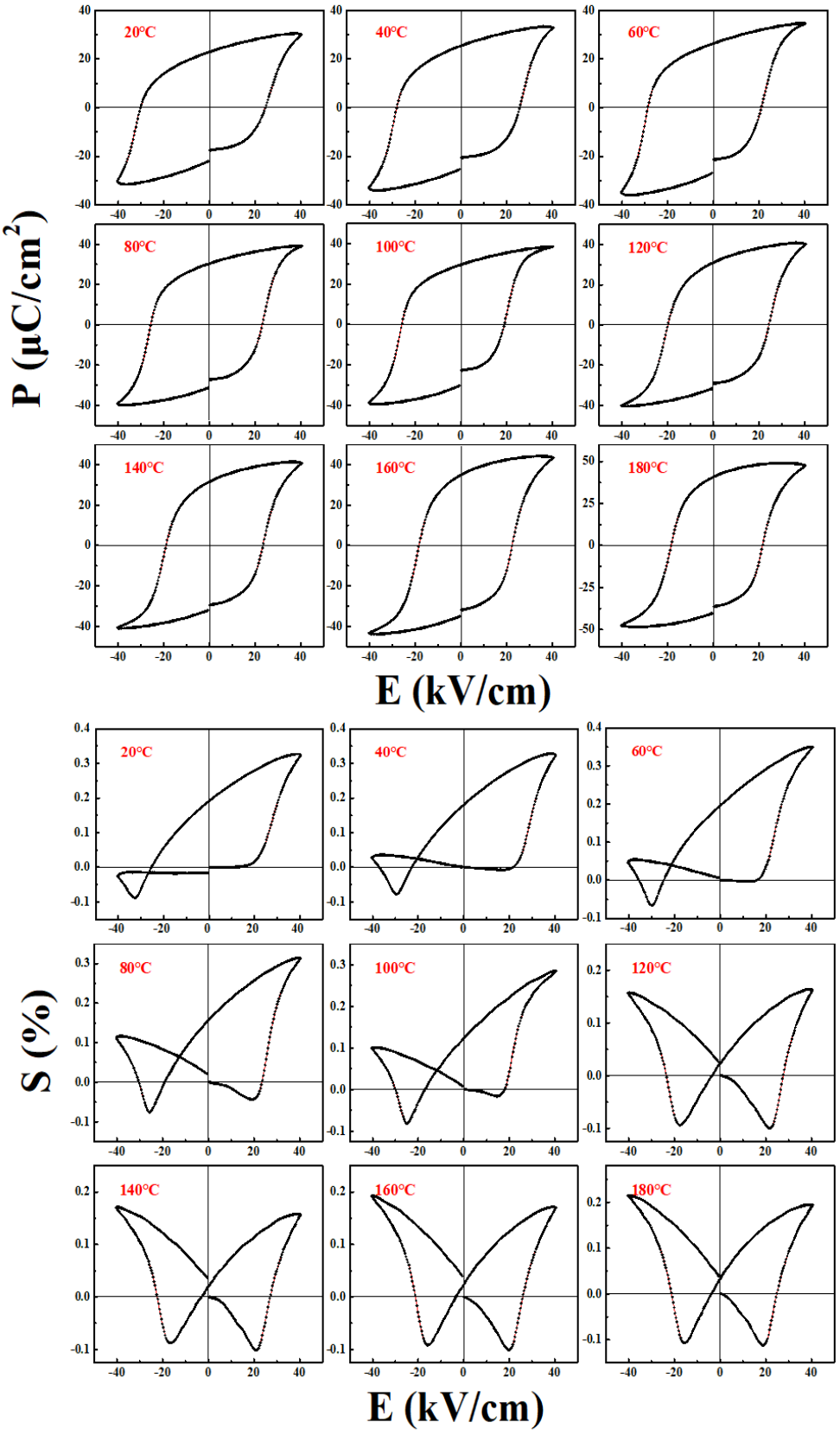


**Figure 4.5** The temperature-dependent of the hysteresis (*P-E*) loops and the bipolar *S-E* loops for the poled 0.6BF-0.24PT-0.16BST ceramics.

On the other hand, the frequency of the applied electric field also has an important effect on the defect dipoles. Fig. 4.6 shows the *P-E* and *S-E* loops of the poled 0.6BF-0.24PT-0.16BST ceramics at different electric field frequencies, the frequency range is 0.01 Hz-50 Hz. As expected, the asymmetry of the hysteresis *P-E* loops of the poled ceramics gradually decreases with the decrease of the applied electric field frequency. As shown in Fig. 4.7(b), with the frequency decreases from 50 Hz to 0.01 Hz, the value of $E_i$ gradually decreases from 20.0 kV/cm to 10.8 kV/cm, and the $P_r$ increases from 24.3 μC/cm$^2$ to 38.9 μC/cm$^2$. Under the high-frequency applied electric field, the defect dipoles haven't a sufficient time to switch due to the slow migration of oxygen vacancies. However, as the frequency decreases, the defect dipoles have enough time to follow the direction of the electric field. Therefore, the corresponding internal bias field decreases and the shape of *P-E* and *S-E* loops becomes symmetrical. In this experiment, the internal bias field still exists in the poled ceramics at low frequencies (0.01 Hz), which may be related to the fact that the applied electric field frequency is not low enough.

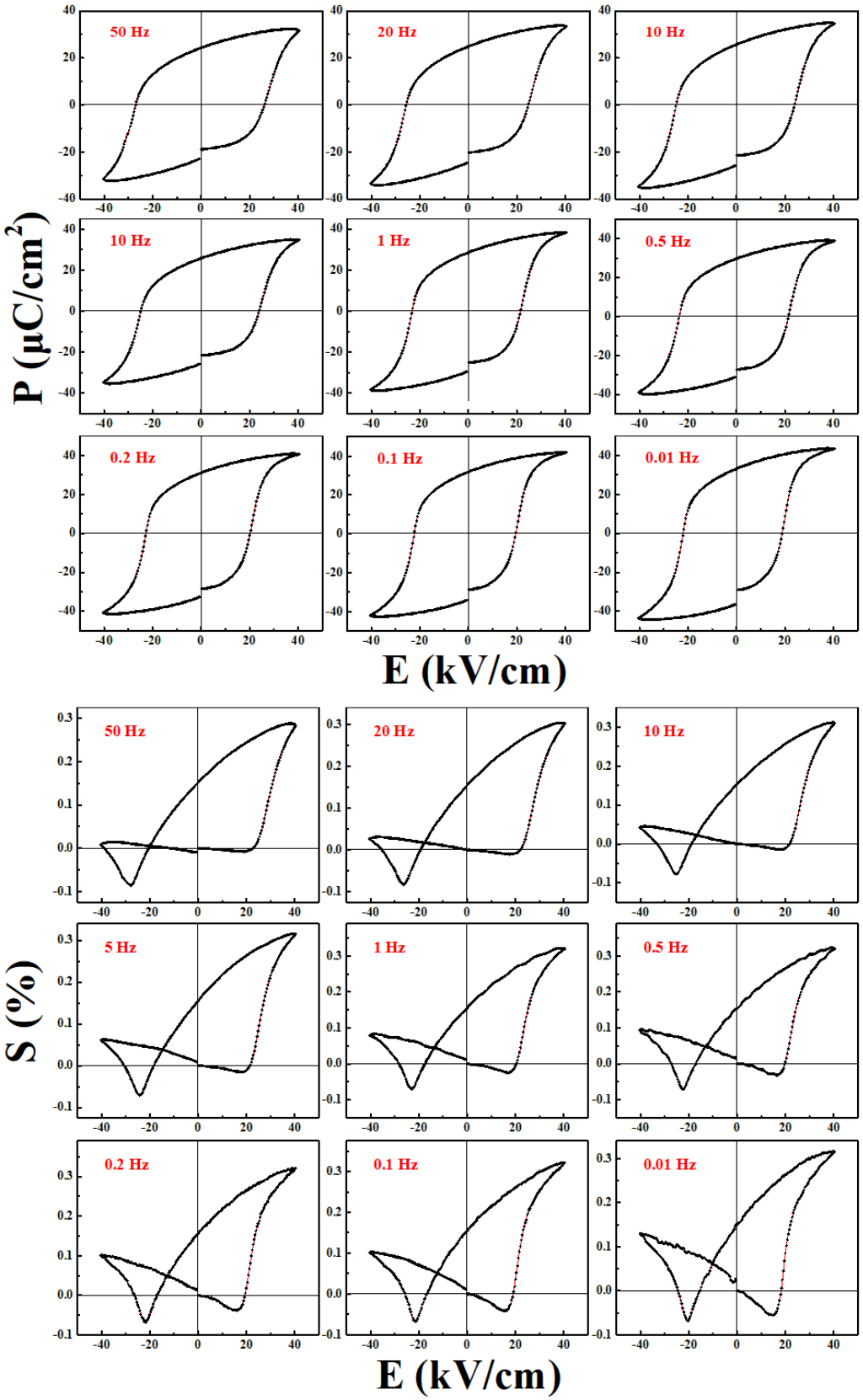


**Figure 4.6** The frequency-dependent of the hysteresis (*P-E*) loops and the bipolar *S-E* loops for the poled 0.6BF-0.24PT-0.16BST ceramics.

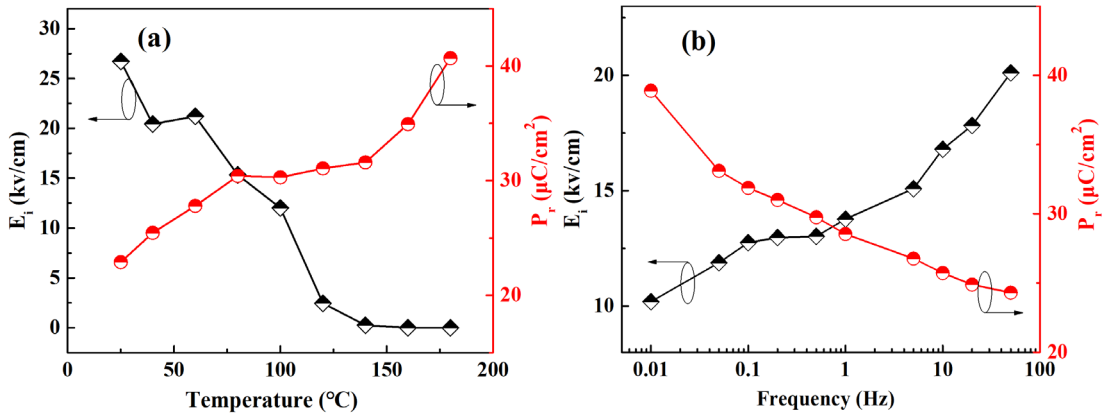


**Figure 4.7** (a) The temperature dependences of $E_i$ and $Pr$ for the poled 0.6BF-0.24PT-0.16BST ceramics; (b) the frequency dependences of $E_i$ and $Pr$ for the poled 0.6BF-0.24PT-0.16BST ceramics.

### 4.3.4 Comparison of internal bias fields for BF-PT-xBST ceramics

The above work mainly focuses on the formation of the internal bias field caused by the defect dipoles in the poled 0.6BF-0.24PT-0.16BST piezoelectric ceramics. To investigate the effect of BST doping on the defect pinning of BF-PT based ceramics, the *P-E* loops of the unpoled and poled (0.76-x)BF-0.24PT-xBST (x = 0.13, 0.16, 0.18, 0.22, 0.26, 0.3) ceramics are shown in Fig. 4.8. After poling, the shift and asymmetric hysteresis loops can be obtained in the BF-PT-xBST ceramics with low BST doping content (x = 0.13, 0.16, 0.18), which is similar to the 0.6BF-0.24PT-0.16BST ceramics above. At the same time, the values of maximum polarization $P_{max}$ and $P_r$ both increase significantly for the ceramics after poling. With the increase of BST doping content, the difference of the hysteresis *P-E* loops for the unpoled and poled ceramics gradually decreases. Predictably, the *S-E* loops of BF-PT-xBST ceramics show the same results, as depicted in Fig. 4.9. Specifically, Fig. 4.10(a) points out the internal bias field ($E_i$) of the poled BF-PT-xBST ceramics. It can be seen that with the increase of the BST doping content, $E_i$ of the poled BF-PT-xBST ceramics gradually decreases, from 38.2 kV/cm at x=0.13 to 6.9 kV/cm at x=0.3. Also, the strain memory reflecting the characteristics of the defect

dipoles in poled ceramics gradually decreases from 0.38 % at x=0.13 to 0.10 % at x=0.3, as shown in Fig. 4.10(b).

As mentioned earlier, defects such as Bi vacancies, oxygen vacancies, and $Fe^{2+}/Fe^{4+}$ are generated in the $BiFeO_3$-based ceramics during the preparation process [46]. The directional arrangement of these charged defects produces an internal bias field, which causes the strong asymmetric *P-E* loops in the poled ceramics. In the present work, BF-PT-xBST ceramics with different BST doping content exhibit significantly different phenomenon in hysteresis loops for unpoled and poled ceramics, which may be related to the concentration of charged defects in the ceramics. It is reasonable to suggest that the content of $Bi^{3+}$ ions and $Fe^{3+}$ ions decreases with the increase of BST doping content, which reduces the concentration of charged defects caused by Bi volatilization and the fluctuation of Fe valence state. Therefore, the normal hysteresis *P-E* loops are observed in the poled BF-PT-xBST ceramics with high BST doping content. This result has been reported previously in other systems. Huang et al. [163] found that the difference in the oxygen vacancies content leads to the variation of defect dipoles, which affects the pinning phenomenon of $Sr_{1-x}Pb_xTiO_3$ system.

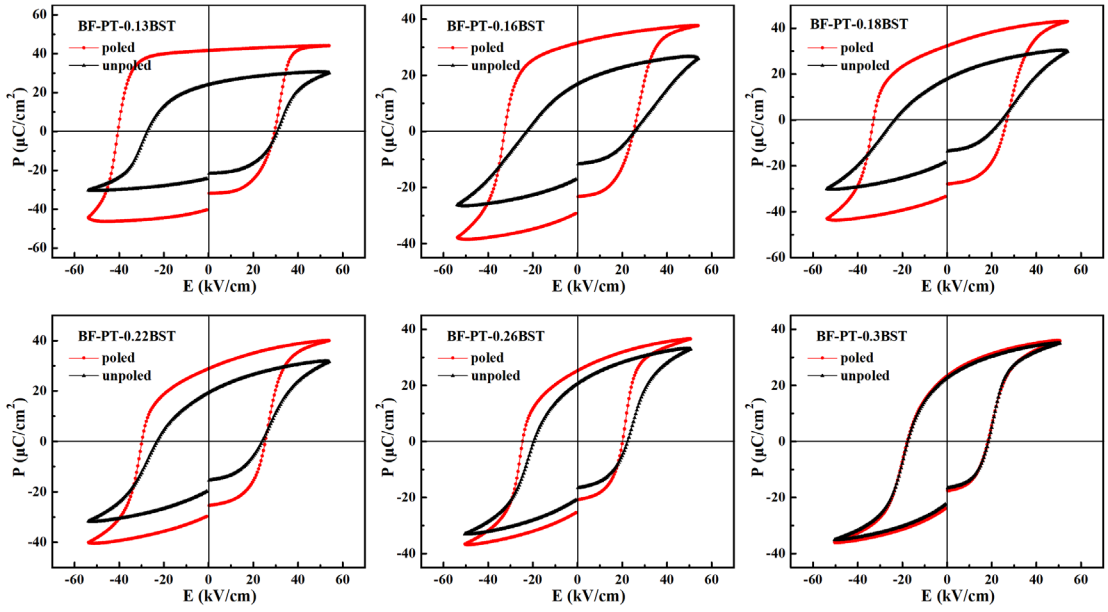


**Figure 4.8** The hysteresis (*P-E*) loops of the poled and the unpoled (0.76-x)BF-0.24PT-xBST (x=0.13, 0.16, 0.18, 0.22, 0.26, 0.3) ceramics

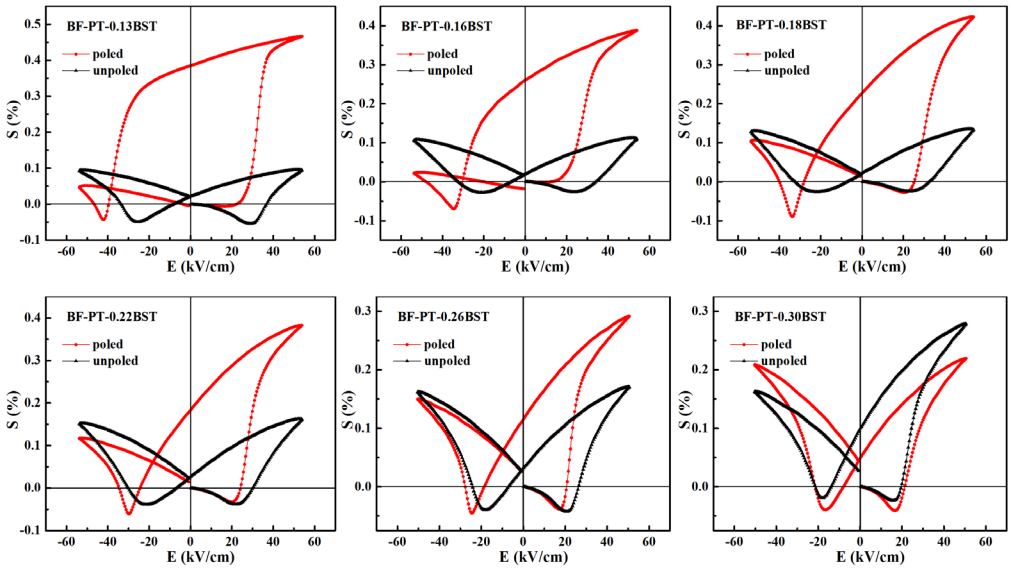


**Figure 4.9** The bipolar *S-E* loops of the poled and the unpoled (0.76-x)BF-0.24PT-xBST (x=0.13, 0.16, 0.18, 0.22, 0.26, 0.3) ceramics.

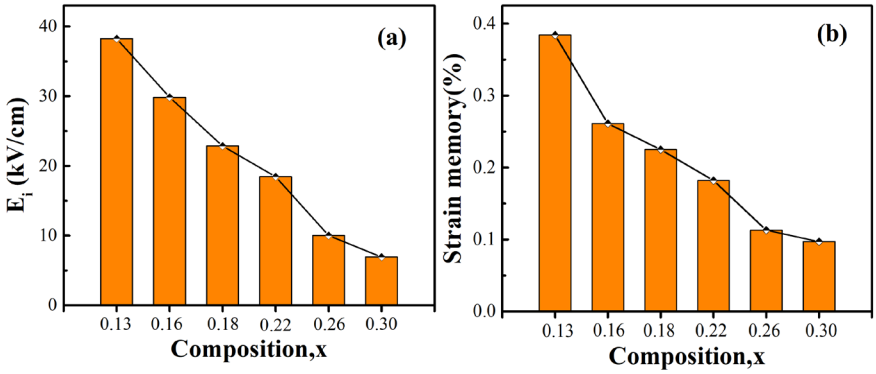


**Figure 4.10** (a) The internal bias field $E_i$; and (b) the strain memory for the poled (0.76-x)BF-0.24PT-xBST (x=0.13, 0.16, 0.18, 0.22, 0.26, 0.3) ceramics.

## 4.3.5 Variation of ferroelectric properties with temperature

Fig. 4.11(a) shows the temperature-dependent hysteresis *P-E* loops of the unpoled (0.76-x)BF-0.24PT-xBST ceramics. The specific parameters of the ferroelectric performance ($P_{max}$, $P_r$ and coercive field $E_c$) as a function of temperature are also shown in Fig. 4.11(b). It should be pointed out that in order to avoid the error in the polarization intensity caused by the high-temperature leakage current, the maximum test temperature of the samples with x=0.1 and x=0.18 is 140 ℃ and 160 ℃, respectively. As can be seen from Fig. 4.11, the variation in the *P-E*

loops with varying temperatures for the BF-PT-xBST ceramics with different BST doping content is significantly different. Firstly, for the BF-PT-xBST ceramics with low BST doping content (x=0.1, 0.18, 0.24, 0.26), a typical square hysteresis loop can be observed at the high temperature. The values of $P_{max}$ and $P_r$ both increase from 23.5 μC/cm$^2$ and 14.7 μC/cm$^2$ to 43.6 μC/cm$^2$ and 34.5 μC/cm$^2$ with increasing temperature from 20 ℃ to 200 ℃ for the sample of x=0.24. For these samples, the high concentration of oxygen vacancies generated by Bi volatilization leads to a strong pinning effect in the ceramics. Therefore, the hysteresis loop is not easily opened at room temperature and the polarization intensity is low. As the temperature increases, the pinning effect decreases and the domain wall mobility increases, which leads to the enhancement of polarization. In contrast, for the BF-PT-xBST ceramics with high BST doping content (x=0.28, 0.3), the normal square hysteresis loops gradually change to thin shapes with increasing temperature. The values of $P_{max}$ and $P_r$ show different changes, the former increases gradually, while the latter decreases gradually. As mentioned in the previous chapter, with the addition of BST, the BF-PT-xBST ceramics with pseudo-cubic (PC) phases exhibit the nonergodic relaxor characteristics. In general, as the temperature increases, the transformation of nonergodic to ergodic relaxor state will occur. Also, the polar nanometer-sized regions (PNRs) will be distributed and exist in an ergodic relaxor state, resulting in a thin hysteresis loop for the ceramics [177]. Therefore, the increase of $P_{max}$ and the decrease of $P_r$ with increasing temperature for ceramics may be related to the increase of the ergodic relaxor phase. In addition, it should be noted that the high temperature provides higher thermal fluctuation to the polarization order parameter, which causes a decrease in the coercive field of the ferroelectric ceramics [178]. However, the $E_c$ of the samples with x = 0.1-0.18 increases slightly with increasing temperature, which may be related to the hysteresis loops not being fully opened at room temperature.

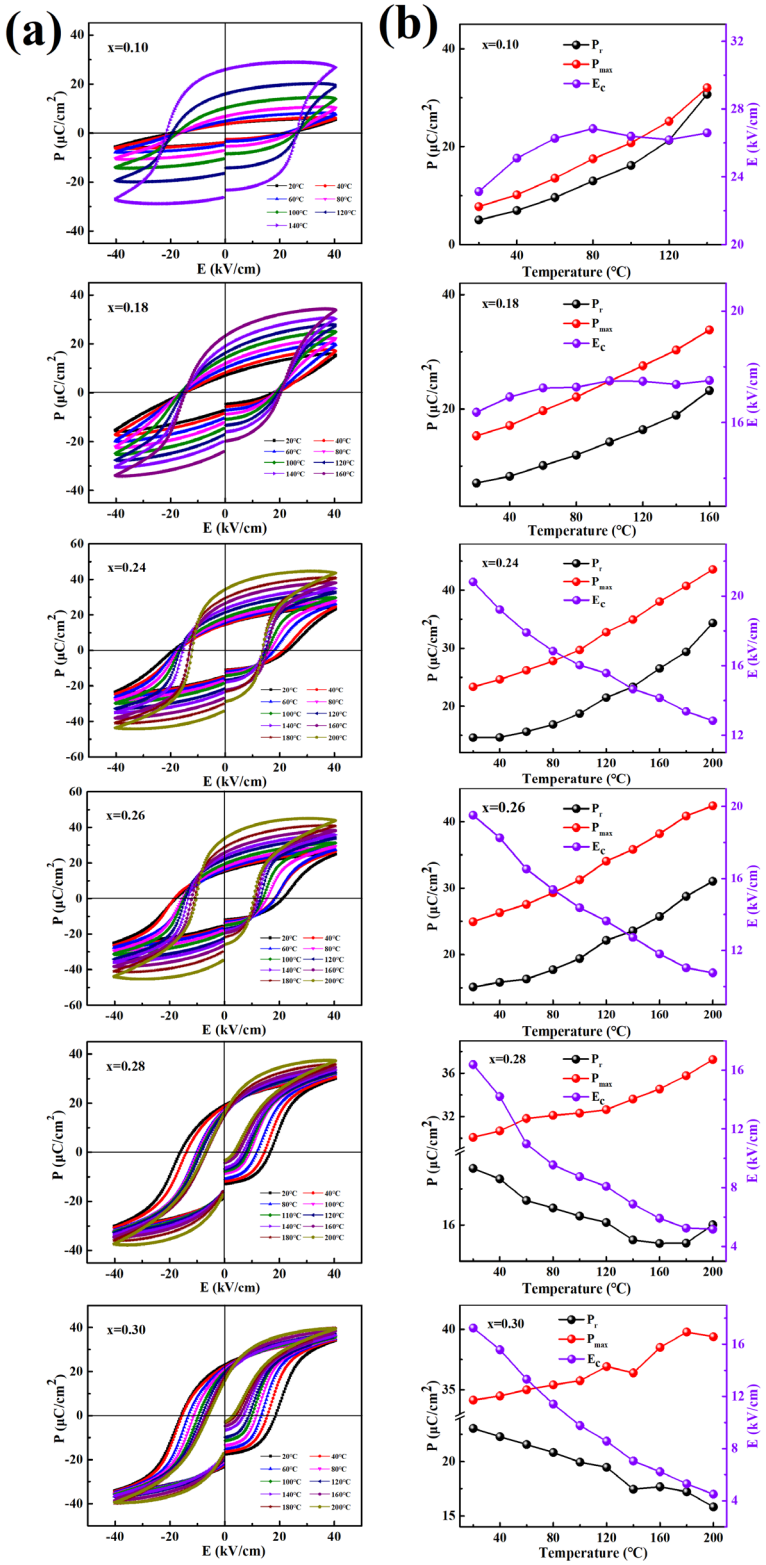


**Figure 4.11** (a) Temperature-dependent hysteresis (*P-E*) loops of the unpoled (0.76-x)BF-0.24PT-xBST ceramics; (b) the variation of $P_{max}$, $P_r$ and $E_c$ as a function of the temperature.

The temperature-dependent unipolar *S-E* loops of the unpoled (0.76-x)BF-0.24PT-xBST ceramics are shown in Fig. 4.12(a), the test electric field is constant at 40 kV/cm. The unipolar strain of all samples increases with the temperature. In particular, the increase in the strain for ceramics with low BST content at high temperatures is significantly higher than that of samples whit high BST content. For the sample with x=0.18, the unipolar strain increases from 0.005 % at 20 ℃ to 0.215 % at 180 ℃ under an electric field of 40 kV/cm. The significant increase of the strain with increasing temperature may be attributed to the decrease of the coercive field and the weakening of the domain wall pinning effect at high temperatures. For the samples with high BST doping , the unipolar strain does not vary substantially with the temperature and remain at about 0.2 %. For these samples, most of the ferroelectric domains are able to orient with the electric field and then leading to a large electrostrain at room temperature.

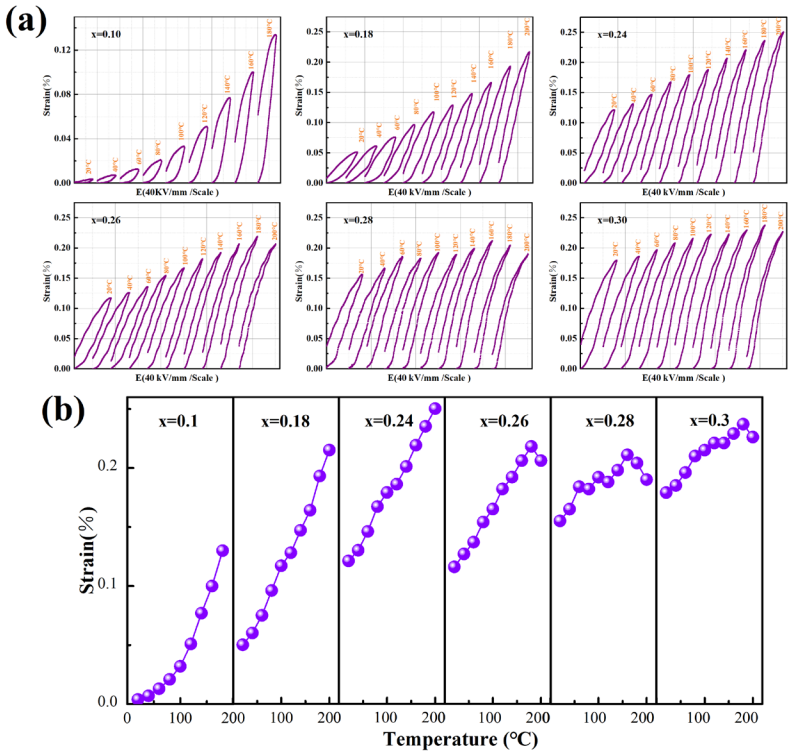


**Figure 4.12** Temperature-dependent unipolar *S-E* loops of the unpoled (0.76-x)BF-0.24PT-xBST ceramics; (b) the variation of strain (@40kV/cm) as a function of the temperature.

### 4.3.6 Model building

It is generally believed that the diffusion of charged defects to domain walls or grain boundaries will pin the domain walls and inhibit the motion of ferroelectric domains. This is due to the presence of the local strain field in the domain walls and discontinuous polarization, which causes an interaction between the domain walls and the randomly distributed charged defects [179]. For the $BiFeO_3$-based piezoelectric ceramics, mobile charge carriers such as oxygen vacancies can diffuse into the non-neutral domain walls and cause the pinned domain walls [180]. Fig. 4.13 shows the model of the defect pinning effect in BF-PT-BST based ceramics. At high temperature, the ceramic is in the paraelectric phase, that is, there is no polarization orientation inside the ceramic, corresponding to the state Fig. 4.13(a). When cooled down below $T_c$, it transforms into a ferroelectric phase, where the spontaneous polarization $P_S$ with random orientation exists in each grain of the ceramics. The presence of charged defects at the domain walls, such as oxygen vacancies, act as pinning centers can inhibit the motion of domain walls, leading to small polarization intensity and electrostrain, as illustrated in Fig. 4.13(b). When the ceramics are poled under high temperatures and high electric fields, the oxygen vacancies have enough energy to migrate and form the defect dipole moments $P_D$, such as $(Fe'_{Fe} - V_{\ddot{O}})^{\cdot}$. According to the symmetry-conforming property of point defects [162], the direction of $P_D$ should be consistent with the direction of $P_S$ due to the presence of restoring force. At this time, most of the domains inside the ceramic are stabilized along the direction of the poling electric field, as shown in Fig. 4.13(c). When the direction of the applied electric field coincides with the direction of poling, the ferroelectric domains of the ceramics will be oriented along the electric field direction, resulting in large polarization intensity and electrostrain. At the same time, the defect dipoles are not easy to rotate and form a stable internal bias field to stabilize the domain structure, as shown in Fig. 4.13(d) and (e).

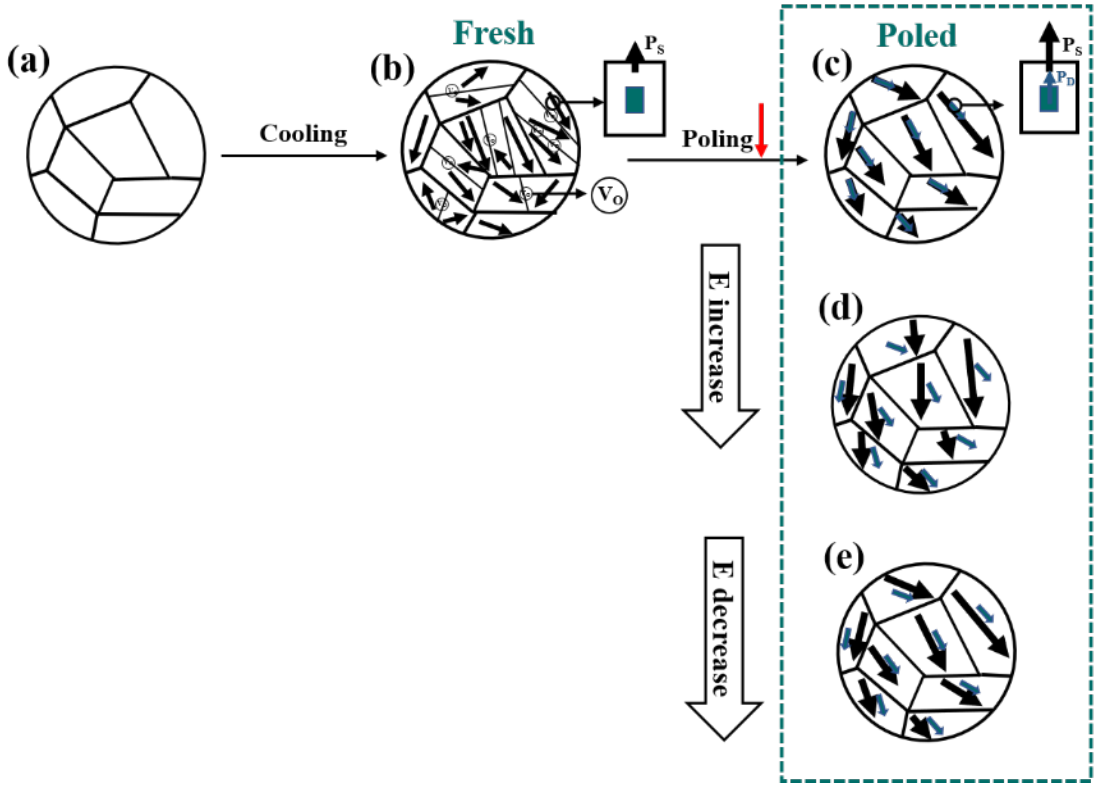


**Figure 4.13** Mechanism of the defect pinning for the BF-PT-BST based ceramics.

## 4.4 Conclusions

In summary, BF-PT-BST ceramics were prepared by a solid-state reaction method. The effects of the poling process, temperature, and electric field on the *P-E* loops and the *S-E* loops were studied. Combining the phase structure, dielectric, leakage current and thermally stimulated discharge current properties for the unpoled and poled ceramics, a qualitative model is developed to explain the pinning phenomenon of BF-PT-BST based piezoelectric ceramics. The main results are summarized below:

(1) For the 0.6BF-0.24PT-0.16BST ceramics, the poling process leads to the shifted and asymmetric *P-E* and *S-E* loops. Specifically, after poling, the maximum polarization $P_{max}$ and the remnant polarization $P_r$ of the ceramics increase significantly from 16.7 μC/cm$^2$ and 26.7 μC/cm$^2$ to 31.0 μC/cm$^2$ and 37.6 μC/cm$^2$, respectively. Also, the bipolar electrostrain (55 kV/cm) increased from 0.11 % to 0.39 %. These results are related to the formation of the defect dipole for the poled

ceramics. The defect dipoles are not easy to rotate and form a stable internal bias field $E_i$ to stabilize the domain structure.

(2) The reorientation of defect dipoles involves the migration of oxygen vacancies.

With increasing the temperature or decreasing the electric field frequency, the shape of *P-E* and *S-E* loops for the poled ceramics gradually changes from asymmetric to symmetric with a decrease of the internal electric field $E_i$. The reason is that the high temperature or low electric field frequency can facilitate the migration of oxygen vacancies, thus leading to the reorientation of defect dipoles.

(3) With the decrease of $BiFeO_3$ content, the difference in ferroelectric properties gradually disappeared and $E_i$ decreases for the unpoled and poled BF-PT-BST ceramics. For the poled BF-PT-xBST ceramics, $E_i$ gradually decreases, from 38.2 kV/cm at x=0.13 to 6.9 kV/cm at x=0.3. Also, the strain memory gradually decreases from 0.38 % at x=0.13 to 0.10 % at x=0.3. This may be related to the decrease of the concentration of charged defects for the ceramics with low $BiFeO_3$ content.

(4) The variation in the *P-E* loops with the temperatures is significantly different for the BF-PT-xBST ceramics with different BST doping contents. Thus, for low BST doping content, the values of $P_{max}$ and $P_r$ both increase with increasing temperature. While the value of $P_r$ decreases for the ceramics with high BST doping content. The significant increase of the strain with increasing temperature may be attributed to the decrease of the coercive field and the weakening of the domain wall pinning effect at high temperature.

# Chapter 5 Effect on electrical properties of Mn-doped 0.7BF-0.3PT ceramics

## 5.1 Introduction

The practical application of piezoelectric ceramics should not only consider their piezoelectric properties, but also focus on whether the material has a high resistivity and low leakage current. On the one hand, piezoelectrically induced charges will drain off before they are detected due to the high leakage current. On the other hand, a high conduction limits the poling effect for the ceramics. $BiFeO_3$-$PbTiO_3$ (BF-PT) based ceramics with the morphotropic phase boundary (MPB) show a high Curie temperature have been mentioned in the previous two chapters, which offers exciting opportunities as high-temperature piezoelectric ceramics. However, this system exhibits a large leakage current at high temperatures, which severely limits its normal operation as a piezoelectric device. Therefore, it is critical to reduce the leakage current of BF-PT based piezoelectric ceramics.

Cation substitution is an effective method to increase the resistivity of the BF-PT system. It was found that the resistivity of BF-PT based ceramics increased by three orders of magnitude from $10^9$ Ωcm to $10^{12}$ Ωcm by doping with $Ga^{3+}$, which was attributed to the suppression of Fe valence fluctuations and the reduction of oxygen vacancy concentration [108]. In addition to $Ga^{3+}$, the doping of $Ta^{5+}$, $Nb^{5+}$, and $La^{3+}$ is also beneficial for the preparation of dense and highly resistive BF-PT based piezoelectric ceramics [113]. According to the results of AC impedance spectroscopy, Ye et al. [114] concluded that the conduction mechanism of BF-PT based ceramics mainly comes from the hopping of electrons between $Fe^{2+}$ and $Fe^{3+}$, while the contribution of ion conduction is not significant. These studies generally attribute the high leakage current of the BF-PT system to factors such as the fluctuations of Fe valence state ($Fe^{3+}\rightarrow Fe^{2+}$) and the formation of oxygen vacancy. The third chapter of

this paper also reported that the high concentrations of $Fe^{2+}$ and oxygen vacancy can be observed in the samples with high leakage current by using XPS analysis. Meanwhile, Rojac et al. [172] used aberration-corrected scanning transmission electron microscopy (STEM) coupled with EELS analysis to show the accumulation of charged defects ($Fe^{4+}$ and Bi vacancy) at domain walls in BFO-based ceramics. The main mechanism of conductivity is p-type hopping conduction involving $Fe^{4+}(Fe_{Fe}^{\cdot})$ and $Fe^{3+}(Fe_{Fe}^{X})$. Similarly, density functional theory calculations also indicated that the p-type conduction of BFO is mainly related to the unoccupied gap state of $Fe^{4+}$ in an $FeO_5$ pyramid caused by the Bi vacancy [181]. Therefore, there are still some controversies about the mechanism of leakage conduction in the BFO-based ceramics.

On the other hand, it was reported that improved electrical properties (low leakage current) can be achieved in the Mn-doped BFO ceramics. In general, when oxygen vacancy exists in ceramic samples, Mn can act as a hole acceptor to reduce the oxygen vacancy concentration. Meanwhile, Mn and Fe at B-site can exhibit various valence states in the Mn-doped BFO ceramics to stabilize the perovskite structure [143, 182]. However, there is a lack of studies on the Mn-modified BF-PT system, especially the explanation of the leakage conduction mechanism of this system.

Based on the above research background, the chapter mainly systematically studied the structure and electrical properties of 0.7BF-0.3PT+xwt%$MnCO_3$ (x=0, 0.15, 0.3, 0.45) ceramic samples. First, the phase structure and the grain size of the ceramics were characterized by the XRD and SEM. Dielectric spectrum and AC impedance spectroscopy were used to study the abnormal dielectric relaxation phenomenon of the system. At the same time, the ferroelectric properties of different Mn-doped ceramic samples were analyzed. In particular, the leakage currents of different Mn-doped ceramic samples were fitted to derive the conduction mechanism. The valence state of Fe in the ceramics was analyzed by the Mössbauer spectrum, which corresponds to the conduction mechanism of the BF-PT system.

## 5.2 Experimental

0.7BF-0.3PT+xwt%$MnCO_3$ (x=0, 0.15, 0.3, 0.45) ferroelectric ceramics (abbreviated as BF-PT) were prepared by a solid state reaction method. The detailed preparation process is shown in Chapter 2 of this thesis. It should be pointed out that Mn is added to the ceramic powders as an additive, that is, a certain mass fraction of $MnCO_3$ is added to the calcined powders for the second ball milling process, and then sintered into a bulk ceramic.

## 5.3 Results

### 5.3.1 Phase and microstructure

Fig. 5.1 shows the XRD patterns of 0.7BF-0.3PT+xwt%$MnCO_3$ (x=0, 0.15, 0.3, 0.45) ceramic powders. The pure perovskite tetragonal (T) phase structure can be clearly observed in all ceramic samples. Detailed XRD profiles of diffraction lines in the 2θ range 46°-48° are also shown in Fig. 5.1, corresponding to the $(002)_T$ and $(200)_T$ peaks of the tetragonal phase. It can be seen that with the doping of Mn, the $(002)_T$ peak gradually moves to a higher angle, indicated the decrease of the lattice parameter *c*. Interestingly, the $(200)_T$ peak shifts first to a low angle and then to a high angle. That is, the $(200)_T$ peak of the sample with 0.15wt% Mn shifts to a low angle, but as increasing Mn content to 0.3 and 0.45 wt.%, the $(200)_T$ peak shifts to a higher angle. It indicates that with the increase of Mn content, the lattice parameter *a* of the ceramics increases first and then decreases. This result is also verified by the calculated lattice parameters of ceramics, as shown in Fig. 5.2. Since the radii of Mn ions are close to the radius of $Ti^{4+}$ ions and $Fe^{3+}$ ions at the B site ($r_{Mn}^{2+}$=0.67 Å, $r_{Mn}^{3+}$=0.65 Å, $r_{Mn}^{4+}$=0.53 Å, $r_{Fe}^{3+}$=0.65 Å, $r_{Ti}^{4+}$=0.61 Å) and smaller than the radius of $Bi^{3+}$ ions and $Pb^{2+}$ ions at the A site ($r_{Bi}^{3+}$=1.03 Å, $r_{Pb}^{2+}$=1.19 Å), so the doping of Mn ions should enter the lattice B-site for the BF-PT system. It is generally accepted that 2+, 3+ and 4+ valence states of Mn ions can exist in the Mn-doped BFO

ceramics, while the addition of Mn will lead to a change in the Fe valence state [182]. Therefore, the lattice parameter does not change monotonously, which may be related to the different ion radius caused by the change in the element valence.

On the other hand, it can be seen from Fig. 5.2 that all samples have a very large tetragonality *c/a*, and the pure 0.7BF-0.3PT ceramic has a *c/a* ratio as high as 1.18, which is much larger than the other reported perovskite-type ferroelectrics. This result is similar to those previously reported [99], where the (1-x)BF-xPT system has a very large tetragonal distortion at x = 0.27 to 0.31, which may be related to the partial covalent character of the Ti/Fe-O and Pb/Bi-O bonds in this system [93]. The doping of Mn only slightly changes the lattice parameters of the BF-PT system, and the doped ceramics still have very large tetragonal distortion.

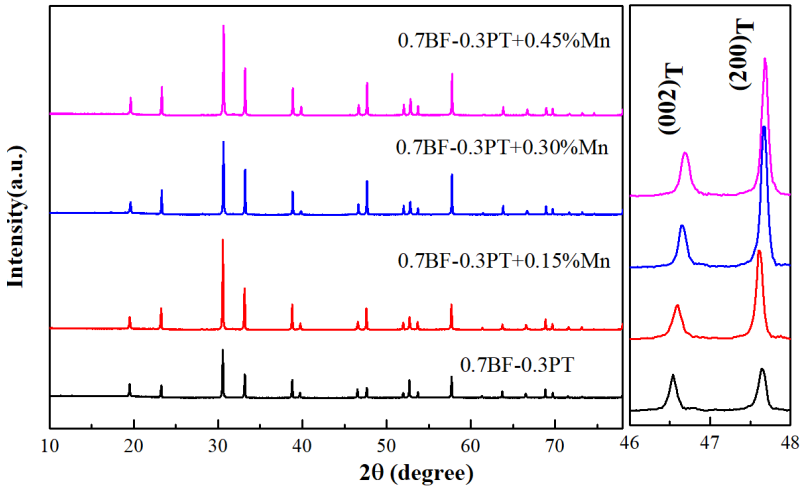


**Figure 5.1** XRD pattern of the 0.7BF-0.3PT+xwt%$MnCO_3$ (x=0, 0.15, 0.3, 0.45) ceramics.

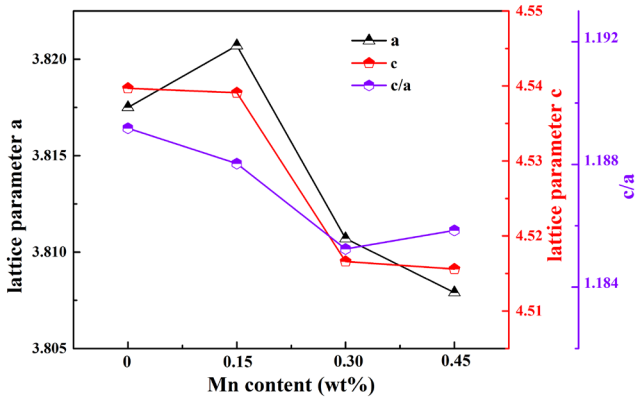


**Figure 5.2** Lattice parameters of 0.7BF-0.3PT+xwt%$MnCO_3$ (x=0, 0.15, 0.3, 0.45) ceramics.

Fig. 5.3 shows the SEM images of the fresh fracture surfaces for 0.7BF-0.3PT+xwt%$MnCO_3$ (x=0, 0.15, 0.3, 0.45) ceramics. A dense microstructure can be seen on the scanned surfaces. The grain size distributions are statistically calculated on SEM images by Imagej software for large numbers of grains. As shown in the inset of Fig. 5.3, there is no difference in the grain size for the samples with different Mn content. All the ceramics exhibit a small grain size of about 0.5 μm. This apparently small grain size is consistent with that reported in other BF-PT ceramics [91], which may be related to its large tetragonality. In addition, the energy-dispersive X-ray spectroscopy (EDS) analysis was used to get a clear view of the elemental distribution in the ceramic samples. Fig. 5.4 shows the EDS elemental mapping results of the 0.7BF-0.3PT+0.15wt%Mn ceramic samples. All the elements (Bi, Pb, Fe, O, Ti, Mn) are distributed homogeneously, indicating that there is no element aggregation phenomenon in the ceramics. Meanwhile, the measured atom percentage is close to the theoretical ones.

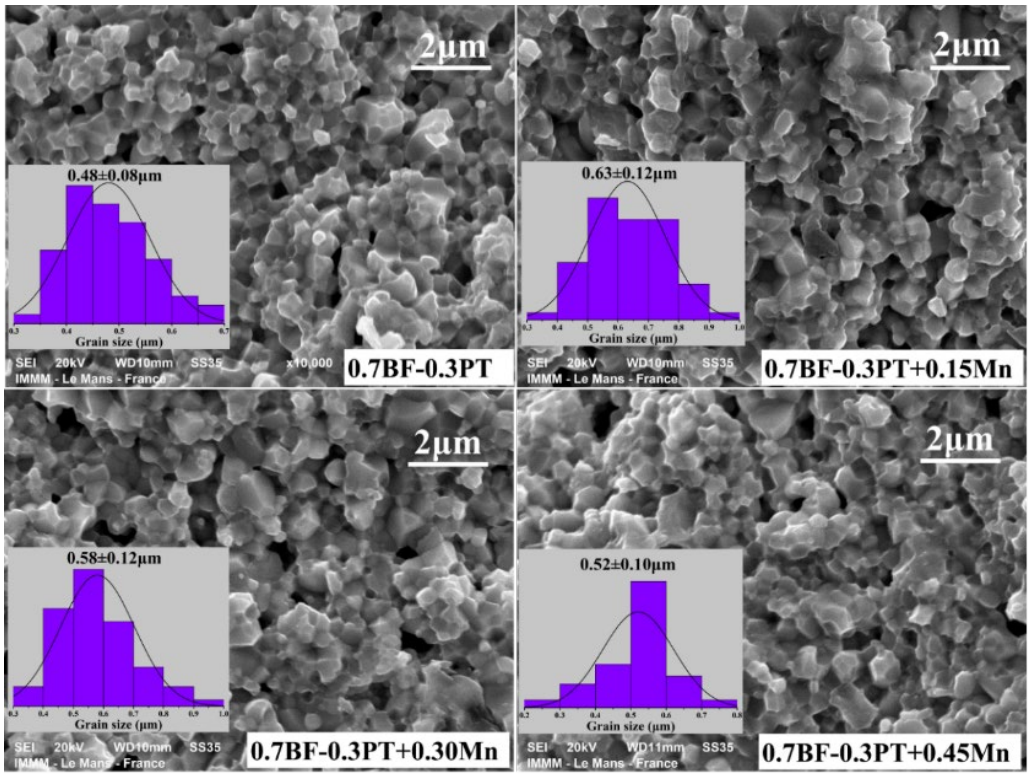


**Figure 5.3** SEM images of the fresh fracture surfaces of the 0.7BF-0.3PT+xwt%$MnCO_3$ (x=0, 0.15, 0.3, 0.45) ceramics.

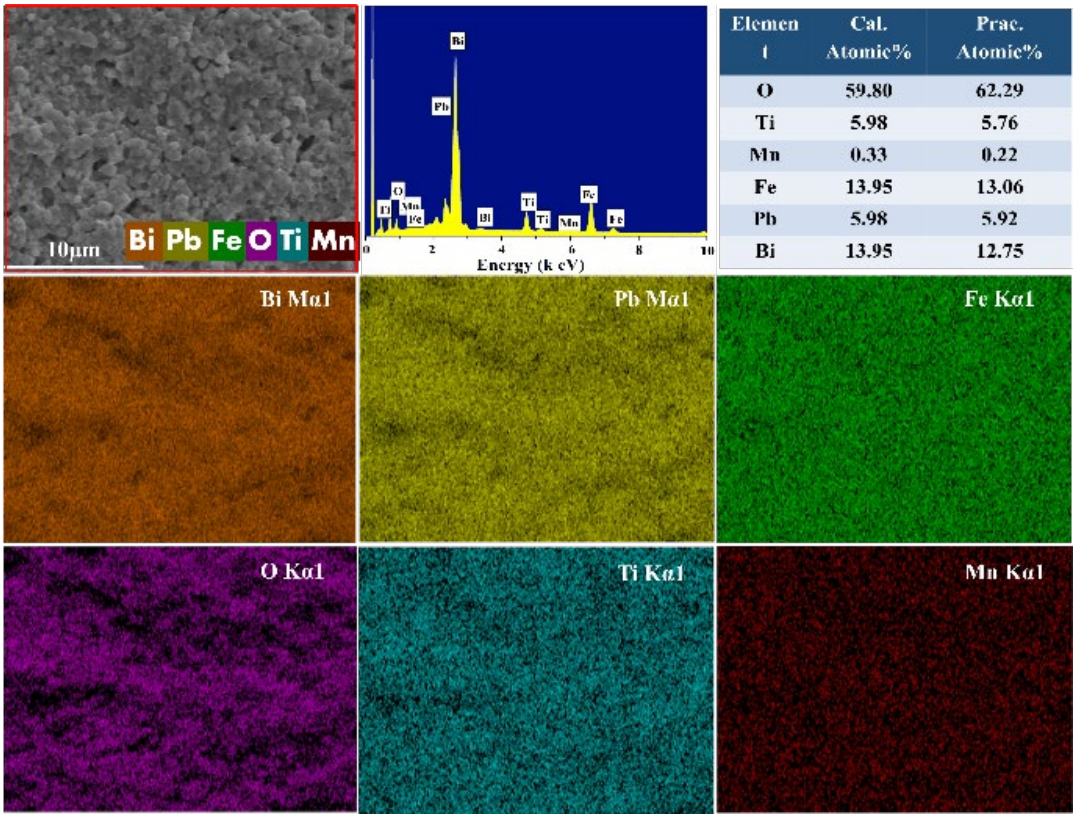


| Element | Cal. Atomic% | Prac. Atomic% |
|---|---|---|
| O | 59.80 | 62.29 |
| Ti | 5.98 | 5.76 |
| Mn | 0.33 | 0.22 |
| Fe | 13.95 | 13.06 |
| Pb | 5.98 | 5.92 |
| Bi | 13.95 | 12.75 |

**Figure 5.4** The element distribution of the sample and the surface SEM images of the 0.7BF-0.3PT+0.15wt%Mn ceramics.

## 5.3.2 Dielectric properties of ceramics

Fig. 5.5(a) shows the dielectric constant as a function of frequency for 0.7BF-0.3PT+xwt%$MnCO_3$ (x=0, 0.15, 0.3, 0.45) ceramics at room temperature. It can be seen that all the ceramics show the same variation, that is, as the frequency increases, the dielectric constant of ceramics decreases. Compared with the pure 0.7BF-0.3PT ceramic samples, the dielectric constant with frequency of the Mn-doped ceramics exhibits a flatter curve. Meanwhile, the dielectric constant of the pure 0.7BF-0.3PT ceramics is significantly higher than that of the Mn-doped ceramics, especially in the low frequency range. The dielectric constant decreases from 320 to 250 with the addition of Mn in the ceramics at the test frequency is 50 Hz. Fig. 5.5(b) shows the dielectric loss as a function of frequency for samples. Similar to the dielectric constant, the loss of the pure BF-PT ceramic at low frequency is significantly higher than that of the Mn-doped ceramic. In general, the

dielectric loss of ferroelectric ceramics involves the polarization loss and the conductive loss, while at low frequency it mainly originates from the contribution of leakage loss. Therefore, the pure BF-PT ceramics exhibit a large dielectric loss of more than 10 % at the frequency of 100 Hz, indicating the poor insulation and the large leakage current. The doping of Mn in BF-PT ceramics significantly reduces the dielectric loss, which is beneficial to the characterization of its ferroelectric properties. The leakage current of different ceramic samples will be analyzed in detail later.

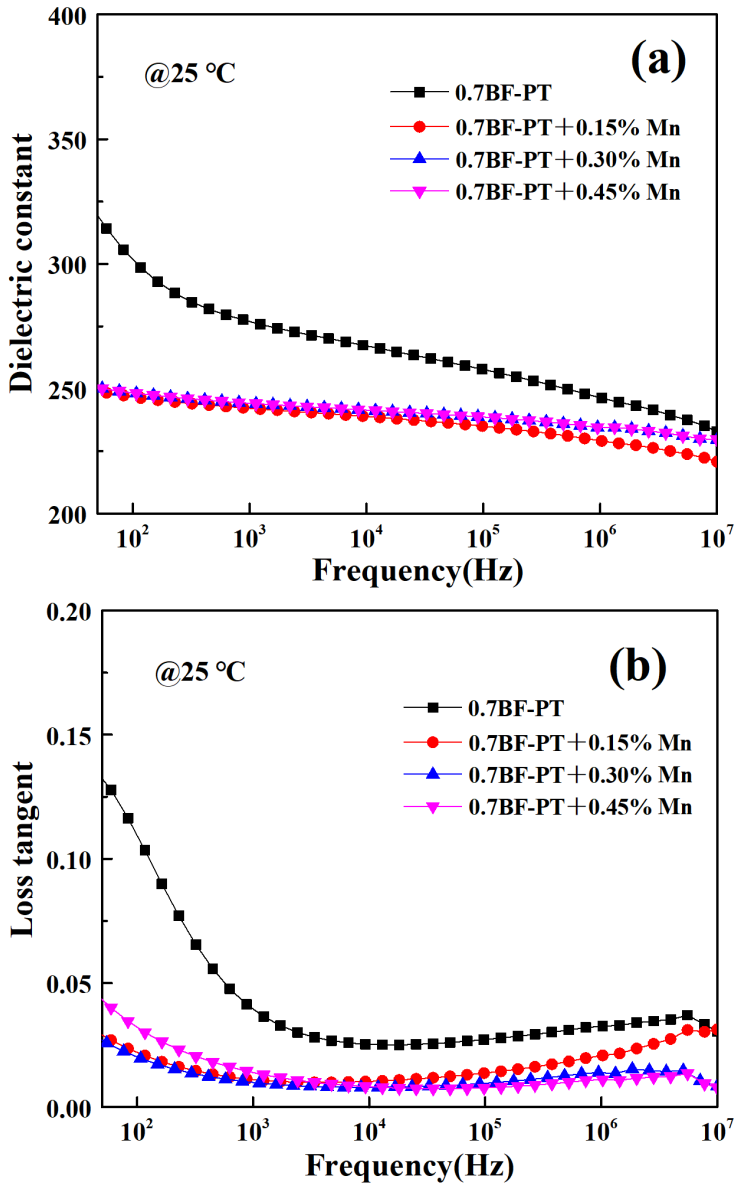


**Figure 5.5** The frequency dependencies of (a) $\varepsilon_r$; (b) tanδ at room temperature for the 0.7BF-0.3PT+xwt%$MnCO_3$ (x=0, 0.15, 0.3, 0.45) ceramics.

Fig. 5.6(a) shows the dielectric constant as a function of temperature for 0.7BF-0.3PT+xwt%$MnCO_3$ (x=0, 0.15, 0.3, 0.45) ceramics at the frequency of 1 MHz. There is a little difference of the Curie temperature for the samples with different compositions. This system exhibits a high Curie temperature, exceeding 600 °C, which is related to its large tetragonality. It should be noted that the dielectric-temperature curve of the pure BF-PT ceramic samples have a significant "lift" around 200 °C compared to the Mn-doped samples, indicating that the poor stability of the dielectric constant with temperature. This feature is not in favor of its application as a piezoelectric device in the high temperature environments. With the doping of Mn, the improved stability of the dielectric constant can be achieved in the samples. Fig. 5.6(b) shows the dielectric loss as a function of temperature for ceramic samples. It can be seen that there is a peak around 600 °C, corresponding to the phase transition. In addition, similar to the results from the dielectric-temperature curves, the pure BF-PT ceramics exhibit poor stability of the dielectric constant. As the temperature increases, the dielectric loss increases significantly, which is caused by the increase in thermally activated conductivity. To further investigate the anomalous plateau around 200 °C in the dielectric-temperature curves, the measurement on the temperature dependence of dielectric loss at different frequencies for the pure 0.7BF-0.3PT ceramics were carried out, as shown in Fig. 5.6(c). A relaxor-like dielectric anomaly in the temperature range of 30 °C-250 °C and the frequency range of 100 Hz-1 MHz can be observed from the inset. The loss peak shifts to higher temperature with increasing frequency, and the corresponding loss values gradually increase. This is a characteristic of thermally activated relaxation, which has been reported in many systems [183, 184]. It implies that the existence of a dielectric anomaly below the Curie temperature that is related to the thermally activated relaxation process, which is independent of the phase transition.

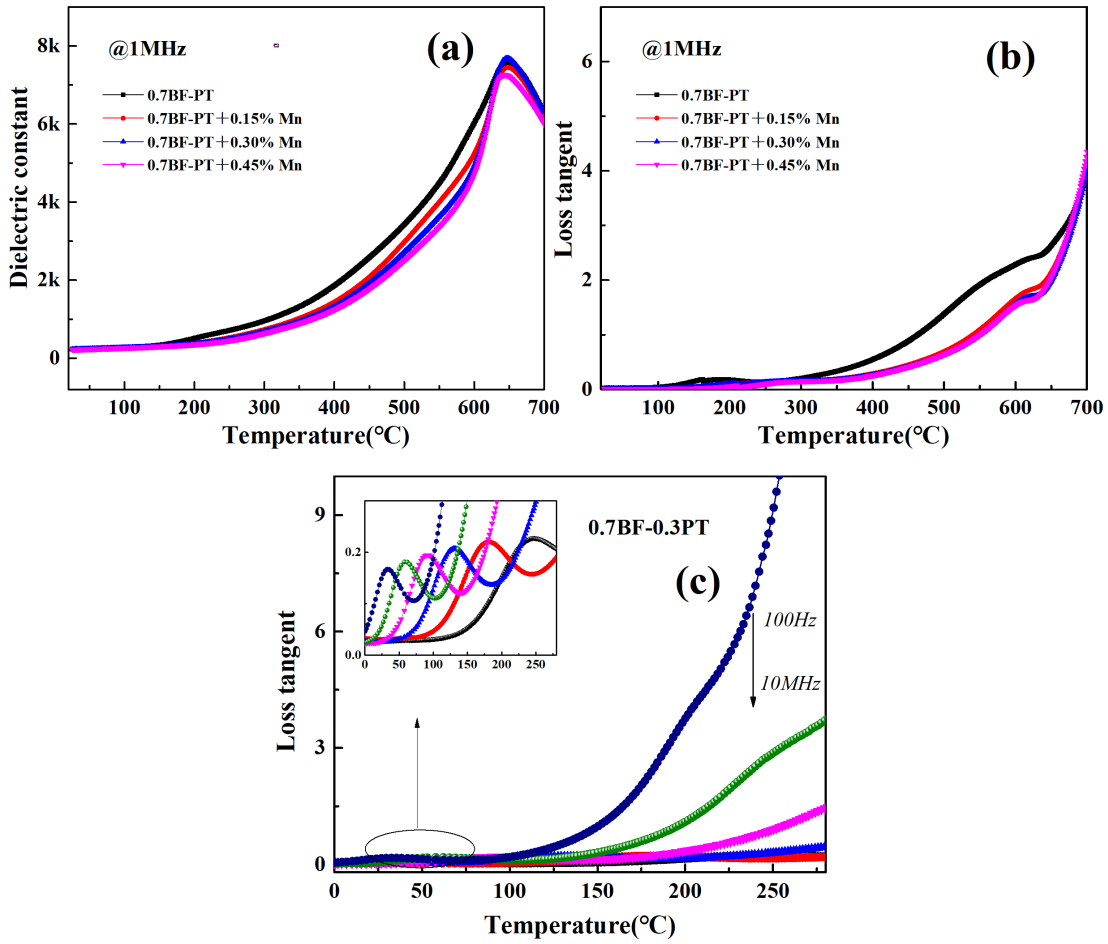


**Figure 5.6** (a)(b) The temperature dependencies of $\varepsilon_r$ and tanδ for the 0.7BF-0.3PT+xwt%$MnCO_3$ (x=0, 0.15, 0.3, 0.45) ceramics; (c) The temperature dependence of tanδ for the 0.7BF-0.3PT ceramics.

AC impedance spectroscopy is an effective method to study the phenomenon of dielectric relaxation in the ceramics, and the fitting activation can contribute to a better understanding of the relaxation mechanism. Fig. 5.7(a) shows the frequency dependency of dielectric loss at the different temperature for the 0.7BF-0.3PT ceramics, and the temperature range is 120 ℃-240 ℃. At a low frequency, the dielectric loss decreases monotonously with increasing frequency caused by the leakage conduction. As the frequency increases, a relaxation peak occurs in the relaxation zone. Also, it can be found that the peak shifts to a higher frequency as the temperature increases. It is well known that the dielectric relaxation at low frequencies is related to the space charge in the dielectric materials. The kind of

space charge can be confirmed by calculating the activation energy by Arrhenius' law, the formula is as follows:

$$f=f_0\exp(-E_{relax}/k_BT) \quad \ldots(5.1)$$

where $f$ is a characteristic frequency, $f_0$ is the pre-exponential factor, $k_B$ is the Boltzmann constant, and $E_{relax}$ is the activation energy for the relaxation. According to the linear fitting of $\ln(f)\sim1/T$ shown in Fig. 5.7(b), the calculated relaxation activation energy $E_a$ is 0.74 eV. In addition, Fig. 5.8(a) shows the frequency dependence of ac conductivity ($\sigma_{AC}$) for the 0.7BF-0.3PT ceramics. It can be found that the $\sigma_{AC}$ monotonously decreases as decreasing frequency and saturates to a constant value at a low frequency. The dc conductivity ($\sigma_{DC}$) can be obtained by extrapolating the ac conductivity curve at low frequencies. The $\sigma_{DC}$ as a function of temperature follows the Arrhenius law:

$$\sigma_{DC}=\sigma_0\exp(-E_{cond}/k_BT) \quad \ldots(5.2)$$

where the $E_{cond}$ is the activation energy for the conduction. From the linear fitting of $\ln(\sigma_{DC})\sim1/T$ shown in Fig. 5.8(b), the calculated conduction activation energy $E_{cond}$ is 0.92 eV. It is generally accepted that the relaxation mechanism is determined by a dipolar conduction process when the value of $E_{relax}$ is higher than that of $E_{cond}$. While if the relaxation is determined by a trap-controlled or hopping conduction, the value of $E_{relax}$ will be less than that of $E_{cond}$ [185, 186]. The sample with a higher value of conduction activation energy ($E_{relax}<E_{cond}$), indicating the relaxation should be related to the trap-controlled conduction. For the BF-PT system, the oxygen vacancy can be generated by the volatilization of $Bi_2O_3$ at the A-site, as shown in equations (5.3) and (5.4).

$$O_O^X \Leftrightarrow 1/2O_2 + 2e' + V_{\ddot{O}} \quad \ldots(5.3)$$

$$2Bi_{Bi}^X + 3O_O^X \Leftrightarrow 2V_{Bi}''' + 3V_{\ddot{O}} + Bi_2O_3(g) \quad \ldots(5.4)$$

$$V_O \Leftrightarrow V_{\dot{O}} + e' \quad \ldots(5.5)$$

$$V_{\dot{O}} \Leftrightarrow V_{\ddot{O}} + e' \quad \ldots(5.6)$$

Meanwhile, the ionization of the oxygen vacancy will create the conducting electrons, according to equations (5.5) and (5.6). The activation energy of electron

hopping (<0.3 eV), single-ionized oxygen vacancies (0.3-0.5 eV) and doubly-ionized oxygen vacancies (0.6-1.2 eV) can be obtained in previous reports. Depending on the value of activation energy, doubly-ionized oxygen vacancies are considered to be responsible for the dielectric relaxation in the BF-PT system. It can be concluded that the dielectric relaxation behaviors are attributed to the short-range hopping of the oxygen vacancies, while the long-range motion of doubly-ionized oxygen vacancies causes the conduction. The same relaxation behaviors have been reported in other systems [183-185].

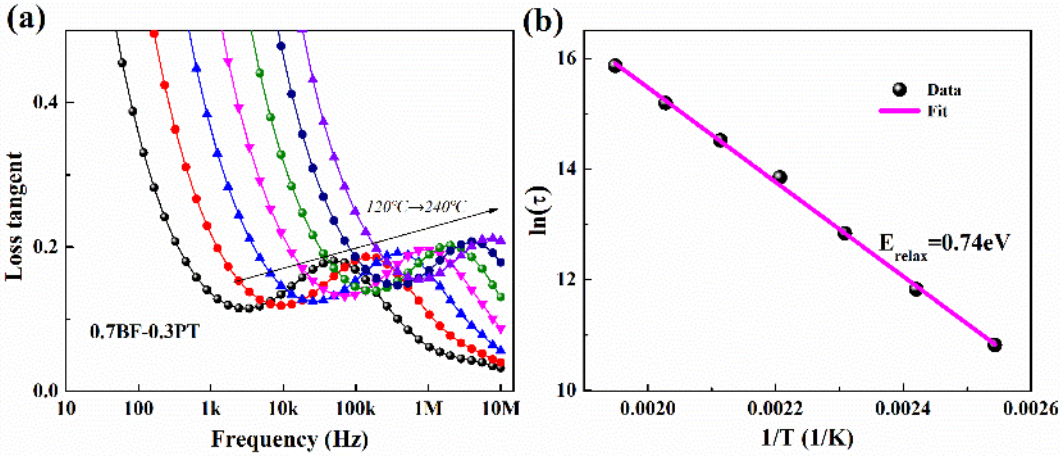


**Figure 5.7** (a) The frequency dependency of tanδ at the different temperature for the 0.7BF-0.3PT ceramics; (b) Arrhenius plot of the tanδ.

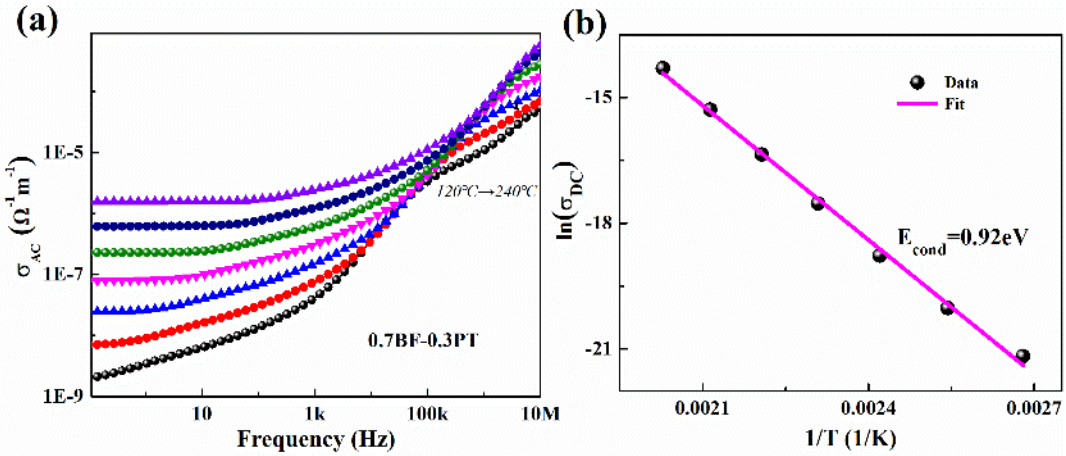


**Figure 5.8** (a) The frequency dependency of ac conductivity at the different temperature for the 0.7BF-0.3PT ceramics; (b) Arrhenius plot of the dc conductivity.

## 5.5.3 Ferroelectric properties of ceramics

Fig. 5.9(a) shows the hysteresis *P-E* loops of 0.7BF-0.3PT+xwt%$MnCO_3$ (x=0, 0.15, 0.3, 0.45) ceramics. It can be seen that even with an applied electric field of up to 130 kV/cm, the hysteresis *P-E* loops of all ceramic samples are still not fully opened. The values of remnant polarization $P_r$ and coercive field $E_c$ for the ceramic samples are shown in Fig. 5.9(b). $E_c$ for pure 0.7BF-0.3PT ceramics is as high as 56 kV/cm, which is much higher than that of other ferroelectric ceramics. It was reported that a large tetragonality *c/a* didn't favor the rotation of domains, which will lead to a large $E_c$. Therefore, it can be concluded that the large $E_c$ of the BF-PT system is related to its large tetragonality, which makes it difficult to accurately characterize the ferroelectric properties of ceramics. With the addition of Mn, the field $E_c$ of the ceramics decreases slightly, but still has a very large value (>40 kV/cm). In addition, the $P_r$ of the ceramics gradually decreases, from 8.6 μC/cm$^2$ for the undoped sample to 3.7 μC/cm$^2$ for the ceramics doped with 0.45 wt.% Mn.

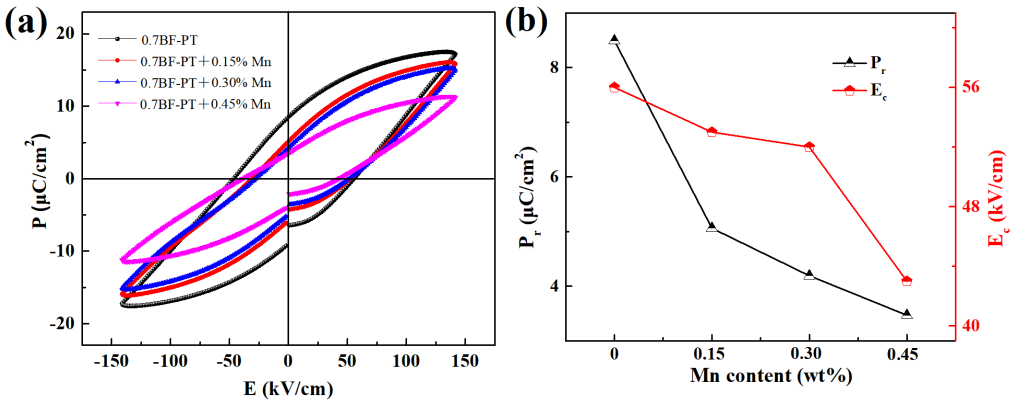


**Figure 5.9** (a) The *P-E* loops of 0.7BF-0.3PT+xwt%$MnCO_3$ (x=0, 0.15, 0.3, 0.45) ceramics; (b) $P_r$ and $E_c$ as a function of Mn content.

## 5.3.4 Leakage conduction of ceramics

Fig. 5.10(a) shows the unipolar leakage current of the 0.7BF-0.3PT+xwt%$MnCO_3$ (x=0, 0.15, 0.3, 0.45) ceramics at room temperature. As the electric field increases, the leakage current density of all ceramic samples gradually increases. In particular, compared with the Mn-doped samples, the leakage

current density of the pure 0.7BF-0.3PT ceramics increases sharply with the electric field. When the electric field is 75 kV/cm, the leakage current density is as high as 12 μA/cm$^2$. With the addition of Mn, the leakage current density of the ceramics first decreases and then increases. When the Mn doping content is 0.15 wt.%, the ceramics exhibit the lowest leakage current density (0.25 μA/cm$^2$ at 75 kV/cm), which is two orders of magnitude less than that of the pure 0.7BF-0.3PT ceramics and also significantly lower than that of the previously reported BFO-based ceramics [175, 176]. On the contrary, the leakage current density of ceramics with high Mn content increases, which may imply that the different leakage current mechanisms can be found in the ceramics with different Mn contents. The leakage currents at different temperatures for the 0.7BF-0.3PT ceramics are shown in Fig. 5.10(b). It can be seen that the leakage current density of the ceramics increases significantly with the temperature, indicating the high leakage conduction at high temperature, which is consistent with the increase in a dielectric loss at high temperature.

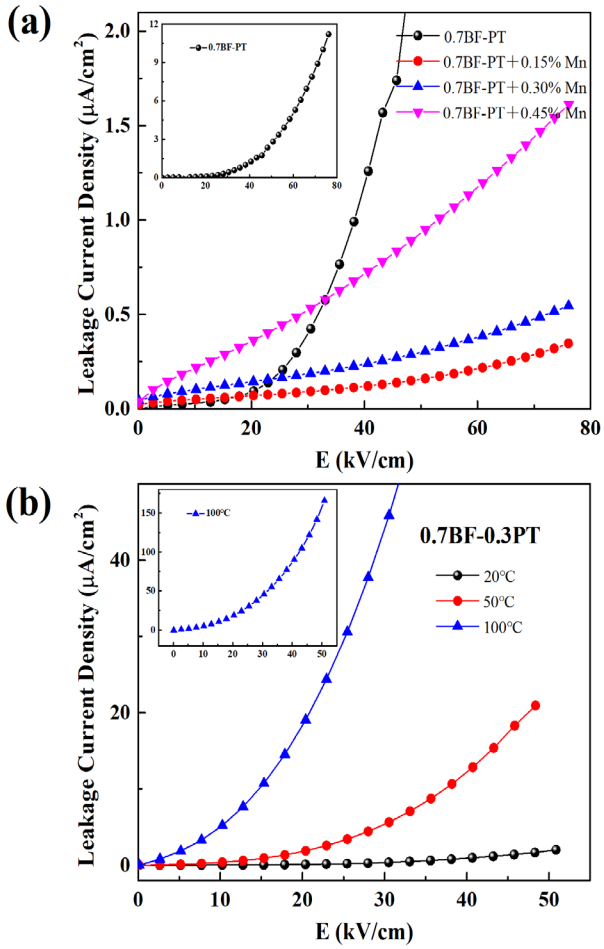


**Figure 5.10** (a) The unipolar leakage current of the 0.7BF-0.3PT+xwt%$MnCO_3$ (x=0, 0.15, 0.3, 0.45) ceramics; (b) The leakage current at different temperatures for the 0.7BF-0.3PT ceramics.

To investigate the leakage conduction mechanism of the BF-PT system, the log*J*~log*E* curves of ceramic samples are shown in Fig. 5.11. Firstly, for the pure 0.7BF-0.3PT ceramics, the slop at low electric field is 2.05, corresponding to the space charge limited current (SCLC) mechanism. In this case, the leakage current density and electric described by the formula:

$$J=9\mu\varepsilon_0\varepsilon_r E^2/8d \qquad \ldots(5.7)$$

where $\varepsilon_0$ is the dielectric constant of free space, $\varepsilon_r$ is the dielectric constant, $\mu$ is the carrier mobility, and $d$ is the thickness. Meanwhile, the slop at high electric field is 3.81, indicating the trap filled limited current (TFL) mechanism [187, 188]. For ceramics doped with low contents Mn (x=0.15, 0.3), the slopes at low electric fields

are 0.82, 0.86, respectively, as shown in Fig. 5.11(b) and (c), corresponding to the Ohmic conduction. As the electric field increases, SCLC conduction is dominant for the ceramics with the composition of x=0.15, 0.3. The addition of Mn leads to a change in the leakage conduction mechanism of the BF-PT system, which may be related to the concentration of traps, i.e. oxygen vacancies in the ceramics. It was reported that Mn can act as a hole acceptor to reduce the oxygen vacancy concentration in BFO-based ceramics [182, 189]. In the present work, with the trace doping of Mn, the concentration of oxygen vacancies is reduced and the leakage conduction mechanism is changed, which results in a significant decrease in leakage current. In addition, the ceramics with the composition of x=0.45 exhibit Ohmic conduction behavior during the whole measurement region, which may be related to the fact that the high content of Mn doping changes the valence state of the B-site ions and generates more free carriers. The leakage conduction mechanisms of the investigated ceramics are shown in Table 5.1.

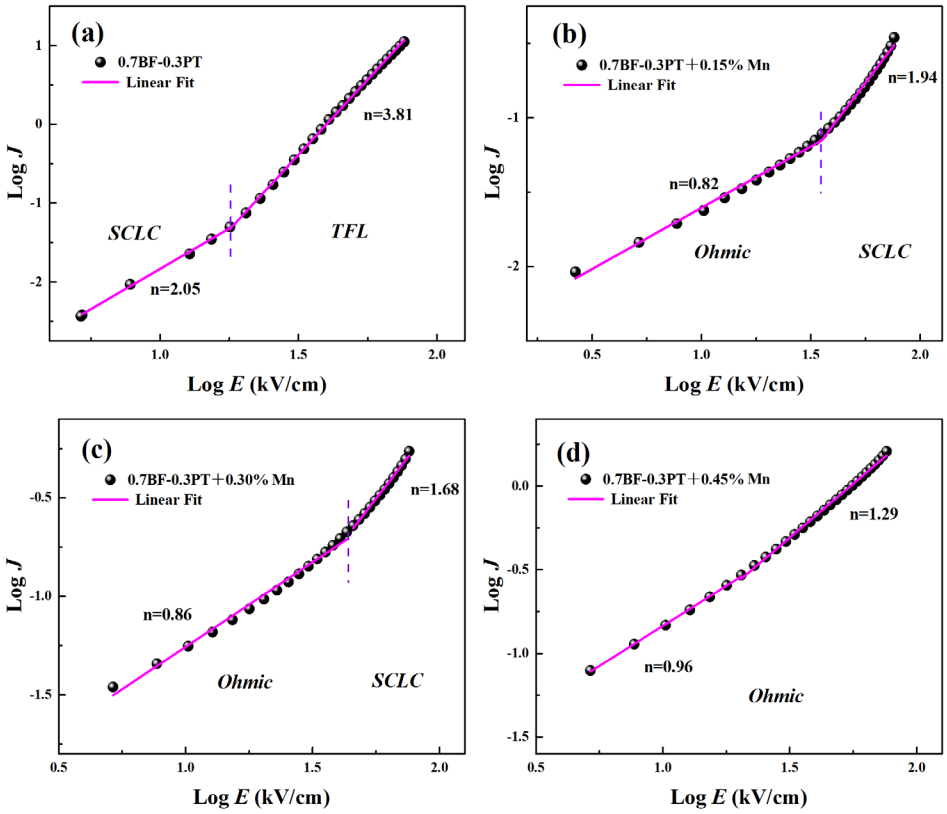


**Figure 5.11** Plots of log$J$ vs. log$E$ for the 0.7BF-0.3PT+xwt%$MnCO_3$ (x=0, 0.15, 0.3, 0.45) ceramics.

**Table 5.1** The leakage mechanism of the 0.7BF-0.3PT+xwt%$MnCO_3$ (x=0, 0.15, 0.3, 0.45) ceramics.

| Composition | Leakage mechanism | |
|---|---|---|
| | Low field | High field |
| 0.7$BiFeO_3$-0.3$PbTiO_3$ | SCLC | TFL |
| 0.7$BiFeO_3$-0.3$PbTiO_3$+0.15wt%Mn | Ohmic | SCLC |
| 0.7$BiFeO_3$-0.3$PbTiO_3$+0.30wt%Mn | Ohmic | SCLC |
| 0.7$BiFeO_3$-0.3$PbTiO_3$+0.45wt%Mn | Ohmic | |

## 5.3.5 $^{57}$Fe Mössbauer probing of Fe

$^{57}$Fe Mössbauer spectrum is sensitive to the chemical valence and surrounding fine structure of Fe, which provides information about the electronic density of the nuclei (isomer shift, IS), the electric field gradient (quadrupole splitting, QS) and the magnetic environment (magnetic hyperfine splitting, HF). For $BiFeO_3$-based ceramics, the Mössbauer spectrum can clearly reflect the various valence states of Fe ions ($Fe^{2+}$, $Fe^{3+}$ and $Fe^{4+}$), which is very helpful for analyzing the role of Fe in the BF-PT system. Fig. 5.12 shows the Mössbauer spectrum of 0.7BF-0.3PT+xwt%$MnCO_3$ (x=0, 0.15, 0.3, 0.45) ceramics. It can be seen that Mössbauer spectrum of the ceramics can be fitted with the Zeeman sextets and the paramagnetic doublet. Due to the presence of at least two sites of Fe in the binary perovskite compound, multiple Zeeman sextets can be found in the Mössbauer spectrum, corresponding to different HF. Similar results have also been reported in other BFO-based ceramics [190, 191]. Table 5.2 shows the mean refined values of hyperfine parameters obtained from Mössbauer spectrum. Generally, the valence state of Fe can be determined by the isomer shift IS values. For the ceramics with composition of x=0, 0.15, 0.3, the IS values are about 0.24-0.54 mm/s, corresponding to the $Fe^{3+}$ ions [190]. The dominancy of $Fe^{3+}$ oxidation state can be obtained in the ceramics doped with low Mn content. When the Mn doping content is 0.45 wt%, three values of the IS appeared: 0.06 mm/s, 0.39 mm/s, and 1.23 mm/s,

corresponding to $Fe^{4+}$, $Fe^{3+}$, and $Fe^{2+}$ ions, respectively [190, 192], and with relative contents of 48 %, 37 %, and 15 %. This result indicates that the excessive Mn doping leads to the partial reduction and partial oxidation of $Fe^{3+}$ ions in the ceramics. It is generally believed that in Mn-doped $BiFeO_3$-based ceramics, Mn can act as a hole acceptor to reduce the oxygen vacancy concentration, on the other hand, Mn and Fe ions can exhibit different valence states to balance the charges [182]. Combined with the previous analysis of the leakage conduction, it can be speculated that the high oxygen vacancy concentration rather than the fluctuations of Fe valence, causes a large leakage current in the pure BF-PT ceramics. With the addition of Mn which acts as a hole acceptor, it suppresses the formation of the oxygen vacancy, which leads to a low leakage current density for ceramics. When the content of Mn continues to increase, the valence of Mn and Fe will be changed in order to balance the charge in the ceramics. As a result, more free carriers are generated in the materials, which increases its leakage current.

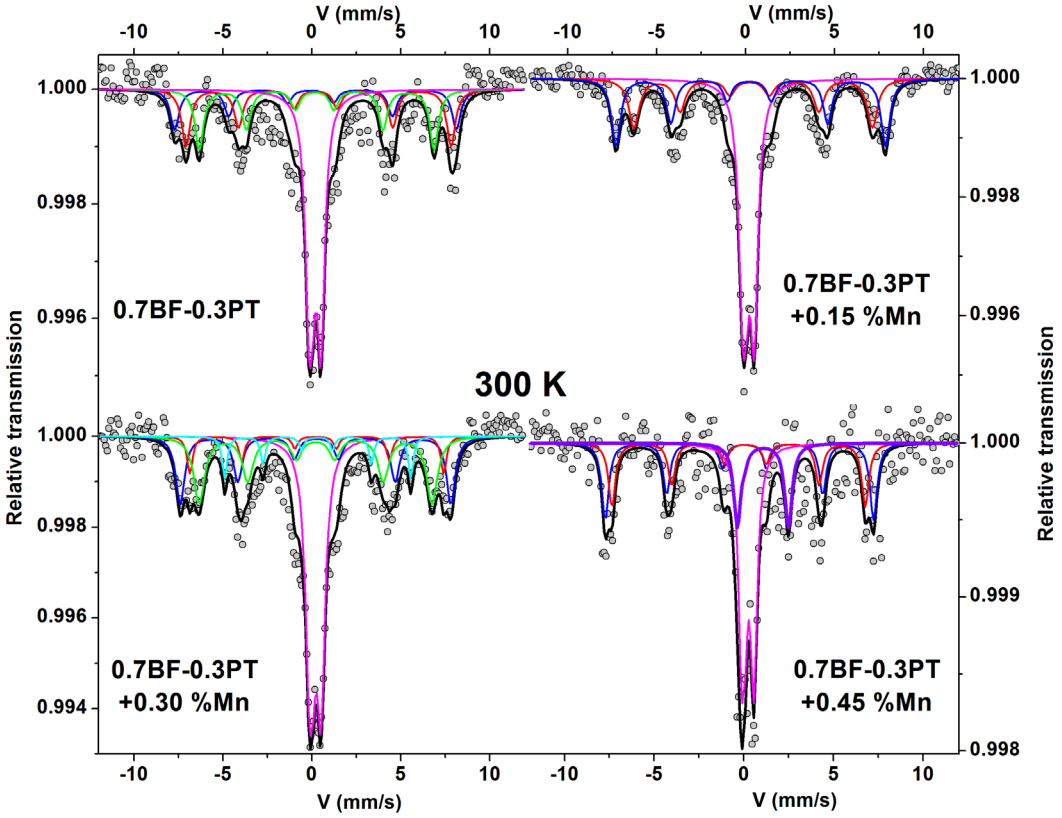


**Figure 5.12** Mössbauer spectrum of 0.7BF-0.3PT+xwt%$MnCO_3$ (x=0, 0.15, 0.3, 0.45) ceramics.

**Table 5.2** Mean refined values of hyperfine parameters obtained from Mössbauer spectrum of 0.7BF-0.3PT+xwt%$MnCO_3$ (x=0, 0.15, 0.3, 0.45) ceramics.

| Sample | Site | IS (mm/s) | QS (mm/s) | HF (Tesla) | Area (%) |
|---|---|---|---|---|---|
| x=0 | Sextet 1 | 0.24 | 0.28 | 48.9 | 15 |
| | Sextet 2 | 0.46 | 0.16 | 46.0 | 22 |
| | Sextet 3 | 0.38 | 0.10 | 40.7 | 23 |
| | Doublet | 0.35 | 0.56 | - | 40 |
| x=0.15 | Sextet 1 | 0.40 | 0.08 | 46.8 | 30 |
| | Sextet 2 | 0.45 | 0.20 | 41.4 | 25 |
| | Doublet | 0.34 | 0.53 | - | 45 |
| x=0.30 | Sextet 1 | 0.40 | -0.05 | 47.0 | 22 |
| | Sextet 2 | 0.41 | 0.07 | 44.1 | 8 |
| | Sextet 3 | 0.37 | 0.01 | 40.4 | 26 |
| | Sextet 4 | 0.47 | 0.03 | 32.2 | 7 |
| | Doublet | 0.35 | 0.54 | - | 37 |
| x=0.45 | Sextet 1 | 0.06 | -0.29 | 46.2 | 26 |
| | Sextet 2 | 0.06 | -0.37 | 43.6 | 22 |
| | Doublet 1 | 0.39 | 0.56 | - | 37 |
| | Doublet 2 | 1.23 | 2.75 | - | 15 |

## 5.4 Conclusions

In summary, 0.7BF-0.3PT+xwt%$MnCO_3$ (x=0, 0.15, 0.3, 0.45) ceramics were prepared by a solid-state reaction method, and the structure and the electrical properties were studied. Mössbauer spectrum was used to determine the valence state of Fe. The main results are summarized below:

(1) All the ceramic samples exhibit the pure perovskite tetragonal (T) phase with a large tetragonality *c/a*. The lattice parameter does not change monotonously with the Mn content increases, which may be related to the different ion radius

caused by the change in the element valence. Meanwhile, a dense and homogeneous microstructure can be obtained in the ceramics.

(2) This system exhibits a high Curie temperature, exceeding 600 ℃, which is related to its large tetragonality. The dielectric loss-temperature curve of pure 0.7BF-0.3PT ceramics shows a relaxation peak in the temperature range of 30-250 ℃ and the frequency range of 100 Hz-1 MHz. The calculated activation energy ($E_{relax}$~0.74 eV, $E_{cond}$~0.92 eV) shows that the relaxation peak is related to the doubly-ionized oxygen vacancies. In addition, the large coercive field $E_c$ can be observed in the BF-PT system, which makes it difficult to accurately characterize the ferroelectric properties of ceramics.

(3) The pure 0.7BF-0.3PT ceramics show a large leakage current density of about 12 μA/cm$^2$. With the addition of Mn, the leakage current density of the ceramics first decreases and then increases. When the Mn doping content is 0.15 wt.%, the ceramics exhibit the lowest leakage current density (0.25 μA/cm$^2$ at 75 kV/cm), which is two orders of magnitude less than that of the pure 0.7BF-0.3PT ceramics and also significantly lower than that of the previously reported BFO-based ceramics. It was found that the ceramics with high Mn content (x=0.45) exhibit Ohmic conduction behavior during the whole measurement region, which is different from space charge limited current conduction of other compositions.

(4) Mössbauer spectrum of all the ceramics can be fitted with the Zeeman sextets and the paramagnetic doublet, indicating the presence of at least two sites of Fe. In addition, the valence state of Fe is determined by the isomer shift IS values. The dominancy of $Fe^{3+}$ oxidation state can be obtained in the ceramics doped with low Mn content (x=0, 0.15, 0.3). However, there are multivalent Fe ions ($Fe^{2+}$, $Fe^{3+}$ and $Fe^{4+}$) in the ceramics doped with high Mn content (x=0.45). This result is consistent with the analysis of leakage conduction of ceramics.

# Chapter 6 Enhanced energy storage properties of lead-free BF-BT based ceramics by grain-size reduction

## 6.1 Introduction

In recent decades, particular attentions have been drawn for the ferroelectric capacitors, which have been widely investigated as promising candidates for energy storage devices because of their high energy density and fast charge-discharge capabilities [124-126]. Generally, the energy density of ferroelectric materials mainly derives from the switching of the reversible domain under an electric field, which is calculated by the following equation:

$$W_{re} = \int_{P_r}^{P_{max}} EdP \quad \ldots (6.1)$$

where $W_{re}$ represents the recoverable energy density, $P_{max}$ and $P_r$ represent the maximum polarization at the electric field and the remanent polarization. Hence, in order to design relevant ferroelectric structures with a high recoverable energy density, the main requirement lies in a large polarization difference $\Delta P$ ($\Delta P = P_{max} - P_r$) along with a high dielectric breakdown strength ($E_b$). In this context, several doped ferroelectric ceramics were designed to ensure a low remanent polarization [131, 193-195]. Among them, increasing the local compositional disorder in the underlying structures by introducing non-isovalent cations into the perovskite $ABO_3$ ferroelectric ceramics, represents potentially the most effective ways [131]. As a consequence, a low remanent polarization occurs due to the dynamic of polar nanoregions (PNRs) involved in relaxor ferroelectrics [195].

In close relation with the targeted properties, the grain size plays a crucial role in the domain configuration and electrical properties of ferroelectric ceramics. Several developments were carried out to analyze the grain size effects on ferroelectric and dielectric properties of the polycrystalline ferroelectrics. As an

example, it has been reported that $BaTiO_3$ ceramics with an intermediate grain size near 1μm show a maximum dielectric constant and piezoelectric coefficient [196]. The domain wall effects were reported to be the origin of the large dielectric constant in the fine-grained $BaTiO_3$ ceramics. Besides, Arlt et al. [197] have revealed that the domain width of ferroelectric ceramics decreases with the decrease of grain size. Recently, it was reported that the domain size decreases from 700 nm to 70nm by decreasing the grain size from 5.4μm to 0.15μm in the KNN-based ceramics [198]. The above results point out that the decrease of grain size ensures the formation of nanosized domains in ferroelectric ceramics.

As a drastic evolution can be expected for the energy storage properties, the present contribution is devoted to an exhaustive analysis of the recoverable energy storage density in ferroelectric ceramics with fine grains. The chosen systems are based on the lead-free $BiFeO_3$-$BaTiO_3$ (BF-BT) ferroelectric ceramics and consist in $BiFeO_3$-$BaTiO_3$-$Bi(Mg_{2/3}Nb_{1/3})O_3$ (BFBT-BMN) ternary ceramics. The scheme of this study is presented in Fig. 6.1. Two representative samples were prepared by a conventional solid-state reaction method and using a high-energy ball milling to obtain fine-grinded ceramics where the nanosized ferroelectric domains are expected to hold. A comparative study between the fine-grinded BFBT-BMN ceramics and the coarse-grained ones was performed along with an in-depth analysis of the microstructure effects on the energy storage properties.

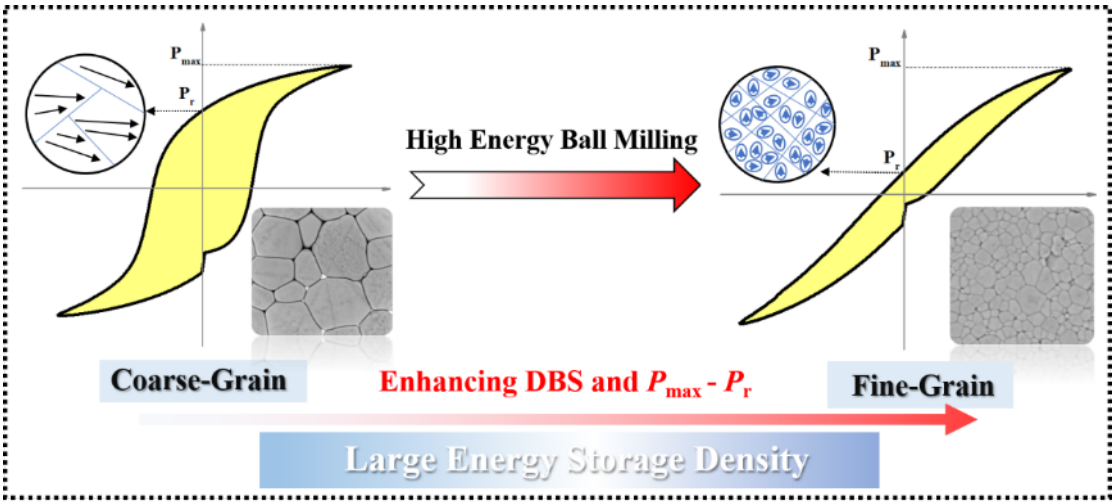


**Figure 6.1** A sketch of the design for this section.

# 6.2 Experimental

$(0.67\text{-}x)BiFeO_3\text{-}0.33BaTiO_3\text{-}xBi(Mg_{2/3}Nb_{1/3})O_3$ (x=0.02, 0.06) ceramics prepared by a solid-state reaction method. The detailed preparation process is shown in Chapter 2 of this thesis. For the coarse-grained ceramics, the calcined powders were ball milled again by the planetary ball milling for 6 h. While for the fine-grained ceramics, the calcined powders were re-milled by a high-energy ball milling process for 2 h (Retsch 20.510.0001 High Energy Ball Mill Emax 200-240V, Germany). The piezo-response force microscope (SPA 400, SPI3800N, Seiko Inc. Japan) and transmission electron microscopy (JEOL ARM200F) were used for the investigation of the domain structures in the ferroelectric ceramics.

# 6.3 Results

## 6.3.1 Phase and microstructure

Fig. 6.2 shows the XRD patterns of the BFBT-xBMN (x=0.02,0.06) ceramics. All the ceramic samples show a pure perovskite structure with no secondary phases. Locally magnified XRD profiles of (200) diffraction lines in the 2θ range 44°-46° are also shown in Fig. 6.2. All the peaks are non-split, suggesting the pseudo-cubic (PC) symmetry for the BFBT-xBMN ceramics. With the increase of BMN content, the diffraction peak moves to a higher angle, indicating that the unit cell volume becomes smaller. This may be explained by the replacement of the small cations at B-site. In addition, even for the ceramics with the same composition, the (200) diffraction peaks are found to shift to higher angles, suggesting a slight lattice shrinkage for the samples prepared by high-energy ball milling. It is known that the changes in grain size will affect the internal stresses and the lattice parameters of ceramics [199]. Therefore, this result implies that the difference of microstructure for the ceramics prepared by the different ball mill processes.

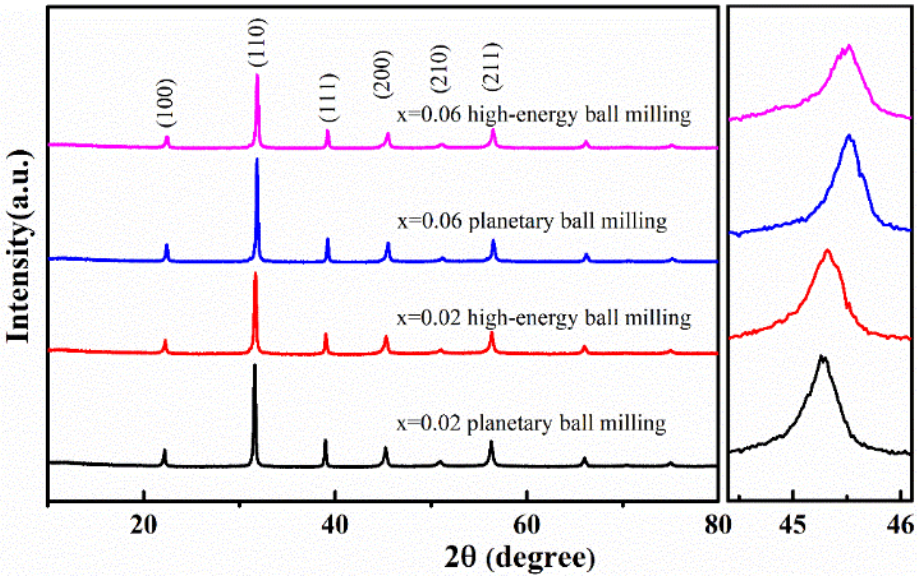


**Figure 6.2** XRD patterns of BFBT-xBMN (x=0.02, 0.06) ceramics.

Fig. 6.3 shows the SEM micrographs of fractured surfaces of the BFBT-xBMN (x=0.02,0.06) ceramics. A dense microstructure can be seen along with few pores distributed on the scanned surfaces. Both fine- and coarse-grained ceramics show a high relative density. The grain size distributions are statistically calculated on SEM images by Imagej software for large numbers of grains. As shown in Fig. 6.4, after using the high-energy ball milling process, the average grain size decreases from 2.86±0.38 to 0.55±0.17 μm for the BFBT-0.02BMN ceramics while the reduction if from 4.1±0.52 to 0.89±0.21 μm for the BFBT-0.06BMN ceramics. Thus, the high-energy ball milling process reduces the average grain size by 80% in the considered ceramics. Moreover, the grain size reduction would inevitably modify the boundary conditions in the host ceramics and leads to changes in the electrical and mechanical features, which in turn alter the dielectric and ferroelectric properties of ceramics [141].

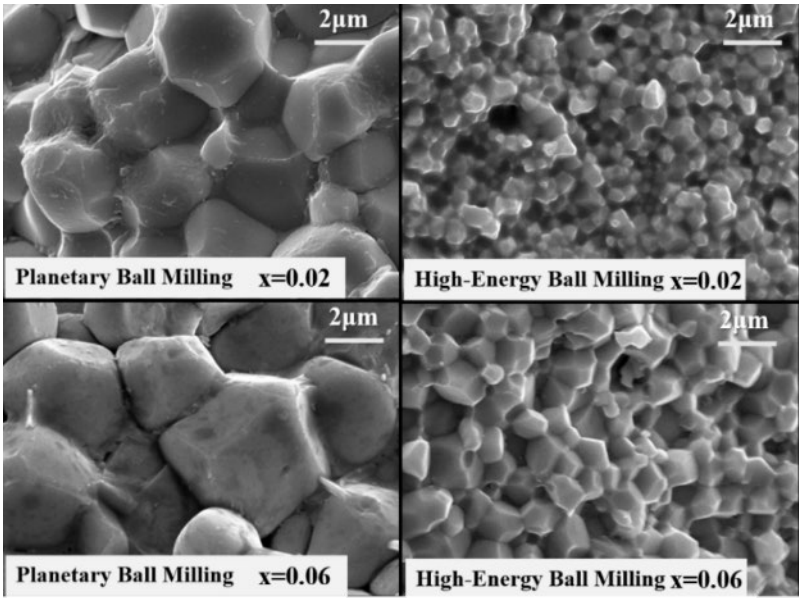


**Figure 6.3** SEM micrographs of fractured surfaces obtained from BFBT-xBMN (x=0.02, 0.06) ceramics.

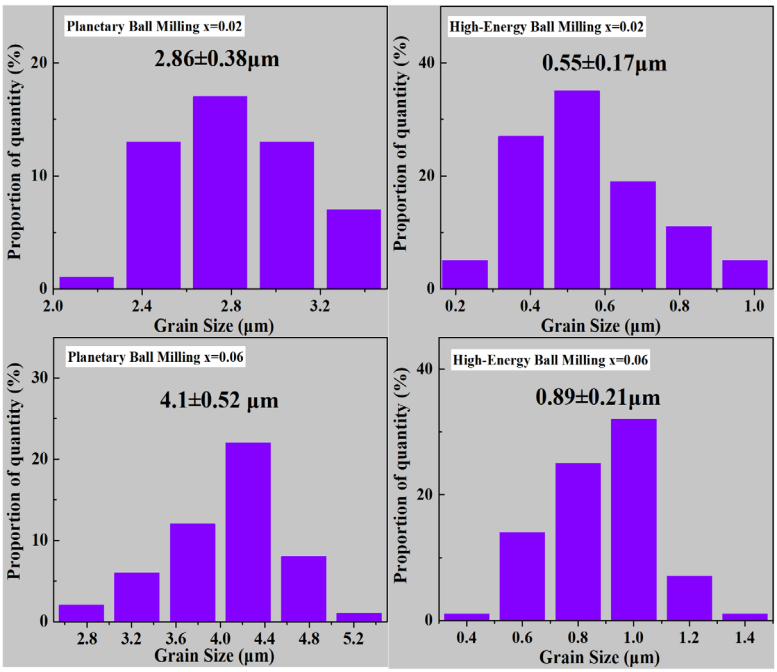


**Figure 6.4** Grain size distributions of BFBT-xBMN (x=0.02, 0.06) ceramics.

## 6.3.2 Dielectric properties

The temperature and frequency dependence of dielectric constant and loss tangent of BFBT-xBMN (x=0.02,0.06) ceramics with different grain sizes are shown

in Fig. 6.5. All the BFBT-BMN ceramics exhibit a diffuse phase transition along with strong frequency dispersion. The drastic increase of the loss tangent at high temperatures results from the enhanced contribution from the thermally activated conductivity. According to previous studies, the coarse-grained BFBT-BMN ceramics show the nonergodic relaxor characteristics [200]. As summarized in Table 6.1, when the grain size decreases, the dielectric maxima ($\varepsilon_m$) at 10 kHz decreases strongly from 25443 to 6473 for the BFBT-0.02BMN samples, and from 10891 to 4902 for the BFBT-0.06BMN samples. Notably, the $\varepsilon$-T curves of the fine-grained ceramics become broader and more extended on the temperature range, compared to the coarse-grained ceramics. Although the decrease of dielectric constant can be explained by the "brick-wall" model according to previous studies [141], this model does not account for any effect of the grain size on the domain structure. In fact, it only takes into account the parallel and series mixing of high-ε grains and low-ε grain boundaries. On the other hand, previous studies reported that the weakly coupled polar nanoregions (PNRs) may lead to the broadening of $\varepsilon$-T curve [177, 201]. Thus, it can be anticipated that the disruption of the ferroelectric long-range order makes an important contribution to the rapid reduction in $\varepsilon_m$ and the broadening $\varepsilon$-T curve of the fine-grained ceramics. Table 6.1 presents the dielectric properties at room temperature for BFBT-xBMN (x=0.02,0.06) ceramics with different grain sizes. It should be noted that although the $\varepsilon_m$ decreases with the decrease of grain size, the $\varepsilon$ at room temperature of the fine-grained ceramics increases compared to the coarse-grained ceramics. This feature further confirms that the changes in the dielectric properties could not be simply explained by the dielectric mixing rules, because the phenomenon of grain boundaries dilution induce reduced dielectric constant should occur over the entire temperature range. Yan et al. [202] recently reported that the enhancement of dielectric constant at room temperature was attributed to more active PNRs in the fine-grained $BaTiO_3$ ceramics. In the present work, the PNRs are expected to exist in the fine-grained BFBT-BMN ferroelectric ceramics.

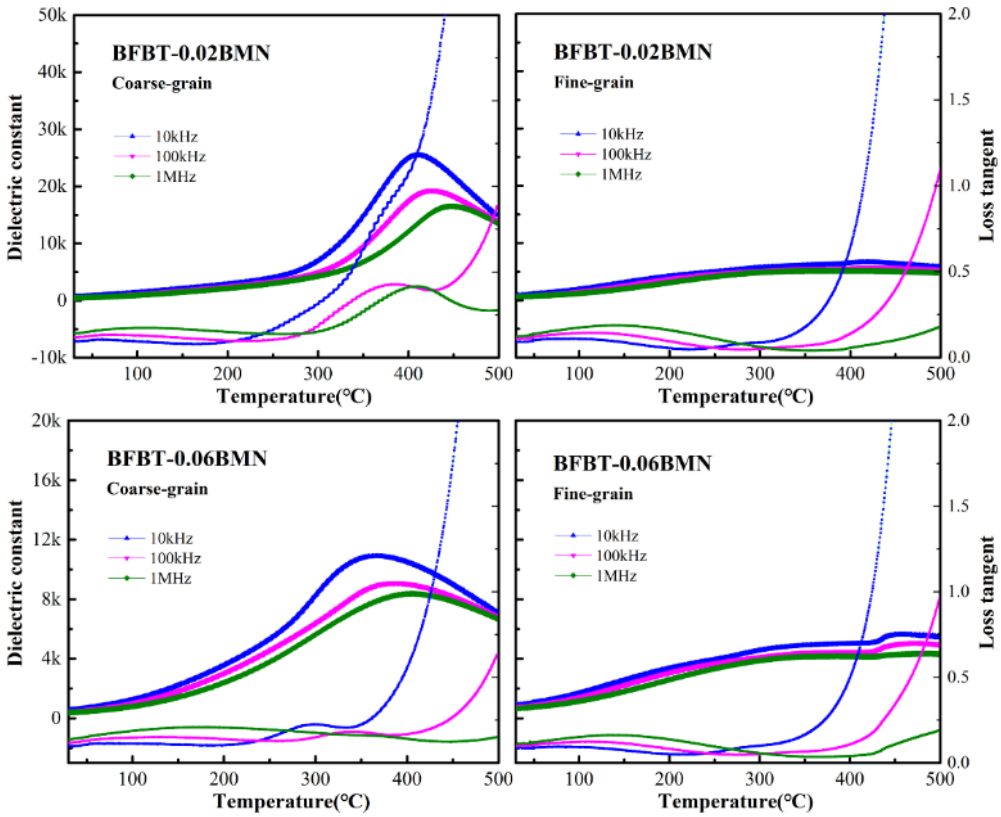


**Figure 6.5** Dielectric constant and loss tangent as a function of the temperature for the BFBT-xBMN (x=0.02, 0.06) ceramics with different grain sizes.

**Table 6.1** Comparisons of dielectric and ferroelectric properties of BFBT-xBMN (x=0.02, 0.06) ceramics with different grain sizes.

| | BFBT-0.02BMN | | BFBT-0.06BMN | |
|---|---|---|---|---|
| | Coarse-grain | Fine-grain | Coarse-grain | Fine-grain |
| Grain size (μm) | 2.87 | 0.55 | 4.1 | 0.89 |
| $\varepsilon$ [10kHz] | 623 | 859 | 520 | 832 |
| Loss tangent [10kHz] | 0.10 | 0.08 | 0.10 | 0.08 |
| $\varepsilon_m$ [10kHz] | 25400 | 6400 | 10800 | 4900 |
| $P_r$ (μC/cm$^2$)[50kV/cm] | 19.06 | 8.79 | 14.12 | 4.26 |
| $E_c$ (kV/cm)[50kV/cm] | 21.83 | 11.61 | 20.78 | 6.76 |

## 6.3.3 Ferroelectric properties

Fig. 6.6(a) shows the bipolar polarization hysteresis (*P*-*E*) loops of the

BF-BT-xBMN (x=0.02,0.06) ceramics with different grain sizes. First of all, the coarse-grained BFBT-BMN ceramics with nonergodic relaxor characteristics show a high remanent polarization. For these systems, $P_r$ decreases from 19.06 μC/cm$^2$ to 14.12 μC/cm$^2$ with increasing the content of BMN. Distinct shapes are observed in *P-E* loops for the ceramics with fine and coarse grain. As shown in Fig. 6.6(a), for the BFBT-0.06BMN ceramics, the coarse-grained samples show the rectangular ferroelectric loops with a high $P_r$ (14.12 μC/cm$^2$) and a high $E_C$ (20.78 kV/cm), while the narrow and slim ferroelectric hysteresis loops accompanied by a low $P_r$ (4.26 μC/cm$^2$) and a low $E_C$ (6.76 kV/cm) are observed in the fine-grained samples. The same features are also observed in the BFBT-0.02BMN ceramics. Furthermore, as can be seen from Fig. 6.6(b), the *I-E* loops of the coarse-grained ceramics exhibit two sharp ferroelectric switching peaks at the coercive field. This result implies the appearance of the irreversible long-range order during the cyclic electric field, accompanied by a large $P_r$. By decreasing the grain size, the *I-E* loops of BFBT-BMN ceramics gradually become flat and broad. The obtained results on the dielectric properties, the narrow *P-E* loops and broad *I-E* peaks may be attributed to the presence of PNRs induced in the fine-grained ceramics. It was reported that the PNRs are free to rotate under an external electric field and then may align along the direction of the electric field, corresponding to a low $E_C$ [177]. Upon the removal of the electric field, it would transform back to the initial state, accompanied by a small $P_r$. The role of the composition inducing weakly coupled short-range polar structures has been widely investigated in other reports [131, 203, 204]. In the present work, it is expected that the grain size reduction leads to the nanosized domains accompanied by the appearance of the dynamic and weakly correlated PNRs. The detailed dielectric and ferroelectric properties of BFBT-xBMN (x=0.02,0.06) ceramics with different grain sizes are presented in Table 6.1.

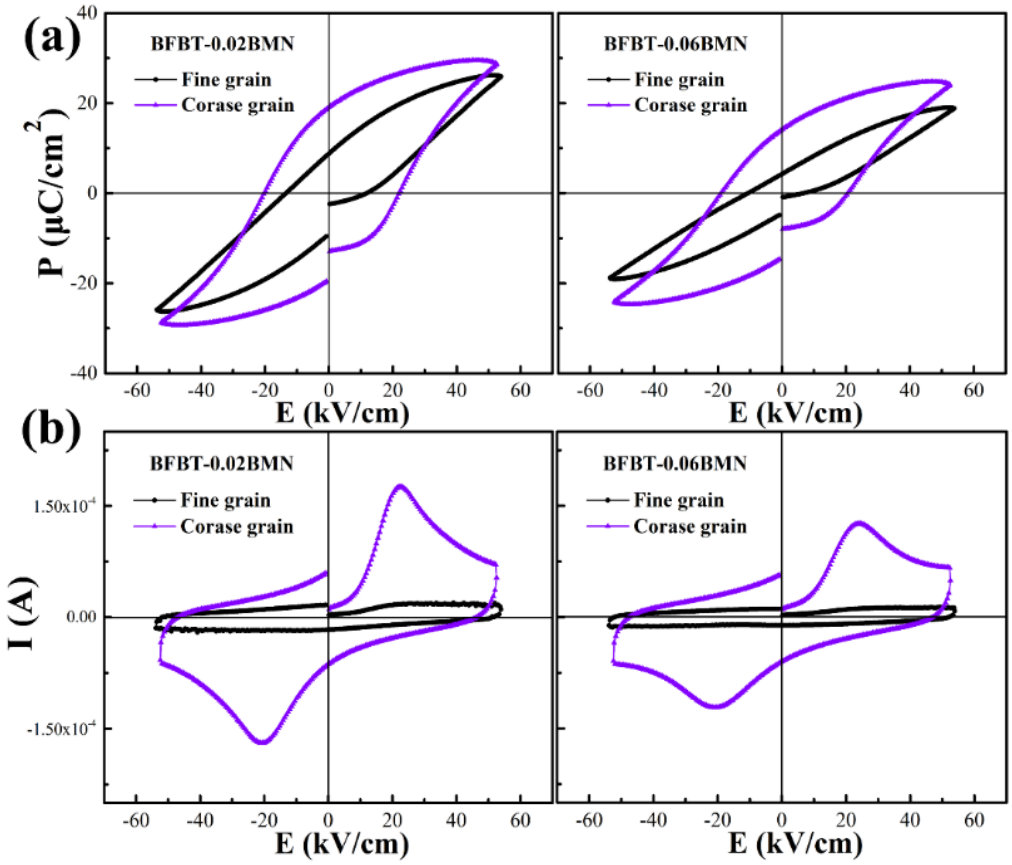


**Figure 6.6** (a) The bipolar polarization hysteresis loops; (b) the current-electric field loops of the BFBT-xBMN (x=0.02, 0.06) ceramics with different grain sizes.

## 6.3.4 Domain configuration

In order to achieve a deep understanding of the microstructural nature of the BFBT-BMN ceramics with different grain sizes. Piezoresponse force microscopy (PFM) and transmission electron microscopy (TEM) measurements were performed to shed light on the domain structures in the BFBT-0.06BMN ceramics. Fig. 6.7 shows the PFM image of polished surfaces obtained from the fine- and coarse-grained BFBT-xBMN (x=0.02, 0.06) ceramics. The bright and dark contrasts in piezoresponse images are ascribed to the opposite polarization directions [205]. A clear domain structure with a strong amplitude response is shown in the coarse-grained ceramics. However, the PFM image of the fine-grained ceramics shown by a blurry domain pattern with a weak contrast cannot evidence the domain structures. In addition, the TEM bright-field images of domain configurations are

shown in Fig. 6.8 where it can be clearly observed that lamellar domains with a width in the range of 80-100 nm exist in the coarse-grained ceramics. For the fine-grained ceramics, typical stripe-like PNRs with a width of 2 nm are shown as it was also reported in other relaxor ferroelectric system [195, 206]. The above observations further verify the existence of nanoscale ferroelectric domain in the fine-grained BFBT-BMN ceramics. The formation of the ferroelectric domain structures leads to the minimum energy for the electrostatic and the elastic energy in ferroelectric materials. Previous theoretical investigations revealed that the domain size decreases proportionally to the square root of the grain size [197]. When the grain size decreases, larger domains broken down to the nanosized domains leading to more dynamic and weakly correlated PNRs distributed in the fine-grained ceramics. As mentioned previously, the formation of PNRs may account for the dielectric and ferroelectric properties in the fine-grained BFBT-BMN ceramics, and it will improve the energy storage properties.

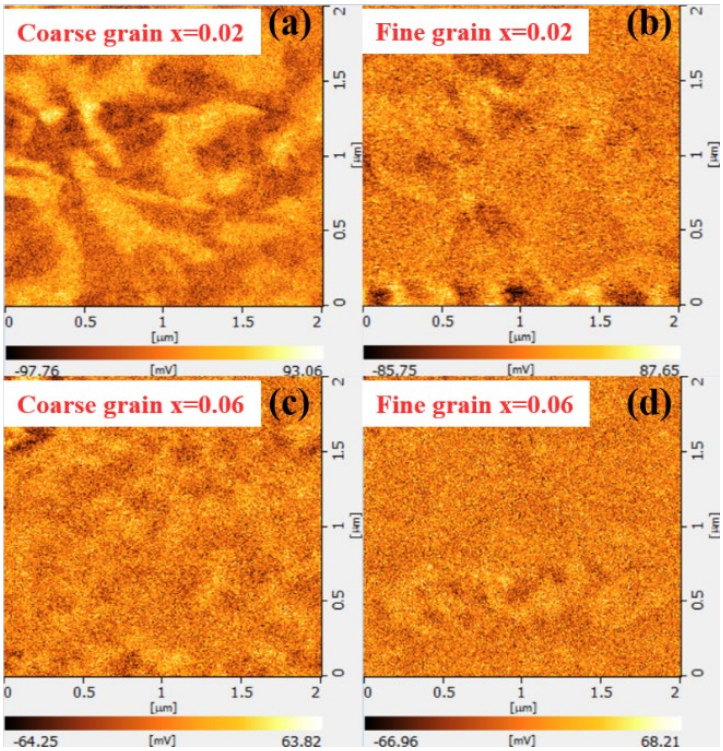


**Figure 6.7** Piezoresponse images of BFBT-xBMN (x=0.02, 0.06) ceramics with different grain sizes.

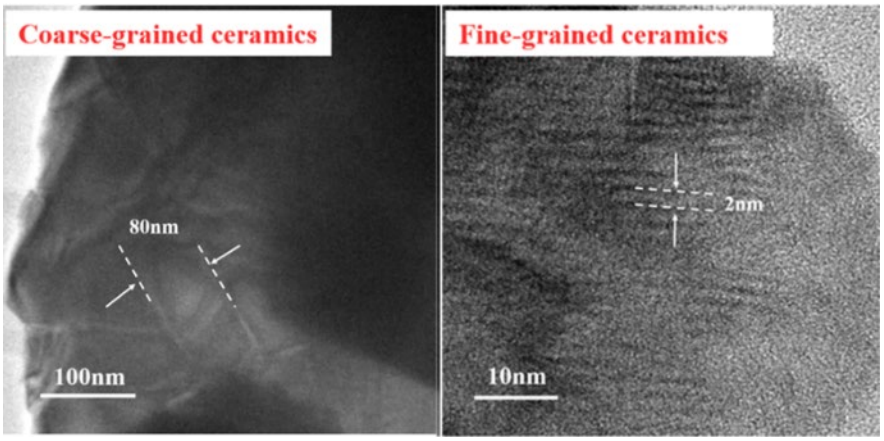


**Figure 6.8** TEM bright-field images of BFBT-0.06BMN ceramics with different grain sizes.

## 6.3.5 Energy storage properties

To further compare the energy storage properties, the *P-E* loops at the maximum applied electric field of the BFBT-0.06BMN ceramics with different grain sizes are shown in Fig. 6.9(a) and (b). As the grain size decreases, the polarization difference $\Delta P$ increases from 10 μC/cm$^2$ to 30 μC/cm$^2$, and the dielectric breakdown strength ($E_b$) increases from 50 kV/cm to 110 kV/cm. Tunkasiri et al. [207] have pointed out that the dielectric breakdown strength is proportional to $1/\sqrt{d}$, where $d$ is the grain size. The high grain boundaries density of the small grain-sized ceramics is suitable for enhancing the dielectric breakdown. As an important consequence of the decrease of $P_r$ and the increase of $E_b$, the recoverable energy density ($W_{re}$) of the fine-grained BFBT-0.06BMN ceramics increases drastically by 8 times from 0.16 J/cm$^3$ to 1.27 J/cm$^3$ compared to the coarse-grained BFBT-0.06BMN ceramics.

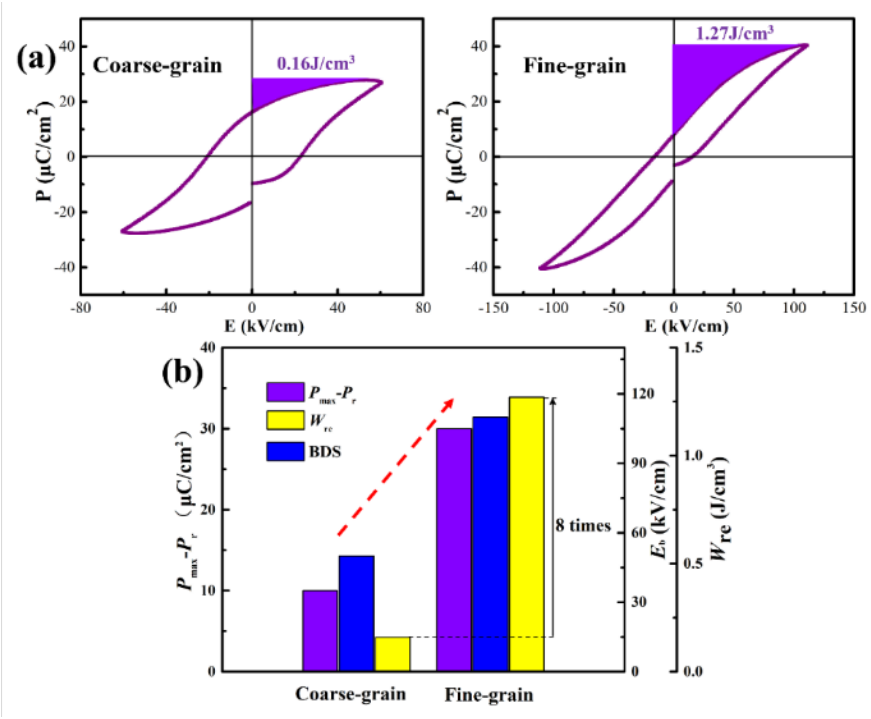


**Figure 6.9** (a) The *P-E* loops at maximum applied electric field for BFBT-0.06BMN ceramics with different grain sizes; (b) the corresponding value of $P_{max}$-$P_r$, $E_b$ and $W_{re}$ of ceramics.

## 6.4 Conclusions

In summary, lead-free $BiFeO_3$-based ceramics with different grain sizes were fabricated by the conventional solid-state method and a high-energy ball milling was used to realize the grain size reduction. The grain size effects on the energy storage properties of the BFBT-BMN ferroelectric ceramics were investigated. The main results are summarized below:

(1) All the ceramic samples show a pure perovskite structure with no secondary phases. A dense microstructure can be seen along with few pores distributed on the scanned surfaces. The high-energy ball milling process reduces the average grain size by 80% in the considered ceramics.

(2) The fine-grained BFBT-BMN ceramics show the narrow *P-E* loops with a low $P_r$ in contrast to the rectangular *P-E* loops with a high $P_r$ shown in the coarse-grained BFBT-BMN ceramics.

(3) Piezoresponse force microscopy (PFM) measurements revealed that the grain size reduction induced the transition from the micrometric ferroelectric domains to the weakly correlated polar nanoregions (PNRs), which contributes to the narrow and slim ferroelectric hysteresis loops in the fine-grained ceramics.

(4) The recoverable energy storage density of the fine-grained $BiFeO_3$-based ceramics greatly increased by 8 times from 0.16 J/cm$^3$ to 1.27 J/cm$^3$, compared to the coarse-grained ceramics. The reduction of grain size provides an effective method to obtain high-performance energy storage materials in the future.

# Chapter 7 General Conclusions and Future Work

## 7.1 Conclusions

In this paper, $BiFeO_3$-based ferroelectric ceramics were prepared by a conventional solid-state reaction method, and the structure, dielectric, ferroelectric and piezoelectric properties were systematically studied. Firstly, doping modification was used to design a novel ferroelectric $(0.76\text{-}x)BiFeO_3\text{-}0.24PbTiO_3\text{-}xBa(Sn_{0.2}Ti_{0.8})O_3$ ternary system with a high Curie temperature and the high piezoelectric properties. At the same time, the defect and pinning effect of this system was also studied. Second, the effects on the electrical properties of Mn-doped $0.7BiFeO_3\text{-}0.3PbTiO_3$ based ceramics were studied. In particular, the leakage conduction mechanism of ceramics was analyzed. Finally, lead-free $BiFeO_3\text{-}BaTiO_3$ based ceramics with a small grain size were prepared through the high-energy ball milling process, focusing on the effect of grain size on the ferroelectric domains and the energy storage properties of ceramics. The main achievements of this PhD thesis work are summarized below:

(1) The effects on the electrical properties of BF-PT based ceramics with different lead raw materials were studied. It turned out that the comprehensive electrical properties of BF-PT(PbO) ceramics were better than that of BF-PT($Pb_3O_4$) ceramics, which was quite different from other reports of lead-based piezoelectric ceramics. A small amount of Bi-rich second phase is precipitated at the grain boundaries of BF-PT($Pb_3O_4$) ceramics. The concentration of the oxygen vacancy and $Fe^{2+}$ ion in BF-PT($Pb_3O_4$) ceramics is significantly higher than that in BF-PT(PbO) ceramics, which exactly confirm the cause of high conductivity in BF-PT($Pb_3O_4$) ceramics. The results demonstrated for the first time that the different lead raw materials have great influence on the performance of BF-PT based piezoelectric ceramics.

(2) On the basis of the proper preparation process, the novel modified BF-PT

based ferroelectric ceramics were prepared. It was shown that the incorporation of large ionic radius $Ba^{2+}$ at A-site and non-ferroelectric-active $Sn^{4+}$ at B-site generates a decrease of the tetragonality degree *c/a*. Moreover, a wide multiphase coexistence region was formed with the content of BST ranging from 0.13 to 0.28. Enhanced piezoelectric coefficient (~200 pC/N) along with a high Curie temperature (~500 °C) was achieved simultaneously in the composition of 0.6BF-24PT-0.16BST. The excellent stability of the piezoelectric behavior was realized for temperatures as high as 450 °C. The achievement of the above characteristics was mainly favored by the design of the weakly distorted structures and the presence of nanodomains with facilitated polarization rotation in the investigated MPB ceramics. The relevant ferroelectric features demonstrated in the new BF-PT-BST ceramics pave the way for their promising applications as high-temperature piezoelectric materials.

(3) The comparison of the dielectric and ferroelectric properties for the poled and unpoled BF-PT-BST ceramics was studied. The poling process leads to the shifted and asymmetric *P-E* and *S-E* loops with an internal bias field, which is related to the formation of the defect dipole. The high temperature or low electric field frequency can make it easier for the migration of oxygen vacancies, thus leading to the reorientation of defect dipoles. Therefore, with increasing the temperature or decreasing the electric field frequency, the shape of *P-E* and *S-E* loops for the poled ceramics gradually changes from asymmetric to symmetric and the $E_i$ decreases. In addition, with the decrease of $BiFeO_3$ content, the difference in ferroelectric properties gradually disappeared and the internal bias field decreases for the unpoled and poled BF-PT-BST ceramics. This may be related to the decrease of the concentration of charged defects for the ceramics.

(4) All the 0.7BF-0.3PT+xwt%$MnCO_3$ ceramics exhibit a high Curie temperature, exceeding 600 °C, which is related to its large tetragonality. The dielectric loss-temperature curve of pure 0.7BF-0.3PT ceramics shows a relaxation peak in the temperature range of 30-250 °C and the frequency range of 100 Hz-1 MHz. The calculated activation energy ($E_{relax}$~0.74 eV, $E_{cond}$~0.92 eV) shows that the relaxation peak is related to the doubly-ionized oxygen vacancies. In addition, the

pure 0.7BF-0.3PT ceramics show a large leakage current density of about 12 μA/cm$^2$. With the addition of Mn, the leakage current density of the ceramics first decreases and then increases. A small amount (0.15 wt.%) of Mn doping can significantly reduce the leakage current of BF-PT ceramics, which is related to the decrease of the oxygen vacancy concentration for the ceramics. However, when the content of Mn increases (0.45 wt.%), the leakage current of ceramics increases instead, which may be related to the more carrier charges caused by the fluctuation in the valence of the B-site ion (Mn, Fe).

(5) The high-energy ball milling process reduces the average grain size by 80 % in the BFBT-BMN ceramics. The fine-grained BFBT-BMN ceramics show the narrow *P-E* loops with a low $P_r$ in contrast to the rectangular *P-E* loops with a high $P_r$ shown in the coarse-grained BFBT-BMN ceramics. Most importantly, a high recoverable energy density (~1.27 J/cm$^3$) was achieved in the fine-grained ceramics, which is much superior to the coarse-grained ceramics (~0.16 J/cm$^3$). The dynamic and weakly correlated PNRs structure can be obtained in the fined-grained BFBT-BMN ceramics, which is responsible for the enhancement of recoverable energy storage density of ceramics. Thus, the achieved work provides an in-depth understanding of the grain size effects in the BFBT-BMN ceramics, which may be a promising strategy to enhance the energy storage properties for the lead-free $BiFeO_3$-based ferroelectric ceramics.

## 7.2 Future work

***(1) Reduction of high-temperature loss of BF-PT based ceramics***

Through proper process and doping modification, the dielectric loss of BF-PT based ceramics at room temperature is effectively reduced. However, it was found that the dielectric loss of the material rises sharply with the temperature increases, which is unfavorable for its practical application as a piezoelectric device in high-temperature conditions. Therefore, it is necessary to further study the preparation of $BiFeO_3$-based ferroelectric ceramics with a low defect content through special processes such as oxygen sintering, hot pressing sintering, and

microwave sintering.

***(2) Study of the stability of BF-PT based ceramics***

Although a high Curie temperature and a high piezoelectric property were achieved in the novel BF-PT-BST ceramics, practical applications of piezoelectric devices require consideration of the complex external environments (e.g., temperature, electric field, aging, and stress). Therefore, it is critical to study the performance stability of ceramics under the complex external field. It is expected to study the variation of dielectric and piezoelectric properties of ceramics are studied by in-situ testing methods.

***(3) Development of energy storage performance of $BiFeO_3$-based ceramics***

This work has effectively improved the energy storage properties of the lead-free $BiFeO_3$-$BaTiO_3$ based ceramics through grain size reduction, but its performance still needs to be improved. Therefore, it is necessary to further optimize the compositions and preparation processes in order to obtain high energy storage properties in $BiFeO_3$-based ceramics.

# Bibliography


[1] 钟维烈. 铁电体物理学 [M]. 北京：科学出版社. 1996.

[2] 殷之文. 电介质物理学 [M]. 北京: 科学出版社. 2003.

[3] Jaffe B, Cook W R, Jaffe H. Piezoelectric ceramics [M]. Elsevier, 1971.

[4] Damjanovic D. Ferroelectric, dielectric and piezoelectric properties of ferroelectric thin films and ceramics [J]. Reports on Progress in Physics, 1998, 61(9): 1267–1324.

[5] Haertling G H. Ferroelectric ceramics: history and technology [J]. Journal of the American Ceramic Society, 1999, 82(4): 797-818.

[6] Kinase W, Uemura Y, Kikuchi M. Correction of dipole field due to lattice deformation of a perovskite-type crystal [J]. Journal of Physics and Chemistry of Solids, 1969, 30(2): 441-447.

[7] Dove M T. Theory of displacive phase transitions in minerals [J]. American Mineralogist, 1997, 82(3-4): 213-244.

[8] Whangbo, M H, Gordon, E E, Bettis J L. Tolerance factor and cation-anion orbital interactions differentiating the polar and antiferrodistortive structures of perovskite oxides $ABO_3$ [J]. Zeitschrift für Anorganische und Allgemeine Chemie, 2015, 641(6): 1043-1052.

[9] Vasala S, Karppinen M. $A_2B'B''O_6$ perovskites: A review [J]. Progress in Solid State Chemistry, 2015, 43(1-2):1-36.

[10] Leontsev S O, Eitel R E. Progress in engineering high strain lead-free piezoelectric ceramics [J]. Science and Technology of Advanced Materials, 2016, 11(4): 044302.

[11] Isupov V A. Some aspects of the physics of piezoelectric ceramics [J]. Ferroelectrics, 2011, 46(1): 217-225.

[12] Wersing W. Ferroelectric phase transitions in substituted barium titanate and lead zirconate titanate [J]. Ferroelectrics, 2011, 54(1): 207-210.

[13] Noheda B, Cox D E, Shirane G, et al. A monoclinic ferroelectric phase in the $Pb(Zr_{1-x}Ti_x)O_3$ solid solution [J]. Applied Physics Letters, 1999, 74(14): 2059-2061.

[14] Singh A K, Pandey D, Zaharko O. Powder neutron diffraction study of phase

transitions in and a phase diagram of (1-x)[$Pb(Mg_{1/3}Nb_{2/3})O_3$]-x$PbTiO_3$ [J]. Physical Review B, 2006, 74(2): 024101.

[15] Haun M J, Furman E, Jang S J, et al. Thermodynamic theory of the lead zirconate-titanate solid solution system, part I: Phenomenology [J]. Ferroelectrics, 1989, 99(1): 13-25.

[16] Rossetti G A, Khachaturyan A G, Akcay G, et al. Ferroelectric solid solutions with morphotropic boundaries: Vanishing polarization anisotropy, adaptive, polar glass, and two-phase states [J]. Journal of Applied Physics, 2008, 103(11): 114113.

[17] Theissmann R, Schmitt L A, Kling J, et al. Nanodomains in morphotropic lead zirconate titanate ceramics: On the origin of the strong piezoelectric effect [J]. Journal of Applied Physics, 2007, 102(2): 024111.

[18] Schmitt L A, Schönau K A, Theissmann R, et al. Composition dependence of the domain configuration and size in $Pb(Zr_{1-x}Ti_x)O_3$ ceramics [J]. Journal of Applied Physics, 2007, 101(7): 074107.

[19] Wang H, Zhu J, Lu N, et al. Hierarchical micro-/nanoscale domain structure in MC phase of (1-x)$Pb(Mg_{1/3}Nb_{2/3})O_3$-x$PbTiO_3$ single crystal [J]. Applied Physics Letters, 2006, 89(4): 042908.

[20] Wang K, Yao F Z, Jo W, et al. Temperature-insensitive (K,Na)$NbO_3$-based lead-free piezoactuator ceramics [J]. Advanced Functional Materials, 2013, 23(33): 4079-4086.

[21] Xue D, Zhou Y, Bao H, et al. Large piezoelectric effect in Pb-free $Ba(Ti,Sn)O_3$-x$(Ba,Ca)TiO_3$ ceramics [J]. Applied Physics Letters, 2011, 99(12): 122901.

[22] Liu W, Ren X. Large Piezoelectric Effect in Pb-Free Ceramics [J]. Physical Review Letters, 2009, 103(25): 257602.

[23] Gao J, Hu X, Wang Y, et al. Understanding the mechanism of large dielectric response in Pb-free (1-x)$Ba(Zr_{0.2}Ti_{0.8})O_3$-x$(Ba_{0.7}Ca_{0.3})TiO_3$ ferroelectric ceramics [J]. Acta Materialia, 2017, 125: 177-186.

[24] Zhang S, Yu F, Green D J. Piezoelectric materials for high temperature sensors [J]. Journal of the American Ceramic Society, 2011, 94(10): 3153-3170.

[25] Shinekumar K, Dutta S. High-temperature piezoelectrics with large piezoelectric coefficients [J]. Journal of Electronic Materials, 2014, 44(2): 613-622.

[26] Shrout T R, Zhang S J. Lead-free piezoelectric ceramics: Alternatives for PZT? [J]. Journal of Electroceramics, 2007, 19(1): 113-126.

[27] Zhao T L, Bokov A A, Wu J, et al. Giant piezoelectricity of ternary perovskite ceramics at high temperatures [J]. Advanced Functional Materials, 2019, 29(12): 1807920.

[28] Shulman H S, Testorf M, Damjanovic D, et al. Microstructure, electrical conductivity, and piezoelectric properties of bismuth titanate [J]. Journal of the American Ceramic Society, 1996, 79(12): 3124-28.

[29] Takenaka T, Nagata H. Current status and prospects of lead-free piezoelectric ceramics [J]. Journal of the European Ceramic Society, 2005, 25(12): 2693-2700.

[30] Takenaka T, Nagata H. Grain orientation and electrical properties of some bismuth layer-structured ferroelectrics for lead-free piezoelectric applications [J]. Ferroelectrics, 2011, 336(1): 119-136.

[31] Takeuchi T, Tani T, Saito Y. Unidirectionally textured $CaBi_4Ti_4O_{15}$ ceramics by the reactive templated grain growth with an extrusion [J]. Japanese Journal of Applied Physics, 2000, 39(9S): 5577-5580.

[32] Wang C M, Wang J F. High performance Aurivillius phase sodium-potassium bismuth titanate lead-free piezoelectric ceramics with lithium and cerium modification [J]. Applied Physics Letters, 2006, 89(20): 202905.

[33] Jiang X P, Yang Q, Zhou S L. et al. Microstructure and properties of high-temperature materials $(1-x)Na_{0.5}Bi_{2.5}Nb_2O_9$-$xLiNbO_3$ [J]. Journal of the American Ceramic Society, 2011, 94(4): 1109-1113.

[34] Soejima J, Sato K, Nagata K. Preparation and characteristics of ultrasonic transducers for high temperature using $PbNb_2O_6$ [J]. Japanese Journal of Applied Physics, 2000, 39(5S): 3083-3085.

[35] Subbarao E C. X-Ray Study of phase transitions in ferroelectric $PbNb_2O_6$ and related materials [J]. Journal of the American Ceramic Society, 1960, 43(9): 439-442.

[36] Soejima J, Nagata K. $PbNb_2O_6$ ceramics with tungsten bronze structure for low $Q_m$ piezoelectric material [J]. Japanese Journal of Applied Physics, 2001, 40(9S): 5747-5750.

[37] Inbar I, Cohen R E. Comparison of the electronic structures and energetics of ferroelectric $LiNbO_3$ and $LiTaO_3$ [J]. Physical Review B, 1996, 53(3):

1193-1204.

[38] Yamada M, Nada N, Saitoh M, et al. First-order quasi-phase matched $LiNbO_3$ waveguide periodically poled by applying an external field for efficient blue second-harmonic generation [J]. Applied Physics Letters, 1993, 62(5): 435-436.

[39] Kitamura K, Furukawa Y, Niwa K, et al. Crystal growth and low coercive field 180° domain switching characteristics of stoichiometric $LiTaO_3$ [J]. Applied Physics Letters, 1998, 73(21): 3073-3075.

[40] Karimi S, Reaney I M, Han Y, et al. Crystal chemistry and domain structure of rare-earth doped $BiFeO_3$ ceramics [J]. Journal of Materials Science, 2009, 44(19): 5102-5112.

[41] Shirane G, Hoshino S, Suzuki K. Crystal structure of lead titanate and of lead-barium titanate [J]. Journal of the Physical Society of Japan, 1950, 5(6): 453-455.

[42] Theis C D, Yeh J, Schlom D G, et al. Adsorption-controlled growth of $PbTiO_3$ by reactive molecular beam epitaxy [J]. Thin Solid Films, 1998, 325(1-2): 107-114.

[43] Hollenstein E, Davis M, Damjanovic D, et al. Piezoelectric properties of Li- and Ta-modified $(K_{0.5}Na_{0.5})NbO_3$ ceramics [J]. Applied Physics Letters, 2005, 87(18): 182905.

[44] Wang Y, Wu J, Xiao D, Wu, et al. High Curie temperature of (Li, K, Ag)-modified $(K_{0.50}Na_{0.50})NbO_3$ lead-free piezoelectric ceramics [J]. Journal of Alloys and Compounds, 2009, 472(1-2): L6-L8.

[45] Liang W, Wu W, Xiao D, et al. Effect of the addition of $CaZrO_3$ and $LiNbO_3$ on the phase transitions and piezoelectric properties of $K_{0.5}Na_{0.5}NbO_3$ lead-free ceramics [J]. Journal of the American Ceramic Society, 2011, 94(12): 4317-4322.

[46] Catalan G, Scott J F. Physics and applications of bismuth ferrite [J]. Advanced Materials, 2009, 21(24): 2463-2485.

[47] Lee M H, Kim D J, Park J S, et al. High-performance lead-free piezoceramics with high curie temperatures [J]. Advanced Materials, 2015, 27(43): 6976-82.

[48] Lee Y, Cho J, Kim B, et al. Piezoelectric properties and densification based on control of volatile mass of potassium and sodium in $(K_{0.5}Na_{0.5})NbO_3$ ceramics [J]. Japanese Journal of Applied Physics, 2008, 47(6): 4620-4622.

[49] Li X, Jiang M, Liu J, et al. Phase transitions and electrical properties of (1-x)($K_{0.5}Na_{0.5}$)$NbO_3$-x$BiScO_3$ lead-free piezoelectric ceramics with a CuO sintering aid [J]. Physica Status Solidi A, 2009, 206(11): 2622-2626.

[50] Zhang S, Xia R, Shrout T R, et al. Piezoelectric properties in perovskite 0.948($K_{0.5}Na_{0.5}$)$NbO_3$-0.052$LiSbO_3$ lead-free ceramics [J]. Journal of Applied Physics, 2006, 100(10): 104108.

[51] Duran C, Trolier-Mckinstry S, Messing G. Processing and electrical properties of 0.5Pb($Yb_{1/2}Nb_{1/2}$)O3-0.5$PbTiO_3$ ceramics [J]. Journal of Electroceramics, 2003, 10(1): 47-55.

[52] Lim J B, Zhang S, Shrout T R. Piezoelectric shear-mode properties of Pb($Yb_{1/2}Nb_{1/2}$)$O_3$-$PbTiO_3$ ceramics [J]. Materials Letters, 2010, 64(8): 951-952.

[53] Zhang S, Kim N, Shrout T R, et al. High temperature properties of manganese modified $CaBi_4Ti_4O_{15}$ ferroelectric ceramics [J]. Solid State Communications, 2006, 140(3-4): 154-158.

[54] Luo X, Zeng J T, Shi X, et al. Dielectric, ferroelectric and piezoelectric of $MnO_2$-doped Pb($Yb_{1/2}Nb_{1/2}$)$O_3$-Pb(Zr,Ti)$O_3$ ceramics [J]. Ceramics International, 2018, 44(7): 8456-8460.

[55] Zhou Z, Dong X, Chen H, et al. Structural and electrical properties of $W^{6+}$-doped $Bi_3TiNbO_9$ high-temperature piezoceramics [J]. Journal of the American Ceramic Society, 2006, 89(5): 1756-1760.

[56] Yan H, Ning H, Kan Y, et al. Piezoelectric ceramics with super-high curie points [J]. Journal of the American Ceramic Society, 2009, 92(10): 2270-2275.

[57] Eitel R E, Randall C A, Shrout T R, et al. New high temperature morphotropic phase boundary piezoelectrics based on Bi(Me)$O_3$-$PbTiO_3$ ceramics [J]. Japanese Journal of Applied Physics, 2001, 40(10R): 5999-6002.

[58] Eitel R E, Randall C A, Shrout T R, et al. Preparation and characterization of high temperature perovskite ferroelectrics in the solid solution (1-x)$BiScO_3$-x$PbTiO_3$ [J]. Japanese Journal of Applied Physics, 2002, 41(4A): 2099-2104.

[59] Cheng J R, Zhu W, Li N, et al. Fabrication and characterization of x$BiGaO_3$-(1-x)$PbTiO_3$: a high temperature reduced Pb-content piezoelectric ceramic [J]. Materials Letters, 2003, 57(13-14): 2090-2094.

[60] Duan R, Speyer R F, Alberta E, et al. High Curie temperature perovskite

$BiInO_3$-$PbTiO_3$ ceramics [J]. Journal of Materials Research, 2011, 19(7): 2185-2193.

[61] Zhang S, Xia R, Randall C A, et al. Dielectric and piezoelectric properties of niobium-modified $BiInO_3$-$PbTiO_3$ perovskite ceramics with high Curie temperatures [J]. Journal of Materials Research, 2005, 20(8): 2067-2071.

[62] Gao F, Hong R, Liu J, et al. Phase formation and characterization of high Curie temperature x$BiYbO_3$-(1-x)$PbTiO_3$ piezoelectric ceramics [J]. Journal of the European Ceramic Society, 2009, 29(9): 1687-1693.

[63] Gao F, Hong R, Liu J, et al. Phase structure and piezoelectric properties of high Curie temperature $BiYbO_3$-$PbTiO_3$-$BaTiO_3$ ceramics [J]. Journal of Alloys and Compounds, 2009, 475(1-2): 619-623.

[64] Randall C A, Eitel R, Jones B, et al. Investigation of a high $T_c$ piezoelectric system: (1-x)$Bi(Mg_{1/2}Ti_{1/2})O_3$-(x)$PbTiO_3$ [J]. Journal of Applied Physics, 2004, 95(7): 3633-3639.

[65] Zhang S, Stringer C, Xia R, et al. Investigation of bismuth-based perovskite system: (1-x)$Bi(Ni_{2/3}Nb_{1/3})O_3$-x$PbTiO_3$ [J]. Journal of Applied Physics, 2005, 98(3): 034103.

[66] Hou X, Yu J, Randall C A. Perovskite-structured $BiFeO_3$-$Bi(Zn_{1/2}Ti_{1/2})O_3$-$PbTiO_3$ solid solution piezoelectric ceramics with Curie temperature about 700°C [J]. Journal of the American Ceramic Society, 2013, 96(7): 2218-2224.

[67] Smith R T, Achenbach G D, Gerson R, et al. Dielectric properties of solid solutions of $BiFeO_3$ with Pb(Ti, Zr)$O_3$ at high temperature and high frequency [J]. Journal of Applied Physics, 1968, 39(1): 70-74.

[68] Cheng J, Meng Z, Cross L E. High-field and high-$T_c$ piezoelectric ceramics based on Bi(Ga,Fe)$O_3$-$PbTiO_3$ crystalline solutions [J]. Journal of Applied Physics, 2005, 98(8): 084102.

[69] Choi S M, Stringer C J, Shrout T R, et al. Structure and property investigation of a Bi-based perovskite solid solution: (1-x)$Bi(Ni_{1/2}Ti_{1/2})O_3$-x$PbTiO_3$ [J]. Journal of Applied Physics, 2005, 98(3): 034108.

[70] Suchomel M R, Davies P K. Enhanced tetragonality in (x)$PbTiO_3$-(1-x)$Bi(Zn_{1/2}Ti_{1/2})O_3$ and related solid solution systems [J]. Applied Physics Letters, 2005, 86(26): 262905.

[71] Suchomel M R, Davies P K. Predicting the position of the morphotropic phase

boundary in high temperature $PbTiO_3$-$Bi(B'B'')O_3$ based dielectric ceramics [J]. Journal of Applied Physics, 2004, 96(8): 4405-4410.

[72] Tinte S, Rabe K M, Vanderbilt D, Anomalous enhancement of tetragonality in $PbTiO_3$ induced by negative pressure [J]. Physical Review B, 2003, 68(14): 144105.

[73] Grinberg I, Suchomel M R, Davies P K, et al. Predicting morphotropic phase boundary locations and transition temperatures in Pb- and Bi-based perovskite solid solutions from crystal chemical data and first-principles calculations [J]. Journal of Applied Physics, 2005, 98(9): 094111.

[74] Stringer C J, Shrout T R, Randall C A, et al. Classification of transition temperature behavior in ferroelectric $PbTiO_3$-$Bi(Me'Me'')O_3$ solid solutions [J]. Journal of Applied Physics, 2006, 99(2), 024106.

[75] Naganuma H. Multifunctional characteristics of B-site substituted $BiFeO_3$ films [M]. Ferroelectrics-Physical Effects, 2011.

[76] Ederer C, Spaldin N A. Effect of epitaxial strain on the spontaneous polarization of thin film ferroelectrics [J]. Physical Review Letters, 2005, 95(25): 257601.

[77] Wang J. Epitaxial $BiFeO_3$ multiferroic thin film heterostructures [J]. Science, 2003, 299(5613): 1719-1722.

[78] Li J, Wang J, Wuttig M, et al. Dramatically enhanced polarization in (001), (101), and (111) $BiFeO_3$ thin films due to epitiaxial-induced transitions [J]. Applied Physics Letters, 2004, 84(25): 5261-5263.

[79] Wang Y P, Zhou L, Zhang M F, et al. Room-temperature saturated ferroelectric polarization in $BiFeO_3$ ceramics synthesized by rapid liquid phase sintering [J]. Applied Physics Letters, 2004, 84(10):1731-1733.

[80] Wang L C, Wang Z H, He S L, et al. Enhanced magnetization and suppressed current leakage in $BiFeO_3$ ceramics prepared by spark plasma sintering of sol-gel derived nanoparticles [J]. Physica B: Condensed Matter, 2012, 407(8): 1196-1202.

[81] Nadeem M, Khan W. Khan S, et al. Tailoring dielectric properties and multiferroic behavior of nanocrystalline $BiFeO_3$ via Ni doping [J]. Journal of Applied Physics, 2018, 124(16): 164105.

[82] Cai W, Gao R, Fu C, et al. Microstructure, enhanced electric and magnetic properties of $Bi_{0.9}La_{0.1}FeO_3$ ceramics prepared by microwave sintering [J].

Journal of Alloys and Compounds, 2019, 774: 61-68.

[83] Chen X, Wang J, Yuan G, et al. Structure, ferroelectric and piezoelectric properties of multiferroic $Bi_{0.875}Sm_{0.125}FeO_3$ ceramics [J]. Journal of Alloys and Compounds, 2012, 541: 173-176.

[84] Zheng T, Wu J. Enhanced piezoelectric activity in high-temperature $Bi_{1-x-y}Sm_xLa_yFeO_3$ lead-free ceramics [J]. Journal of Materials Chemistry C, 2015, 3(15): 3684-3693.

[85] Yuan G L, Or S W, Chan H L. Structural transformation and ferroelectric-paraelectric phase transition in $Bi_{1-x}La_xFeO_3$(x=0-0.25) multiferroic ceramics [J]. Journal of Physics D: Applied Physics, 2007, 40(4): 1196-1200.

[86] Tao H, Lv J, Zhang R, et al. Lead-free rare earth-modified $BiFeO_3$ ceramics: Phase structure and electrical properties [J]. Materials & Design, 2017, 120: 83-89.

[87] Lv J, Lou X, Wu J. Defect dipole-induced poling characteristics and ferroelectricity of quenched bismuth ferrite-based ceramics [J]. Journal of Materials Chemistry C, 2016, 4(25): 6140-6151.

[88] Zheng T, Wu J. Effects of site engineering and doped element types on piezoelectric and dielectric properties of bismuth ferrite lead-free ceramics [J]. Journal of Materials Chemistry C, 2015, 3 (43): 11326-11334.

[89] Kumar V, Gaur A, Kotnala R K. Anomalous dielectric response with suppression in Neel temperature of $Bi_{0.9}Y_{0.1}Fe_{1-x}Mn_xO_3$ ($0<x<0.07$) ceramics [J]. Journal of Alloys and Compounds, 2013, 551: 410-414.

[90] Malič B, Koruza J, Hreščak J, et al. Sintering of lead-free piezoelectric sodium potassium niobate ceramics [J]. Materials, 2015, 8(12): 8117-8146.

[91] Woodward D I, Reaney I M, Eitel R E, et al. Crystal and domain structure of the $BiFeO_3$-$PbTiO_3$ solid solution [J]. Journal of Applied Physics, 2003, 94(5): 3313-3318.

[92] Zhu W M, Guo H Y, Ye Z G. Structural and magnetic characterization of multiferroic $(BiFeO_3)_{1-x}(PbTiO_3)_x$ solid solutions [J]. Physical Review B, 2008, 78 (1): 014401.

[93] Bhattacharjee S, Tripathi S, Pandey D. Morphotropic phase boundary in (1-x)$BiFeO_3$-x$PbTiO_3$: phase coexistence region and unusually large tetragonality [J]. Applied Physics Letters, 2007, 91(4): 042903.

[94] Bhattacharjee S, Pandey D. Stability of the various crystallographic phases of the multiferroic (1-x)$BiFeO_3$-x$PbTiO_3$ system as a function of composition and temperature [J]. Journal of Applied Physics, 2010, 107(12): 124112.

[95] Bhattacharjee S, Pandey V, Kotnala R K, et al. Unambiguous evidence for magnetoelectric coupling of multiferroic origin in 0.73$BiFeO_3$-0.27$PbTiO_3$ [J]. Applied Physics Letters, 2009, 94(1): 012906.

[96] Bhattacharjee S, Senyshyn A, Krishna P S R, et al. Simultaneous changes of nuclear and magnetic structures across the morphotropic phase boundary in (1-x)$BiFeO_3$-x$PbTiO_3$ [J]. Applied Physics Letters, 2010, 97(26): 262506.

[97] Bhattacharjee S, Pandey D. Effect of stress induced monoclinic to tetragonal phase transformation in the multiferroic (1-x)$BiFeO_3$-x$PbTiO_3$ system on the width of the morphotropic phase boundary and the tetragonality [J]. Journal of Applied Physics, 2011, 110(8): 084105.

[98] Hooper T E, Bell A J. Landau-Devonshire derived phase diagram of the $BiFeO_3PbTiO_3$ solid solution [J]. Journal of Applied Physics, 2020, 127(10): 104102.

[99] Sunder S, Halliyal A, Umarji A M. Investigation of tetragonal distortion in the $PbTiO_3$-$BiFeO_3$ system by high-temperature x-ray diffraction [J]. Journal of Materials Research, 1995, 10(5): 1301-1306.

[100] Kounga A B, Granzow T, Aulbach E, et al. High-temperature poling of ferroelectrics [J]. Journal of Applied Physics, 2008, 104(2): 024116.

[101] Leist T, Granzow T, Jo W, et al. Effect of tetragonal distortion on ferroelectric domain switching: A case study on La-doped $BiFeO_3$-$PbTiO_3$ ceramics [J]. Journal of Applied Physics, 2010, 108(1): 014103.

[102] Lynch C S. The effect of uniaxial stress on the electro-mechanical response of 8/63/35 PLZT [J]. Acta Materialia, 1996, 44(10): 4137-4148.

[103] Grinberg I, Suchomel M R, Dmowski W, et al. Structure and polarization in the high $T_c$ ferroelectric Bi(Zn,Ti)$O_3$-$PbTiO_3$ solid solutions [J]. Physical Review Letters, 2007, 98(10): 107601.

[104] Freitas V F, Dias G S, Protzek O A, et al. Structural phase relations in perovskite-structured $BiFeO_3$-based multiferroic compounds [J]. Journal of Advanced Ceramics, 2013, 2(2): 103-111.

[105] Yashima M, Omoto K, Chen J, et al. Evidence for (Bi,Pb)-O covalency in the high $T_C$ ferroelectric $PbTiO_3$-$BiFeO_3$ with large tetragonality [J]. Chemistry of

Materials, 2011, 23(13): 3135-3137.

[106] Cheng J R, Eitel R, Cross L E. Lanthanum-modified (1-x)($Bi_{0.8}La_{0.2}$)($Ga_{0.05}Fe_{0.95}$)$O_3$-x$PbTiO_3$ crystalline solutions: Novel morphotropic phase-boundary lead-reduced piezoelectrics [J]. Journal of the American Ceramic Society, 2003, 86(12): 2111-2115.

[107] Cheng J R, Cross L E. Effects of La substituent on ferroelectric rhombohedral/tetragonal morphotropic phase boundary in (1-x)(Bi,La)($Ga_{0.05}Fe_{0.95}$)$O_3$-x$PbTiO_3$ piezoelectric ceramics [J]. Journal of Applied Physics, 2003, 94(8): 5188.

[108] Cheng J R, Li N, Cross L E. Structural and dielectric properties of Ga-modified $BiFeO_3$-$PbTiO_3$ crystalline solutions [J]. Journal of Applied Physics, 2003, 94(8): 5153.

[109] Chen J, Cheng J, Enhanced high-field strain and reduced high-temperature dielectric loss in 0.6($Bi_{0.9}La_{0.1}$)($Fe_{1-x}Ti_x$)$O_3$-0.4$PbTiO_3$ piezoelectric ceramics [J]. Ceramics International, 2015, 41(1): 1617-1621.

[110] Li Q, Dong Y, Cheng J, et al. Enhanced dielectric and piezoelectric properties in $BaZrO_3$ modified $BiFeO_3$-$PbTiO_3$ high temperature ceramics [J]. Journal of Materials Science: Materials in Electronics, 2016, 27(7): 7100-7104.

[111] Li Z A, Yang H X, Tian H F, et al. Transmission electron microscopy study of multiferroic ($Bi_{1-x}La_x$)$FeO_3$-$PbTiO_3$ with x=0.1, 0.2, and 0.3 [J]. Applied Physics Letters, 2007, 90(18): 182904.

[112] Ning Z, Jiang Y, Jian J, et al. Achieving both large piezoelectric constant and high Curie temperature in $BiFeO_3$-$PbTiO_3$-$BaTiO_3$ solid solution [J]. Journal of the European Ceramic Society, 2020, 40(6): 2338-2344.

[113] Zuo R, Wu Y, Fu J, et al. Influences of dopants on $BiFeO_3$-$PbTiO_3$ ferroelectric ceramics [J]. Materials Chemistry and Physics, 2009, 113(1): 361-364.

[114] Zhu W M, Ye Z G. Effects of chemical modification on the electrical properties of 0.67$BiFeO_3$-0.33$PbTiO_3$ ferroelectric ceramics [J]. Ceramics International, 2004, 30(7): 1435-1442.

[115] Fan L, Chen J, Li S, et al. Enhanced piezoelectric and ferroelectric properties in the $BaZrO_3$ substituted $BiFeO_3$-$PbTiO_3$ [J]. Applied Physics Letters, 2013, 102(2): 022905.

[116] Hu W, Tan X, Rajan K. $BiFeO_3$-$PbZrO_3$-$PbTiO_3$ ternary system for high Curie

temperature piezoceramics [J]. Journal of the European Ceramic Society, 2011, 31(5): 801-807.

[117] Hu W, Tan X, Rajan K, et al. Piezoelectric ceramics with compositions at the morphotropic phase boundary in the $BiFeO_3$-$PbZrO_3$-$PbTiO_3$ ternary system [J]. Journal of the American Ceramic Society, 2011, 94(12): 4358-4363.

[118] Narayan B, Malhotra J S, Pandey R, et al. Electrostrain in excess of 1% in polycrystalline piezoelectrics [J]. Nature Materials, 2018, 17(5): 427-431.

[119] Kumar M M, Srinivas A, Suryanarayana S V. Structure property relations in $BiFeO_3$/$BaTiO_3$ solid solutions [J]. Journal of Applied Physics, 2000, 87(2): 855-862.

[120] Leontsev S O, Eitel R E. Dielectric and piezoelectric properties in Mn-modified (1-x)$BiFeO_3$-x$BaTiO_3$ ceramics [J]. Journal of the American Ceramic Society, 2009, 92(12): 2957-2961.

[121] Wei Y, Wang X, Zhu J, et al. Dielectric, ferroelectric, and piezoelectric properties of $BiFeO_3$-$BaTiO_3$ ceramics [J]. Journal of the American Ceramic Society, 2013, 96(10): 3163-3168.

[122] Zhou C, Feteira A, Shan X, et al. Remarkably high-temperature stable piezoelectric properties of $Bi(Mg_{0.5}Ti_{0.5})O_3$ modified $BiFeO_3$-$BaTiO_3$ ceramics [J]. Applied Physics Letters, 2012, 101(3): 032901.

[123] Wei J, Fu D, Cheng J, et al. Temperature dependence of the dielectric and piezoelectric properties of x$BiFeO_3$-(1-x)$BaTiO_3$ ceramics near the morphotropic phase boundary [J]. Journal of Materials Science, 2017, 52(18): 10726-10737.

[124] Burn I, Smyth D M. Energy storage in ceramic dielectrics [J]. Journal of Materials Science, 1972, 7: 339-343

[125] Kwon S, Hackenberger W, Alberta E. Nonlinear dielectric ceramics and their applications to capacitors and tunable dielectrics [J]. IEEE Electrical Insulation Magazine, 2011, 27(2): 43-55.

[126] Yao Z, Song Z, Hao H, et al. Homogeneous/inhomogeneous-structured dielectrics and their energy-storage performances [J]. Advance Materials, 2017, 29(20): 1601727.

[127] Zheng D, Zuo R, Zhang D, et al. Novel $BiFeO_3$-$BaTiO_3$-$Ba(Mg_{1/3}Nb_{2/3})O_3$ lead-free relaxor ferroelectric ceramics for energy-storage capacitors [J]. Journal of the American Ceramic Society, 2015, 98(9): 2692-2695.

[128] Zheng D, Zuo R. Enhanced energy storage properties in $La(Mg_{1/2}Ti_{1/2})O_3$-modified $BiFeO_3$-$BaTiO_3$ lead-free relaxor ferroelectric ceramics within a wide temperature range [J]. Journal of the European Ceramic Society, 2017, 37(1): 413-418.

[129] Li F, Zhai J, Shen B, et al. Multifunctionality of lead-free $BiFeO_3$-based ergodic relaxor ferroelectric ceramics: High energy storage performance and electrocaloric effect [J]. Journal of Alloys and Compounds, 2019, 803: 185-192.

[130] Liu N, Xu C, Zhou Z, et al. Novel bismuth ferrite-based lead-free ceramics with high energy and power density [J]. Journal of the American Ceramic Society, 2018, 101: 3259-3265.

[131] Liu N, Liang R, Zhou Z, et al. Designing lead-free bismuth ferrite-based ceramics learning from relaxor ferroelectric behavior for simultaneous high energy density and efficiency under low electric field [J]. Journal of Materials Chemistry C, 2018, 6: 10211-10217.

[132] Park T J, Papaefthymiou G C, Viescas A J, et al. Composition-dependent magnetic properties of $BiFeO_3$-$BaTiO_3$ solid solution nanostructures [J]. Physical Review B, 2010, 82(2): 024431.

[133] Jin L, Li F, Zhang S, et al. Decoding the fingerprint of ferroelectric loops: comprehension of the material properties and structures [J]. Journal of the American Ceramic Society, 2014, 97(1): 1-27.

[134] Acosta M, Novak N, Rojas V, et al. $BaTiO_3$-based piezoelectrics: Fundamentals, current status, and perspectives [J]. Applied Physics Reviews, 2017, 4(4): 041305.

[135] Zhang S, Li F, Jiang X, et al. Advantages and challenges of relaxor-$PbTiO_3$ ferroelectric crystals for electroacoustic transducers- a review. Progress in Materials Science [J]. 2015, 68: 1-66.

[136] Kumar M M, Palkar V R, Srinivas K, et al. Ferroelectricity in a pure $BiFeO_3$ ceramic [J]. Applied Physics Letters, 2000, 76(19): 2764-2766.

[137] Zhu W M, Ye Z G. Improved dielectric and ferroelectric properties of high Curie temperature (1-x)$BiFeO_3$-x$PbTiO_3$ ceramics by aliovalent ionic substitution [J]. Applied Physics Letters, 2006, 89(23): 232904.

[138] Du F, Cui B, Cheng H, et al. Synthesis, characterization, and dielectric properties of $Ba(Ti_{1-x}Sn_x)O_3$ nanopowders and ceramics [J]. Materials

Research Bulletin, 2009, 44(9): 1930-1934.

[139] Hou Y, Zhu M, Gao F. Effect of $MnO_2$ addition on the structure and electrical properties of $Pb(Zn_{1/3}Nb_{2/3})_{0.20}(Zr_{0.50}Ti_{0.50})_{0.80}O_3$ ceramics [J]. Journal of the American Ceramic Society, 2004, 87(5): 847-850.

[140] Frey M H, Xu Z, Han P, et al. The role of interfaces on an apparent grain size effect on the dielectric properties for ferroelectric barium titanate ceramics [J]. Ferroelectrics, 1998, 206(1): 337-353.

[141] Ihlefeld J F, Harris D T, Keech R, et al. Scaling effects in perovskite ferroelectrics: Fundamental limits and process-structure-property relations. Journal of the American Ceramic Society, 2016, 99(8): 2537-2557.

[142] Slonopas A, Foley B J, Choi J J, et al. Charge transport in bulk $CH_3NH_3PbI_3$ perovskite [J]. Journal of Applied Physics, 2016, 119(7): 074101.

[143] Guo Y, Xiao P, Wen R, et al. Critical roles of Mn-ions in enhancing the insulation, piezoelectricity and multiferroicity of $BiFeO_3$-based lead-free high temperature ceramics [J]. Journal of Materials Chemistry C, 2015, 3(22): 5811-5824.

[144] Lu C, Chang D. Reaction sintering and characterization of lead magnesium niobate relaxor ferroelectric ceramics [J]. Journal of Materials Science: Materials in Electronics, 2000, 11: 363-367.

[145] Zhang J, Mo S, Wang H, et al. Microstructure and electrical properties of PLZT ceramics from $Pb_3O_4$ as the lead source [J]. Journal of Alloys and Compounds, 2011, 509(6): 2838-2841.

[146] Boutarfaia A. Study of the solid state reaction and the morphotropic phase boundary in $Pb(Zr, Ti)O_3$-$Pb(Fe_{1/5}, Ni_{1/5}, Sb_{3/5})O_3$ ceramics [J]. Ceramics International, 2001, 27: 91-97.

[147] Kim S, Choi H, Han S, et al. A correlation between piezoelectric response and crystallographic structural parameter observed in lead-free $(1-x)(Bi_{0.5}Na_{0.5})TiO_3$-$xSrTiO_3$ piezoelectrics [J]. Journal of the European Ceramic Society, 2017, 37(4): 1379-1386.

[148] Abrahams S C, Kurtz S K, Jamieson P B. Atomic displacement relationship to Curie temperature and spontaneous polarization in displacive ferroelectrics [J]. Physical Review, 1968, 172(2): 551-553.

[149] Liu W, Cheng L, Gao J, et al. Composition design and electrical properties of $(K_{0.48}Na_{0.52})NbO_3$-$xLiSbO_3$}-y{$(Bi_{0.5}Na_{0.5})(Zr_{1-z}Sn_z)O_3$} ceramics [J].

Materials & Design, 2017, 136: 119-126.

[150] Liu X, Tan X. Giant strains in non-textured $(Bi_{1/2}Na_{1/2})TiO_3$-based lead-free ceramics [J]. Advance Materials, 2016, 28(3): 574-8.

[151] Huang C, Cai K, Wang Y, et al. Revealing the real high temperature performance and depolarization characteristics of piezoelectric ceramics by combined in situ techniques [J]. Journal of Materials Chemistry C, 2018, 6(6): 1433-1444.

[152] Xu K, Li J, Lv X, et al. Superior piezoelectric properties in potassium-sodium niobate lead-free ceramics [J]. Advance Materials, 2016, 28(38): 8519-8523.

[153] Zuo R, Qi H, Xie A, et al. Anomalously large lattice strain contributions from rhombohedral phases in $BiFeO_3$-based high-temperature piezoceramics estimated by means of in-situ synchrotron x-ray diffraction [J]. Journal of the European Ceramic Society, 2018, 38(14): 4653-4658.

[154] Kumar N, Bastola N, Kumar S, et al. Relaxor dielectric behavior in $BaTiO_3$ substituted $BiFeO_3$-$PbTiO_3$ multiferroic system [J]. Journal of Materials Science: Materials in Electronics, 2017, 28(14): 10420-10426.

[155] Joseph A J, Goel S, Hussain A, et al. Ferro-/pyroelectric response of 0.57BF-0.31PMN-0.12PT ternary ceramic far away from morphotropic phase boundaries [J]. Ceramics International, 2017, 43(18): 16676-16683.

[156] Pang D, He C, Long X. Multiferroic ternary solid solution system of $BiFeO_3$-$NdFeO_3$-$PbTiO_3$ [J]. Journal of Alloys and Compounds, 2017, 709: 16-23.

[157] Zhou Q, Zhou C, Yang H, et al. Dielectric, ferroelectric, and piezoelectric properties of $Bi(Ni_{1/2}Ti_{1/2})O_3$-modified $BiFeO_3$-$BaTiO_3$ ceramics with high Curie temperature [J]. Journal of the American Ceramic Society, 2012, 95(12): 3889-3893.

[158] Tressler J F, Alkoy S, Newnham R E. Piezoelectric Sensors and Sensor Materials [J]. Journal of Electroceramics, 1998, 2(4): 257-272.

[159] Zong L C, Zeng J T, Zhao SC, et al. Study on A-site cation doping of $CaBi_2Nb_2O_9$ with bismuth layered structure [J]. Journal of Inorganic Materials, 2012, 27(7): 726-730.

[160] Li B S, Zhu Z G, Li G R, et al. Peculiar hysteresis loop of $Pb(Mn_{1/3}Nb_{2/3})O_3$-Pb(Ti, Zr)$O_3$ ceramics [J]. Japanese Journal of Applied Physics, 2004, 43(4A): 1458-1463.

[161] Du G, Liang R, Wang L, et al. Large stable strain memory effect in poled Mn-doped $Pb(Mn_{1/3}Sb_{2/3})O_3$-$Pb(Zr,Ti)O_3$ ceramics [J]. Applied Physics Letters, 2013, 102(16): 162907.

[162] Ren X. Large electric-field-induced strain in ferroelectric crystals by point-defect-mediated reversible domain switching [J]. Nature Materials, 2004, 3(2): 91-94.

[163] Huang X X, Zhang T F, Tang X G, et al. Dielectric relaxation and pinning phenomenon of $(Sr,Pb)TiO_3$ ceramics for dielectric tunable device application [J]. Scientific Reports, 2016, 6: 31960.

[164] Zeng J, Zhao K, Shi X, et al. Large strain induced by the alignment of defect dipoles in ($Bi^{3+}$,$Fe^{3+}$) co-doped $Pb(Zr,Ti)O_3$ ceramics [J]. Scripta Materialia, 2018, 142: 20-22.

[165] Kamel T M, With G. Poling of hard ferroelectric PZT ceramics [J]. Journal of the European Ceramic Society, 2008, 28(9): 1827-1838.

[166] Yuan G L, Yang Y, Or S W. Aging-induced double ferroelectric hysteresis loops in $BiFeO_3$ multiferroic ceramic [J]. Applied Physics Letters, 2007, 91(12): 122907.

[167] Rojac T, Kosec M, Budic B, et al. Strong ferroelectric domain-wall pinning in $BiFeO_3$ ceramics [J]. Journal of Applied Physics, 2010, 108(7): 074107.

[168] Geng W R, Tian X H, Jiang Y X, et al. Unveiling the pinning behavior of charged domain walls in $BiFeO_3$ thin films via vacancy defects [J]. Acta Materialia, 2020, 186: 68-76.

[169] Carl K, Hardtl K H. Electrical after-effects in $Pb(Ti,Zr)O_3$ ceramics [J]. Ferroelectrics, 1977, 17(1): 473-486.

[170] Zhang L, Erdem E, Ren X, et al. Reorientation of $(Mn_{Ti}''-V_O^{\bullet\bullet})^{\times}$ defect dipoles in acceptor-modified $BaTiO_3$ single crystals: An electron paramagnetic resonance study [J]. Applied Physics Letters, 2008, 93(20): 202901.

[171] Warren W, Vanheusden K, Dimos D. Oxygen vacancy motion i perovskite oxides [J]. Journal of the American Ceramic Society, 1996, 79(2): 536-38.

[172] Rojac T, Bencan A, Drazic G, et al. Domain-wall conduction in ferroelectric $BiFeO_3$ controlled by accumulation of charged defects [J]. Nature Materials, 2016, 16(3): 322-327.

[173] Huang X, Peng J, Zeng J, et al. The high piezoelectric properties and high temperature stability in Mn doped $Pb(Mg_{0.5}W_{0.5})O_3$-$Pb(Zr,Ti)O_3$ ceramics [J].

Ceramics International, 2019, 45(5): 6523-6527.

[174] Horiuchi N, Iwasaki Y, Nozaki K, et al. A critical phenomenon of phase transition in hydroxyapatite investigated by thermally stimulated depolarization currents [J]. Journal of the American Ceramic Society, 2017, 100(2): 501-505.

[175] Hao S, Yi J, Chao X, et al. Multiferroic properties in Mn-modified $0.7BiFeO_3$-$0.3(Ba_{0.85}Ca_{0.15})(Zr_{0.1}Ti_{0.9})O_3$ ceramics [J]. Materials Research Bulletin, 2016, 84: 25-31.

[176] Borkar H, Tomar M, Gupta V. et al. Anomalous change in leakage and displacement currents after electrical poling on lead-free ferroelectric ceramics [J]. Applied Physics Letters, 2015, 107(12): 122904.

[177] Zhao W, Zuo R, Fu J, et al. Large strains accompanying field-induced ergodic phase-polar ordered phase transformations in $Bi(Mg_{0.5}Ti_{0.5})O_3$-$PbTiO_3$-$(Bi_{0.5}Na_{0.5})TiO_3$ ternary system [J]. Journal of the European Ceramic Society, 2014, 34(10): 2299-2309.

[178] Yimnirun R, Ngamjarurojana A, Wongmaneerung R, et al. Temperature scaling of ferroelectric hysteresis in hard lead zirconate titanate bulk ceramic [J]. Applied Physics A, 2007, 89(3): 737-741.

[179] Damjanovic D. Stress and frequency dependence of the direct piezoelectric effect in ferroelectric ceramics [J]. Journal of Applied Physics, 1997, 82(4): 1788-1797.

[180] Baek S H, Folkman C M, Park J W, et al. The nature of polarization fatigue in $BiFeO_3$ [J]. Advanced Materials, 2011, 23(14): 1621-1625.

[181] Matsuo H, Kitanaka Y, Inoue R, et al. Switchable diode-effect mechanism in ferroelectric $BiFeO_3$ thin film capacitors [J]. Journal of Applied Physics, 2015, 118(11): 114101.

[182] Yoneda Y, Kitanaka Y, Noguchi Y, et al. Electronic and local structures of Mn-doped $BiFeO_3$ crystals [J]. Physical Review B, 2012, 86(18): 184112.

[183] Wang C C, Zhang M N, Xu K B, et al. Origin of high-temperature relaxor-like behavior in $CaCu_3Ti_4O_{12}$ [J]. Journal of Applied Physics, 2012, 112(3): 034109.

[184] Wang C, Zhang M, Xia W, et al. High-temperature dielectric relaxation in $Pb(Mg_{1/3}Nb_{2/3})O_3$-$PbTiO_3$ single crystals [J]. Journal of the American Ceramic Society, 2013, 96(5): 1521-1525.

[185] Wang J, Tang X G, Chan H L W, et al. Dielectric relaxation and electrical properties of $0.94Pb(Fe_{1/2}Nb_{1/2})O_3$-$0.06PbTiO_3$ single crystals [J]. Applied Physics Letters, 2005, 86(15): 152907.

[186] Ang C, Yu Z. Oxygen-vacancy-related low-frequency dielectric relaxation and electrical conduction in Bi:$SrTiO_3$ [J]. Physical Review B, 2000, 62(1): 228-236.

[187] Zhu H, Zhang Y, Wang P, et al. Resistive switching effect and conduction mechanism of $BiFeO_3$ thin films [J]. Journal of the Chinese Ceramic Society, 2017, 45(4): 467-471.

[188] Borkar H, Rao V, Tomar M, et al. Near room temperature bismuth and lithium co-substituted $BaTiO_3$ relaxor ferroelectrics family [J]. Journal of Alloys and Compounds, 2018, 737: 821-828.

[189] Liu N, Liang R, Zhao X, et al. Tailoring domain structure through manganese to modify the ferroelectricity, strain and magnetic properties of lead-free $BiFeO_3$-based multiferroic ceramics [J]. Journal of Alloys and Compounds, 2018, 740: 470-476.

[190] Chauhan S, Kumar M, Pal P. Substitution driven structural and magnetic properties and evidence of spin phonon coupling in Sr-doped $BiFeO_3$ nanoparticles. Rsc Advances, 2016, 6(72): 68028-68040.

[191] Peng J, Zeng J, Zheng L, et al. The interplay of phases, structural disorder and dielectric behavior in Al doped $BiFeO_3$-$BaTiO_3$ ceramics [J]. Journal of Alloys and Compounds, 2019, 796: 221-228.

[192] Lebeugle D, Colson D, Forget A, et al. Room-temperature coexistence of large electric polarization and magnetic order in $BiFeO_3$ single crystals [J]. Physical Review B, 2007, 76(2): 024116.

[193] Yan F, Zhou X, He X, et al. Superior energy storage properties and excellent stability achieved in environment-friendly ferroelectrics via composition design strategy [J]. Nano Energy, 2020, 75: 105012.

[194] Qi H, Zuo R, Xie A, et al. Ultrahigh energy-storage density in $NaNbO_3$-based lead-free relaxor antiferroelectric ceramics with nanoscale domains [J]. Advanced Functional Materials, 2019, 29(35): 1903877.

[195] Qi H, Xie A, Tian A, et al. Superior energy-storage capacitors with simultaneously giant energy density and efficiency using nanodomain engineered $BiFeO_3$-$BaTiO_3$-$NaNbO_3$ lead-free bulk ferroelectrics [J].

Advanced Energy Materials, 2019, 10(6): 1903338.

[196] Hoshina T. Size effect of barium titanate: fine particles and ceramics [J]. Journal of the Ceramic Society of Japan, 2013, 121(2): 156-161.

[197] Arlt G, Hennings D, With G. Dielectric properties of fine-grained barium titanate ceramics [J]. Journal of Applied Physics, 1985, 58(4): 1619-1625.

[198] Yang Z, Gao F, Du H, et al. Grain size engineered lead-free ceramics with both large energy storage density and ultrahigh mechanical properties [J]. Nano Energy, 2019, 58: 768-777.

[199] Ghosh D, Sakata A, Carter J, et al. Domain wall displacement is the origin of superior permittivity and piezoelectricity in $BaTiO_3$ at intermediate grain sizes [J]. Advanced Functional Materials, 2014, 24(7): 885-896.

[200] Zheng T, Zhao C, Wu J, et al. Large strain of lead-free bismuth ferrite ternary ceramics at elevated temperature [J]. Scripta Materialia, 2018, 155: 11-15.

[201] Bokov A A, Ye Z G. Recent progress in relaxor ferroelectrics with perovskite structure [J]. Journal of Materials Science, 2006, 41(1): 31-52.

[202] Yan K, Chen X, Wang F, et al. Large piezoelectricity and high transparency in fine-grained $BaTiO_3$ ceramics [J]. Applied Physics Letters, 2020, 116(8): 082902.

[203] Zhou C, Li Q, Xu J, et al. Ferroelectric-quasiferroelectric-ergodic relaxor transition and multifunctional electrical properties in $Bi_{0.5}Na_{0.5}TiO_3$-based ceramics [J]. Journal of the American Ceramic Society, 2018, 101(4): 1554-1565.

[204] Liu X, Guo H, Tan X. Evolution of structure and electrical properties with lanthanum content in $[(Bi_{1/2}Na_{1/2})_{0.95}Ba_{0.05}]_{1-x}La_xTiO_3$ ceramics [J]. Journal of the European Ceramic Society, 2014, 34(12): 2997-3006.

[205] Yin Q R, Zeng H R, Yu H F, et al. Near-field acoustic and piezoresponse microscopy of domain structures in ferroelectric material [J]. Journal of Materials Science, 2006, 41(1): 259-270.

[206] Fu D, Taniguchi H, Itoh M, et al. Relaxor $Pb(Mg_{(1/3)}Nb_{(2/3)})O_3$: a ferroelectric with multiple inhomogeneities [J]. Physical Review Letters, 2009, 103(20): 207601.

[207] Tunkasiri T, Rujijanagul G. Dielectric strength of fine grained barium titanate ceramics [J]. Journal of Materials Science Letters, 1996, 15:171.

## Title : : Elaboration, structure and functional properties of $BiFeO_3$-based ferroelectric ceramics

**Keywords :** $BiFeO_3$, Piezoelectric Performances, Morphotropic phase boundaries (MPB), Domain's Pinning, Defects, Energy storage

**Abstract :** Bismuth ferrite ($BiFeO_3$), abbreviated BFO, is a ferroelectric material that is of interest due to its high Curie temperature (Tc=825 °C) and its large spontaneous polarization (~100 µC/cm$^2$). The thesis work is related to ceramics based on BFO with different compositions and focusing on the optimization of ferroelectric performances with high Curie temperatures.
(1) The addition to BFO of perovskite structures $BaTiO_3$ (BT) and $PbTiO_3$ (PT) was carried out in order to form morphotropic phase boundaries (MPB) leading to materials with high piezoelectric coefficients while being stable at high temperatures. The study of these BFO-PT-BT ceramics aims to understand the interaction between the effects at the interfaces, the microstructure and lattice distortions. In the same context, defects such as oxygen vacancies and mixed valences $Fe^{3+}/Fe^{2+}$ coexist and contribute to modulate the electrical performance of the ferroelectric and piezoelectric response as well as the electrical conductivity in this group of functional ceramics. (2) Doping by appropriate structures, in particular based on $Ba(Sn_{0.2}Ti_{0.8})O_3$, has also been exploited to improve the ferroelectric and piezoelectric properties of BFO-PT-BT ceramics. The effect of defects on the reorientations of ferroelectric domains (pinning phenomena) was studied as well as their role in the mechanisms responsible behind the leakage currents. (3) The large spontaneous polarization and the adjustable pseudo-cubic phase structure of BFO, BFO-BT lead-free ferroelectric ceramics were investigated with an emphasis on the high dielectric energy densities involved in functional structures. These studies open new ways for the application of these ceramics in the field of energy storage which may offer an alternative to chemical processes.

## Titre : Elaboration, structure et propriétés fonctionnelles des céramiques ferroélectriques à base de ferrite de bismuth $BiFeO_3$

**Mots clés :** $BiFeO_3$, Performances piézoélectriques, Limites de phases morphotropes (MPB), Pinning de domaines, Défauts, Stockage de l'énergie

**Abstract :** La ferrite de bismuth ($BiFeO_3$, abrégée BFO) est un matériau ferroélectrique qui suscite l'intérêt en raison de sa température de Curie élevée (Tc=825 °C) et de sa grande polarisation spontanée (~100 µC/cm$^2$). Le travail de thèse s'inscrit dans ce cadre et porte sur des céramiques ferroélectriques à base de BFO avec différentes compositions.
(1) L'ajout à BFO de structures pérovskites $BaTiO_3$ (BT) et $PbTiO_3$ (PT) a été réalisé en vue de former des limites de phase morphotropes (MPB) conduisant à des matériaux à forts coefficients piézoélectriques tout en étant stables à hautes températures. L'étude de ces céramiques BFO-PT-BT vise à comprendre l'interaction entre l'organisation et les effets aux interfaces avec notamment la limite de phases, la microstructure et les distorsions du réseau. Dans ce même cadre, les défauts telles que les lacunes d'oxygène et les valences mixtes $Fe^{3+}/Fe^{2+}$ coexistent et contribuent à modifier les performances électriques qui portent sur la réponse ferroélectrique, piézoélectrique ainsi que la conductivité électrique dans ces céramiques fonctionnelles. (2) Le dopage par des structures appropriées notamment à base de $Ba(Sn_{0.2}Ti_{0.8})O_3$ a été aussi exploité pour améliorer les propriétés ferroélectriques et piézoélectriques des céramique BFO-PT-BT. L'effet des défauts sur les réorientations des domaines ferroélectriques (phénomène de *pinning*) a été étudié ainsi que leur rôle dans les mécanismes responsables des courants de fuite. (3) Compte tenu de la grande polarisation spontanée et de la structure de phase pseudo-cubique ajustable de BFO, les céramiques ferroélectriques sans plomb de type BFO-BT ont été étudiées comme structures fonctionnelles offrant de grandes densités d'énergie diélectriques. Ces études ouvrent des perspectives d'application de ces céramiques dans le domaine de stockage de l'énergie offrant ainsi une alternative aux procédés chimiques.